NASA SP-384

SIGNIFICANT ACCOMPLISHMENTS IN SCIENCE AND TECHNOLOGY

Goddard Space Flight Center, 1974

A symposium held at

GODDARD SPACE FLIGHT CENTER

December 5, 1974

NATIONAL AERONAUTICS AND SPACE ADMINISTRATION

NASA SP-384

SIGNIFICANT ACCOMPLISHMENTS IN SCIENCE AND TECHNOLOGY

GODDARD SPACE FLIGHT CENTER, 1974

The proceedings of a symposium held at the NASA
Goddard Space Flight Center, December 5, 1974

Prepared by Goddard Space Flight Center

Scientific and Technical Information Office 1975
NATIONAL AERONAUTICS AND SPACE ADMINISTRATION
Washington, D.C.

FOREWORD

This is an almost verbatim transcript of a symposium held at Goddard Space Flight Center, Greenbelt, Maryland, on December 5, 1974. No attempt has been made to introduce editorial or stylistic uniformity in the talks; on the contrary, an effort has been made to retain the informality of the proceedings.

The sole major change results from NASA policy, which now requires in all formal publications the use of international metric units according to the Systeme International d'Unites (SI). However, in certain cases utility requires the retention of other systems of units in addition to the SI units. The conventional units stated in parentheses following the computed SI equivalents are the basis of the measurements and calculations reported here.

Page intentionally left blank

Page intentionally left blank

CONTENTS

CONTENTS (continued)

CONTENTS (continued)

CONTENTS (continued)

CONTENTS (continued)

MEASUREMENT OF SOIL MOISTURE UTILIZING THE DIURNAL RANGE OF SURFACE TEMPERATURES

Thomas J. Schmugge

The purpose of the first Applications Explorer (AE) Mission is to map heat capacities by observing the diurnal range of surface temperatures. The initial object was to use heat capacity differences to map rock types. But it is clear that soil moisture differences also can be mapped in this way.

The basic phenomena used are illustrated in figure 1, which presents surface temperatures for a field versus time, before and after an irrigation. These data were obtained by Dr. Ray Jackson and his colleagues at the U.S. Water Conservation Laboratory in Phoenix. We have been collaborating with them on the analysis of these data.

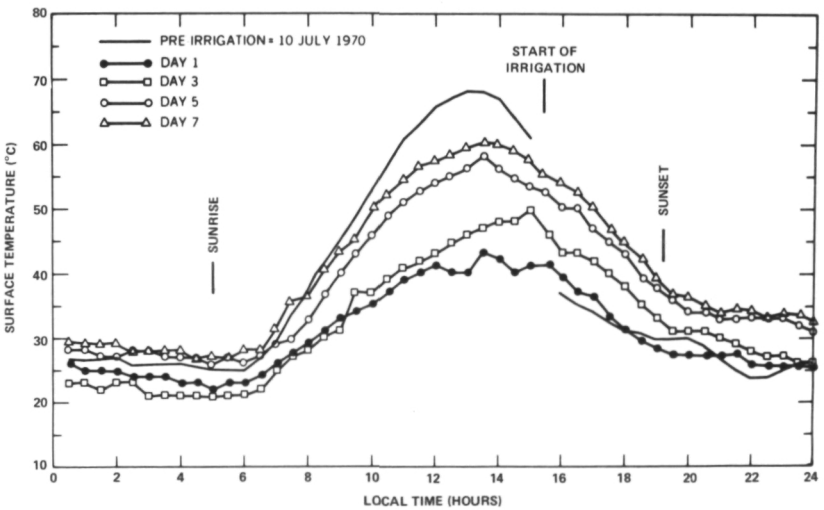

Figure 1. Data from U.S. Water Conservation Laboratory, Phoenix, Arizona.

The solid line in figure 1 is the plot of surface temperature before irrigation, and the filled circles reflect the data on the day following irrigation. There

is a dramatic difference in the maximum temperature achieved on these two days.

On succeeding days, the third, the fifth, and the seventh, the maximum temperature increases as the field dries out.

The summary of results from many such experiments is shown in figure 2 where the amplitude of the diurnal range is plotted as a function of the soil moisture as measured at the surface and at 0- to 1-cm, 0- to 2-cm, and 0- to 4-cm layers.

There is a reasonably linear correlation with the soil moisture in the 0- to 2-cm and 0- to 4-cm layers of the soil, and this response is related to the actual heat capacity of the soil. Initially, when the surface is moist, the temperatures are more or less controlled by evaporation. Once the surface layer dries below a certain level, the temperature is determined by the heat capacity of the soil.

These results indicate that for this particular soil, the diurnal range of surface temperature is a fairly good measure of the soil moisture.

When these measurements are repeated for different soils, there are differences which depend on the soil type. However, there are certain characteristics that are independent of the soil type, and these relate to the evaporation of the water from the soil.

Figure 3 presents an example of the drying characteristics for the particular soil at the Phoenix Laboratory. These are results of three different plots. The top, or wet plot, was irrigated with 18 cm of water; the middle plot was irrigated with 1 cm of water; and the third plot was not irrigated at all.

The photographs in the visual appearance plot were taken every half hour at the same time the measurements of albedo and evaporation were taken, and there is a striking change in the albedo of the middle plot as the soil dries.

Soil physicists have characterized the drying of a soil in three stages. They are:

- The wet stage, where the evaporation is solely determined by the meteorological conditions;
- An intermediate or drying stage where it starts out being in the wet stage early in the day, but because there is not a sufficient amount of water in the soil to meet the evaporative demand, the evaporation rate falls off; and

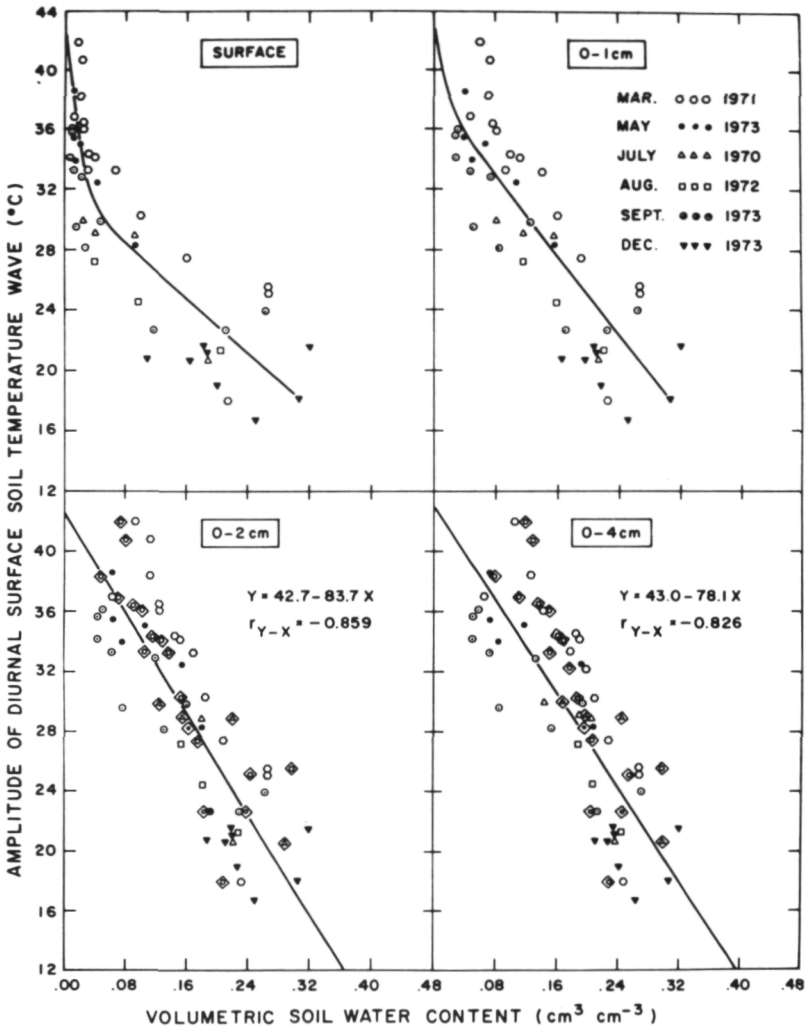

Figure 2. Summary of results of heat capacity experiments.

- The dry stage, where evaporation is solely determined by the molecular transfer properties of water within the soil.

There is a striking change in both the albedo and the evaporation rate as the soil dries during the transition from the wet stage to drying stage.

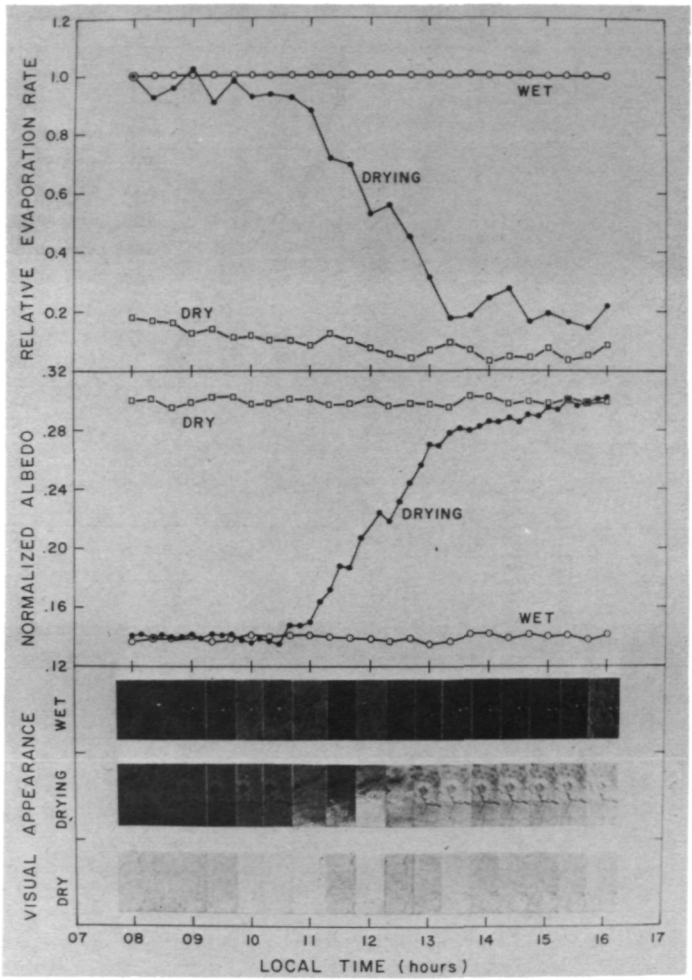

Figure 3. Comparative plots of drying characteristics of Phoenix Laboratory soil.

Similar measurements were repeated for different soil types, and the results indicate that the transitions from the wet stage to the drying stage occur at about the same values of ΔT for the different soils.

Figure 4 summarizes these results for the different soil types. The soils ranged from sandy or light soils to heavy clay soils, and it is clear that for a given diurnal temperature difference, there can be a wide range of soil moisture content.

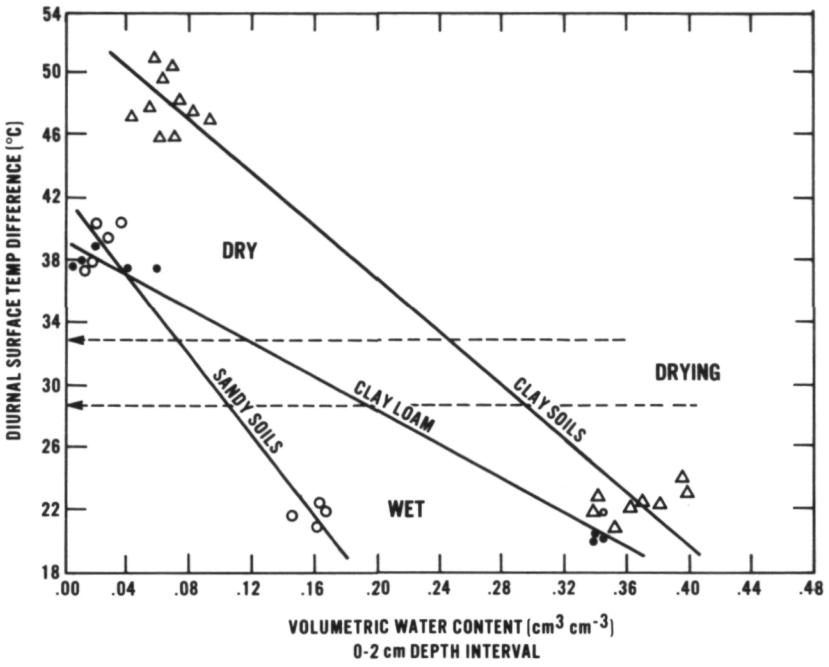

Figure 4. Summary of results of experiments using various soil types.

However, it has been observed that, as these soils dry out, the ΔT is approximately the same for these soil types during transition from the wet stage to the intermediate stage.

Similarly, at the transition from the intermediate stage to the final stage, or the dry stage, again the ΔT is approximately the same for these soil types.

The interesting point is that when the soils are in the wet stage, they are at field capacity or above; there is sufficient moisture for plants to grow. In the intermediate stage, the soil is between field capacity and the wilt point, that is, the moisture level at which plants would begin to wilt. In the dry stage the moisture level is below the wilt point. The moisture level referred to here is for the top 4 cm of the soil.

Thus, this technique can be used, while not to give an absolute value of soil moisture, at least to determine the qualitative state of the moisture in the soil independent of soil type.

In conclusion, I would like to emphasize that these experiments were all field measurements, made in a field, and were not remotely sensed. We are

now in the process of undertaking experiments to verify these results from aircraft platforms.

DISCUSSION

JAFFE: In the last figure (figure 4), only end-point data are plotted. Were intermediate data acquired?

SCHMUGGE: We only plotted the end-point data, and we have not plotted all the data in between.

VOICE: (Inaudible question.)

SCHMUGGE: The data shown in figure 2 were for one of the soils presented in figure 4, and for the same soil layer. We did get the linear response—the linear response is demonstrated in figure 2 at approximately a 2-cm-depth interval. All the data points were not shown in figure 4 in order to simplify the presentation. But the results were linear.

JAFFE: Are the curves linear?

SCHMUGGE: Yes.

MULTIYEAR SATELLITE SNOWCOVER-RIVER RUNOFF RELATIONSHIPS

Albert Rango and Vincent V. Salomonson

The launch of Landsat-1 (formerly ERTS-1) and NOAA-2 in 1972 provided sensors that adequately observed changes in the aerial extent of snow cover over local and regional watersheds of interest to water resources management agencies. As an example, figure 1 shows four views taken by Landsat-1 over the Wind River Mountains in Wyoming. These illustrate snowcover accumulation and snowmelt during the 1972 to 1973 snow season. Even though it has been shown that snow extent can be accurately measured from such images, there has been some question about the usefulness of these data in terms of predicting snowpack yield or seasonal runoff because only the area covered by snow, not snow depth or water equivalent, is observed. Only two years of snowcover versus runoff information exists for Landsat-1 and NOAA-2, and this does not provide a sufficient number of observations to indicate the validity of any empirical statistical relationship that might appear to exist between the snow-covered area and runoff. As a result, longer duration data than currently exist for Landsat-1 had to be obtained.

Some of our previous work showed promise for relating meteorological satellite snowcover data (based on two years of data) to seasonal runoff data for very large watersheds such as the Indus River Watershed in the western Himalayas. Because several years of meteorological satellite data now exist, this work has been extended to cover six years of snowcover versus runoff data and to test whether an empirical relationship of statistical significance is evident.

Figure 2 shows sample observations from the operational ESSA-9 meteorological satellite over the Indus River Watershed (outlined in black) above Attock, Pakistan, where an International Hydrological Decade stream gaging station exists. The watershed outlined here covers about a half million square kilometers (300,000 square miles). It can be seen that these early April observations are distinctly different in terms of the snow-covered area in the watershed, and a similar difference is observed in the resulting runoff.

In 1969, the snow-covered area was approximately 60 percent, and the resulting runoff, April through June, was about 36.4 billion m^3 (29.5 million

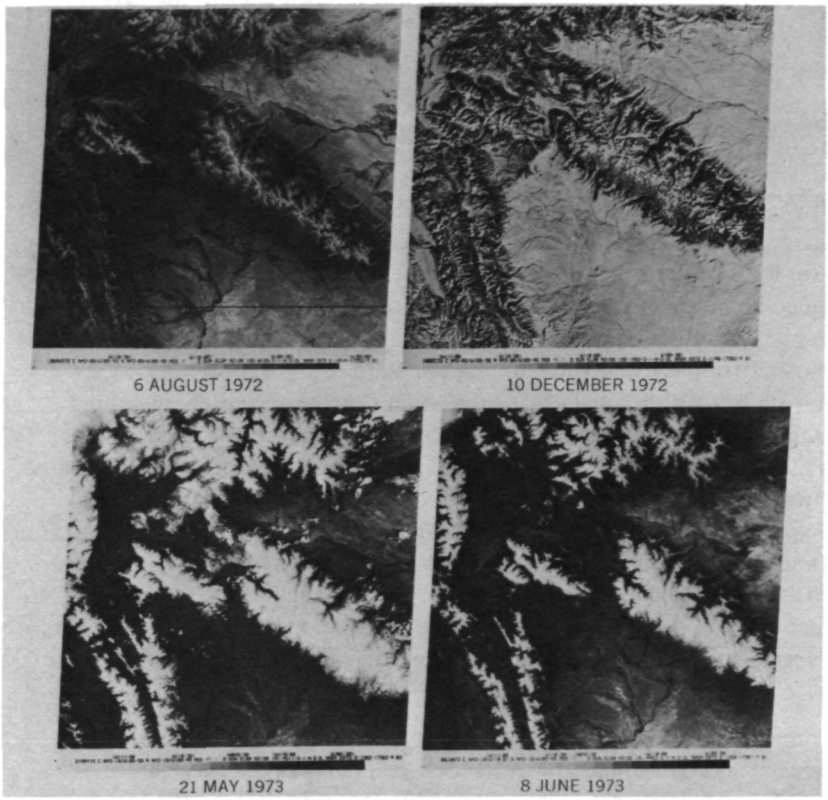

Figure 1. Snowcover changes in northwestern Wyoming.

acre-feet). Whereas, in 1971, the snow-covered area in the watershed is considerably less, about 44 percent, and the April through June runoff is 30.7 billion m^3 (24.9 million acre-feet). Acre-feet units are retained because they are traditional irrigation units. One acre-foot of water is equal to about 1.23×10^3 m^3 of water, which is why we are still using acre-feet, that is, until we can accustom the traditionalists to the new units. Using observations such as these, the average snow cover, during the period April 1 to 15, in percent of watershed area, was plotted against seasonal runoff in acre-feet for the years 1967 through 1972, and is shown in figure 3.

Typical runoff volumes are in the 24.7 to 37 billion m^3 (20 to 30 million acre-feet) range. As can be seen, a good statistical relationship between April snow cover and the resulting April through June runoff does exist. The coefficient of determination, R^2, is 0.92, and the standard error of estimate is 5 percent of the mean seasonal yield. Even though snow depth or water

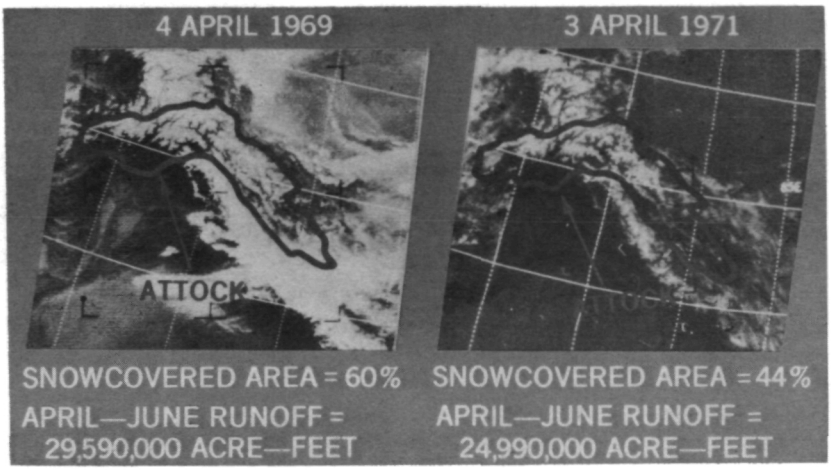

Figure 2. ESSA-9 observations of the annual variation in snow-covered area at the beginning of snowmelt in the Indus River Basin.

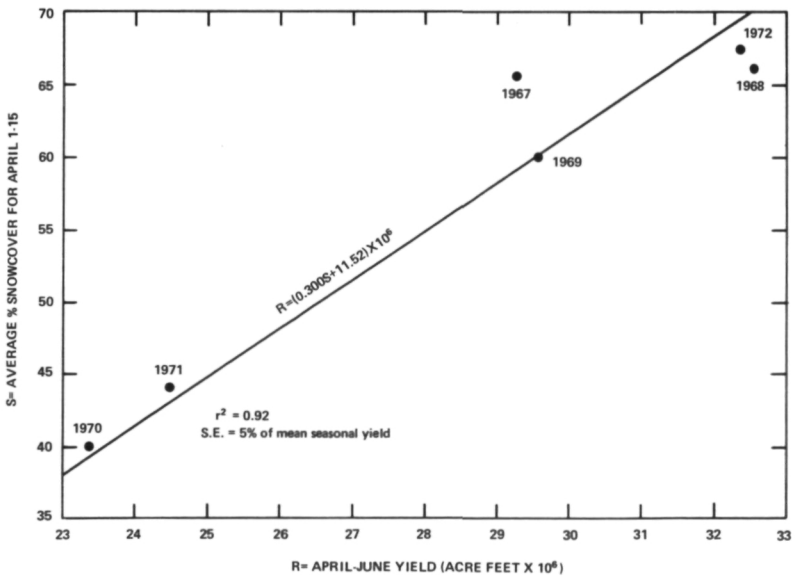

Figure 3. Satellite-derived snowcover estimates versus measured runoff for the Indus River.

equivalent are not directly measured here, it appears that the areal snow extent is an adequate index parameter for predicting runoff.

This result offers definitive and quantitative evidence that satellite snow-cover observations can be used in lieu of other snowpack parameters to predict seasonal runoff, if enough years of information exist, or as valuable ancillary information that can be combined with conventional snowpack observations for any given year. In view of the significance of water stored in the form of snow in the Western United States for hydroelectric power generation, irrigated agriculture, and reservoir regulation, the importance and value of more accurate runoff information provided by satellite observations is very promising.

DISCUSSION

VOICE: Does this mean that the average density of the snow is pretty uniform over these areas?

RANGO: That is not necessarily so. What is showing is that the area covered by snow and the rate with which it changes is distinctly related to how much water is stored in the watershed. The greater the amount of water stored in the watershed, the slower the change in the area covered.

The densities do not have to be uniform, but if you see a rapid change in the area covered by snow, you know you had a relatively thin snowpack with not much water stored. The snowcover change also happens to be very well correlated to the amount of runoff that occurs at the streamgage.

VOICE: It is also interesting that the plot is a straight line in figure 3, as Mr. Chapman mentioned before, and it looks like the depth of the snow does not matter; just the area.

RANGO: I would not say that; I think it is fortunate for us that depth is so well related to the area.

VOICE: How does the relationship that we have vary from one watershed to another around the world?

RANGO: This is the major watershed that we have tested, but we have seen, using the first images that I showed you in Wyoming, that with over two years of data, the same kinds of relationships exist. There are seven watersheds in that region with different elevations, and we have seen that the runoff peaks were well related to the change in the snow-covered area.

We think we are seeing the same kinds of things in Wyoming and other areas in the Western United States that you see here in the longer duration data. We are hoping to build up four or five years of data to test that out.

VOICE: You have no information on other countries at this time?

RANGO: No. This is the one foreign watershed that we used. It is very difficult to get runoff data from undisturbed watersheds in some of these remote areas.

VOICE: How many years of Landsat-1 data do we need to produce similar relationships?

RANGO: We feel that somewhere between four and six years of data are necessary, and we have projects underway that will use ERTS and NOAA data to build up the data base that we think is necessary in the United States.

VOICE: Can the NOAA satellites provide data that are pertinent?

RANGO: Yes, we are able to take the NOAA data, which is available on essentially a daily basis with a resolution of about 0.9 kilometers (0.6 miles), and we are able to monitor the changes in a snow-covered area. We can calibrate the NOAA data with the high resolution ERTS data and obtain very satisfying continuity of data.

VOICE: Do we need ERTS to calibrate NOAA data?

RANGO: The results so far by the NOAA investigators indicate that ERTS data are very valuable to them in calibrating their information.

VOICE: Will the runoff correlation be better in mountainous areas than in the plain areas?

RANGO: The value of measuring the snow-covered areas in the mountains is that they have distinct topographic indicators that allow us good reference in regard to the area covered. In the plains, we may have some discrepancies, but we feel that if the snow lasts long enough, very often in the plains it comes quickly and leaves quickly, and relationships are not as good. But if it lasted long enough, we should have the same type of results, but perhaps not as accurate.

RANGO: The significance of the April date is that, many times, the forecast in the United States, at least, has to be made on April 1 for the rest of the year. And therefore, we have tried to take a date early in April, or an average date during April, that can be used by people like the Soil Conservation Service to come up with a meaningful forecast at that time. It is possible to update these forecasts later in April and also into May. But we need early values to give us an initial forecast.

GLOBAL MEASUREMENTS OF THE SiO_2 EMISSIVITY BAND STRENGTH FROM NIMBUS-4 IRIS

Cuddapah Prabhakara and Giuseppe Dalú

The surface emissivity of soil in the infrared can be useful in inferring soil properties. In the present study we have found that the surface emissivity sensed from a satellite can be related to the aridity of a given desert region.

The surface emissivity depends strongly on the grain size of the surface material and also on the vegetation cover. The lack of rain and vegetation promotes coarse grain size due to erosion, while the rain and vegetation favor the formation of fine soil. Thus, the measurement of surface emissivity gives a composite index of the surface character.

The infrared interferometer spectrometer (IRIS) flown on the Nimbus-4 satellite revealed, around 9 μm, the emissivity band that is characteristic of the earth's deserts. This characteristic band found in desert regions is due to the wavelength-dependent properties of silicate-type materials found in these regions.

In figure 1, a spectrum taken over a cloud-free ocean and a spectrum taken over the Sahara desert are shown to illustrate the emissivity band effect. The abscissa in the figure is the wave number, which is the reciprocal of wavelength. Channel 1 on this scale corresponds to 11 μm and channel 2, to 9 μm. The mean brightness temperature in the 11- and the 9-μm regions over the ocean is the same. Over the desert, due to the emissivity effects, the spectrum is considerably colder in the 9-μm region.

It is found that the desert spectrum can be explained in terms of silicon dioxide emissivity and water vapor absorption. A spectrum fitted in this fashion is shown in figure 1 by the dotted line.

With this approach, the IRIS data are analyzed to give the silicon dioxide emissivity band strength over the globe for the period of April 1970 to January 1971. As the field of view of IRIS is fairly large, about 100 km, clouds are often present in the view of the instrument. After eliminating the cloud-contaminated data, it was possible to construct one global map of the surface emissivity for the entire period of IRIS data (figure 2). In this map, all the major desert regions are vividly seen. The minimum emissivity is present over the Sahara and the Middle East. A band of

intermediate strength is seen over the Kalahari, Australian, and Mongolian deserts. The weakest feature is seen over the Southwest United States and Atacama.

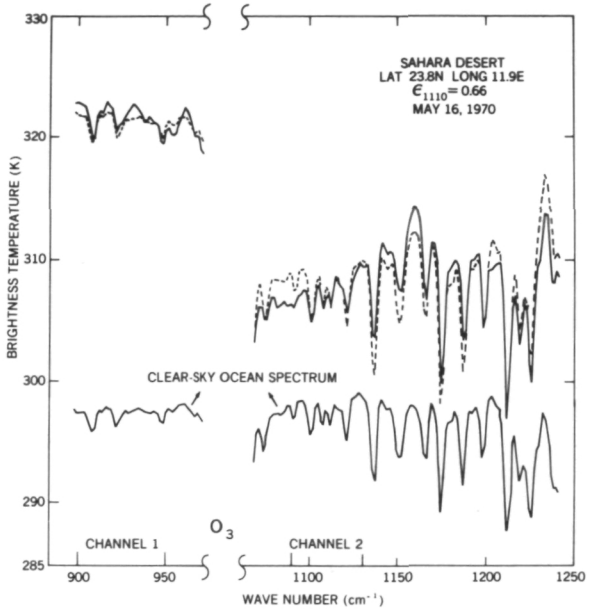

Figure 1. Comparison between a clear-sky ocean spectrum and a spectrum taken over the Sahara desert. The dotted line is a spectrum obtained by combining the water vapor absorption spectrum and the silicon dioxide emissivity spectrum.

In order to appreciate the significance of this map, a climatic map of the globe is shown (figure 3). Here the extremely arid regions are shaded in black, followed by arid and semiarid areas in lighter shades. From an examination of this map, one can see a close correspondence with the surface emissivity map shown earlier. It appears that the extremely arid regions have a 9-μm emissivity between 0.76 and 0.84, the arid ones have an emissivity range of 0.84 to 0.92, and the semiarid deserts have a range from 0.92 to 0.96.

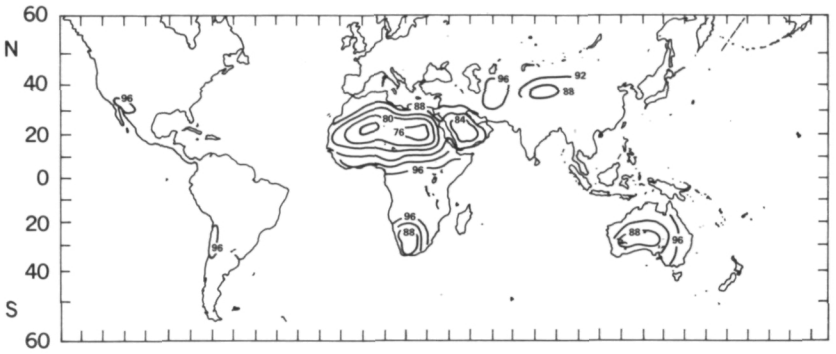

Figure 2. Global distribution of the emissivity in the 9-μm region as calculated from IRIS measurements.

From this study it may be concluded that data from a simple scanning infrared radiometer with a channel in both the 11- and the 9-μm window regions can yield useful information about climatic state and possibly detect the development of drought conditions.

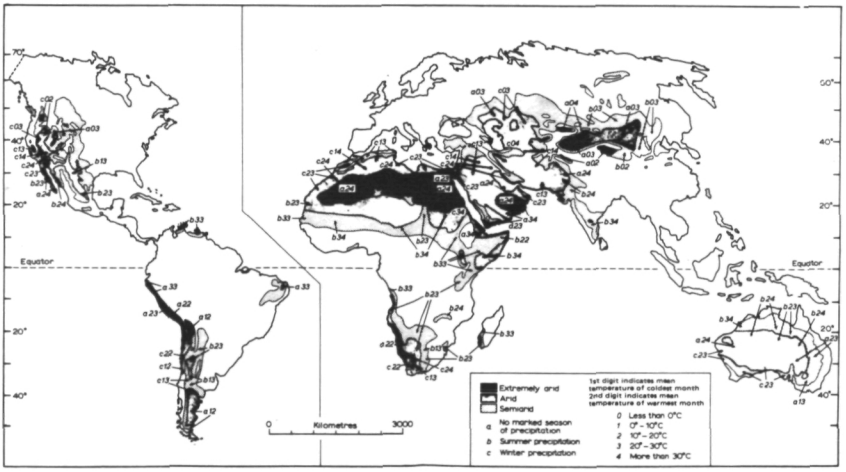

1.1 World distribution of arid lands (after Meigs, 1953).

Figure 3. Distribution of the semiarid, arid, and extremely arid regions.

STUDY OF THE SAHARA DROUGHT

Peter H. Stone*

Jule Charney recently suggested a biogeophysical mechanism which tends to enhance changes in rainfall and plant cover. This mechanism operates because of the dependence of surface albedo on plant cover. Ground covered by plants has an albedo in the range from 10 to 25 percent, while ground with no vegetation, that is, dry, sandy soil, frequently has an albedo as high as 35 or 45 percent. Thus a decrease in plant cover may be accompanied by an increase in surface albedo. This would lead to a decrease in the net incoming radiation, and, as a consequence, the air would sink to maintain thermal equilibrium by adiabatic compression causing cumulus convection and its associated rainfall to be suppressed. The lower rainfall in turn would have an adverse effect on plants and tend to enhance the original decrease in plant cover. The positive feedback would be particularly important in regions like the Sahara where (1) large scale subsidence already occurs; (2) most of the rainfall is from cumulus clouds; and (3) transports of heat by the winds are particularly weak and inefficient at counteracting temperature changes due to albedo changes. This mechanism offers a possible explanation for droughts in the Sahel, the southern region of the Sahara, where the process could be initiated by overgrazing.

To assess the plausibility of this mechanism, we need to calculate its effect together with the effects of all other mechanisms which operate simultaneously. We attempt to do this by using the Goddard Institute for Space Studies (GISS) General Circulation Model (GCM) which includes most atmospheric processes, for example, winds, convection, clouds, rain, radiative absorption, and emission. We performed two integrations, both using the observed state of the atmosphere on June 18, 1973, as an initial condition. Both integrations were carried forward for seven weeks of simulated time. The only differences between the two integrations was the prescribed surface albedo for the Sahara.

Both integrations had boundary conditions, such as the sea surface temperature and soil moisture, prescribed to correspond to climatological conditions

*Paper presented by Dr. James E. Hansen.

for July, which is in the rainy season in the Sahara. In one integration the surface albedo in the Sahara was 14 percent, and, in the other, it was 35 percent. These albedo simulate, respectively, a Sahara covered with plants and a Sahara devoid of plant cover.

Figure 1 shows the computed weekly precipitation averaged over the 46 grid points in the Sahara. The rainfall in the high albedo experiment was substantially smaller, as you can see. The consistency in the difference in rainfall in each of the seven-week periods shows that the difference is real and not a result of statistical fluctuations in the GCM's behavior.

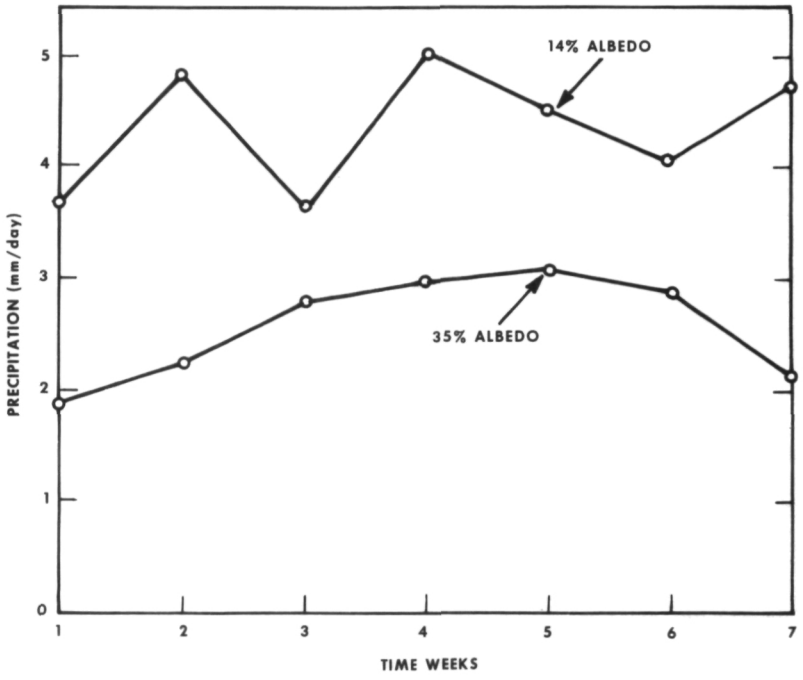

Figure 1. Precipitation with low and high albedos assumed for the Sahara.

The mean rainfall over the Sahara during the calendar month of July was 4.4 mm per day in the low albedo experiment and 2.5 mm per day in the high albedo experiment, a decrease of 43 percent. There was also a decrease in cumulus cloud cover over the Sahara when the surface albedo was increased. The mean cumulus cloud cover during July was 26 percent in the low albedo integration and 19 percent in the high albedo integration.

Figure 2 shows the latitudinal distribution of mean rainfall during July in the two experiments. The figure illustrates that most of the rainfall over the Sahara actually occurs in the Sahel, near 18°N latitude. The distribution of rainfall in the Sahara, in the 35-percent albedo experiment, is quite close to the observed distribution in summer.

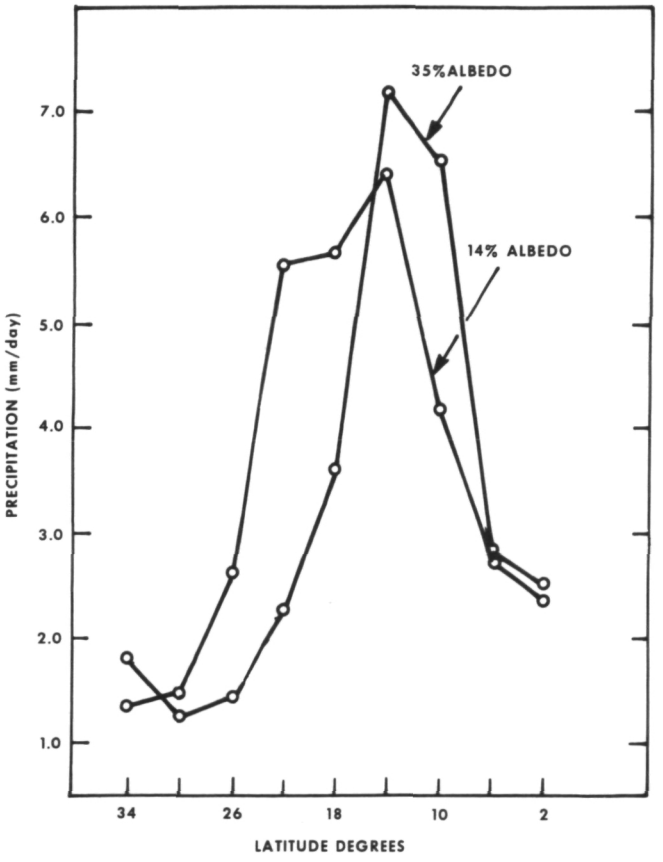

Figure 2. Latitudinal distribution of mean rainfall over the Sahara.

Figure 2 also shows that the decrease in rainfall in the Sahara in the high albedo experiment is compensated to some extent by an increase south of

the Sahara. The shift in the rainfall distribution reflects a shift to the south of the intertropical convergence zone over Africa. The latitude of mean low level convergence over Africa during July was 22° in the low albedo experiment and 16° in the high albedo experiment.

Finally, to determine how local the albedo change can be and still produce large changes in rainfall, we performed a third numerical experiment. In this experiment, the albedo was increased only in the Sahel. This integration was started from the same initial condition, but only covered two weeks of simulated time. Therefore, the results do not have the statistical significance of the first two experiments. However, they do show a similar effect in the rainfall. For example, during days 3 to 10 of the integration, the mean rainfall at 18°N latitude decreased by 75 percent. This result indicates that very local changes in the albedo may be sufficient to produce droughts.

We conclude that surface albedo can have a substantial effect on the climate in the Sahara and that the biogeophysical feedback mechanism is a plausible one for causing such changes. We can envisage overgrazing in the Sahel leading to an increase in the surface albedo. This causes the intertropical convergence zone to move south, and the rainfall over the Sahel to decrease, perhaps by as much as 40 percent.

Because the GCM we used does not include a model of the biosphere for calculating changes in albedo resulting from changes in rainfall, this 40-percent figure, is in effect, an upper bound. The need for a model of the biosphere emphasizes the complexity of climate problems. And the results also show the importance of monitoring surface albedos from satellites.

DISCUSSION

RASOOL: When you talk about the latitude, do you mean around the whole world or just in the Sahara?

HANSEN: The result for the rainfall was for just the Sahara.

RASOOL: But if you bound the problem to the Sahara, you cannot tell whether the result is significant.

HANSEN: We can tell. It is not a bounded problem. The GCM is for the entire globe, and the result for the entire latitude range was a 6-percent decrease in rainfall. But if you subtract the Sahara, then the rainfall was essentially normal for the rest of the globe.

LAU: Do you think that the atmospheric aerosol content is important through the radiation, and does the GCM take this into account?

HANSEN: I will address that in a later paper. I think it is important. But in these experiments aerosols were not included.

SCHWEIKER: Since you see a compensatory increase in the rainfall south of the Sahel, I wonder whether this would indicate that a resulting increase in the biomass at that latitude would offset the decrease in the Sahel. I wonder if it is a self-limiting problem.

HANSEN: I doubt that it would be a fully compensating increase. We cannot take all of the rain in the world, put it in one place, and end up with as much vegetation as you would if it were spread out.

SCHWEIKER: There must be some increase in the biomass as a result of the increased rainfall south of the southern region of the Sahel?

HANSEN: In terms of percentages, the increase for the south is smaller than the decrease in the Sahel. Qualitatively, there may be such an effect as you suggest, but I doubt that it is a compensating increase.

VOICE: How large must the area be in order to produce an effect such as this?

HANSEN: The local experiments consisted of a strip of 4° wide in latitude. That was the smallest area investigated, and there was a very clear effect in that case.

STONE: What does that work out to be, millions of acres?

HANSEN: Something like a few hundred kilometers wide.

VOICE: Is it reversible? Has anybody thought about how to reverse the process?

HANSEN: You would like to decrease the albedo? Perhaps if you could promote plant growth artificially in some part of the region, through fertilization or irrigation, it may tend to reverse this feedback effect.

STRIP MINE MONITORING

Arthur T. Anderson

The capability of rapidly determining the extent and condition of affected acreage in surface extractive contour coal mining regions and the assessment of such areas is of primary importance. For example, strip mines, gravel pits, and large, open quarries have been detected, analyzed, and regionally inventoried using the ERTS computer compatible tapes (CCTs) through various computer processing techniques. However, the lack of statistically quantitative results is evident throughout numerous studies. These quantitative aspects of the effects of strip mining will be discussed.

Thus, the objectives of this study are to: (1) demonstrate the capability and application of ERTS CCTs, aircraft photography, and field verification through multilevel sampling for quantitative values; (2) perform an inventory and introduce procedures for monitoring the various stages and yearly change detection of the affected acreage of extractive mining areas; (3) establish classification keys for different levels of disturbed and reclaimed areas; and (4) establish an exchange of resulting data with the Maryland State Bureau of Mines and the Geological Survey so that their field-derived data can be used for comparative results.

This study will concentrate on one segment: contour strip mines (figure 1) and their affected acreage in Garrett County in western Maryland.

Strip mines in this area are 76 to 400 meters (250 to 1300 feet) wide (including the 9- to 30-meter (30- to 100-foot) spoil banks), have a high wall of 18 to 46 meters (60 to 150 feet), and cover approximately 4050 to 113,300 square meters (10 to 280 acres). To best analyze these affected areas rapidly, which are relatively small areas, and to make maximum use of the ERTS system, the G.E. Image 100 system was chosen to analyze the area as it looked on September 1, 1973, and to later compare it with the September 1972 and September 1974 scenes.

The Image 100 system makes best use of the spatial and spectral tape data to manipulate the digital values in an interactive mode. It simultaneously analyzes and displays radiometric histograms or spectral signatures while training on a specific feature within the scene.

Figure 1. A contour strip mine in Garrett County, Maryland.

Figure 2 is from a color, IR rendition of the output. This enlarged training (sample) area, from the Image 100 system at 4:1 (16 TV elements/ERTS picture element (pixel)), contains 15 mines in 36 square kilometers (15 square miles) in the scene, and was classified into seven themes. They were derived, correlated (as seen with the 1:18,000 aircraft data), field-verified, and refined, based on surface texture, color, and subsoil reflectance values. These themes are: three for strip mines which correlated to specific coals seams and spoils, bare soil, revegetated areas, open fields, and forest.

A composite of the themes was applied to the training area, then later to the entire area under study. The signatures for the areas agreed with field verification reflectance values and ground-truth assessment.

To examine the quantitative aspect, seven mine areas were chosen and delineated, using only the three strip mine classes, revegetated and bare soil themes. Values, based on rapid and continuous strip mine processing, were assigned to the changes noted by each theme, cumulated, and compared directly with the state's recorded stripped and backfilled acreage. For example, figure 3, shows the line of best fit and comparison (Image 100) of ERTS versus aircraft and Maryland Bureau of Mines data for Mill Run. The state data showed that there were 135 affected acres, the Image 100 data showed over 60,690 square meters (150 acres) plus at least 16,200 square

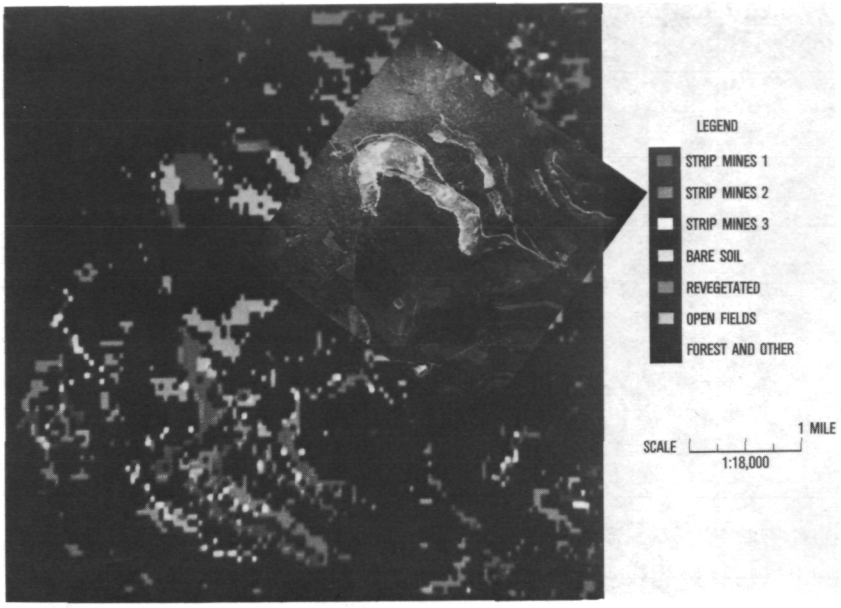

Figure 2. IR rendition from the Image 100 system. The enlarged sample area contains 15 mines.

meters (40 acres) on the boundary, and the aircraft data showed that there were 30-percent more affected acres than the state data showed. However, vast improvements are now expected, as work continues with the Image 100 system, in classifying the boundary pixel areas, or mixed pixels, to derive better quantitative data. This shows that, although these are the post-1967 through 1973 values (when Maryland began recording such acreage), the September 1973 data correlated on the average with state and Image 100 figures and not fully with the 1:18,000 aircraft data. The aircraft provides the most reliable coverage, but has the smallest coverage base.

These comparisons show that, upon backfilling and grading, additional acreage is affected after stripping. For example, this study showed that there were approximately 25 to 30 percent more acres affected by the strip mining process than accounted for in the data available to the state.

In summary, computer multispectral analysis has demonstrated the application of an added dimension, which should prove complementary to the state's records, by providing an additional source of information. By monitoring change detection on an annual to semiannual basis through this rapid procedure, comparison of the stripped, backfilled, and planted (or reclaimed) acreage will provide the state with information for control and planning for future activities on a quantitative basis.

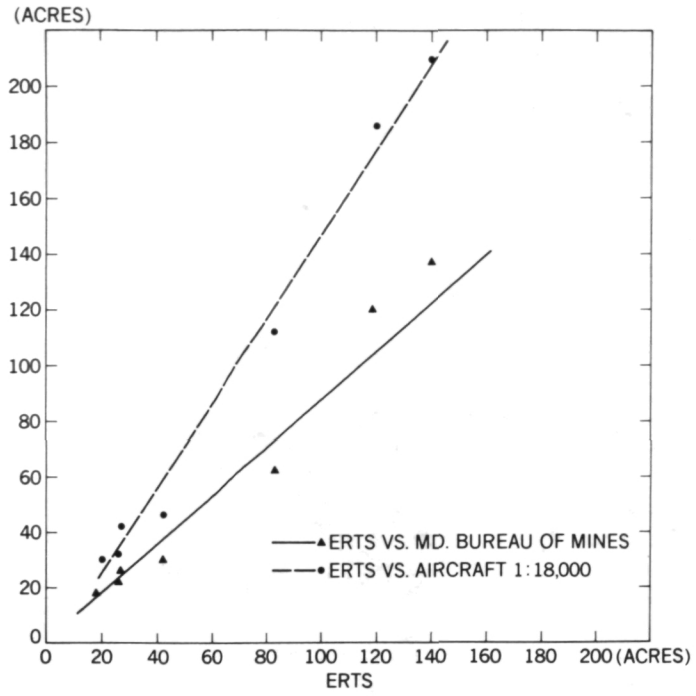

Figure 3. The line of best fit and comparison (Image 100) of ERTS versus aircraft and Maryland Bureau of Mines data for bare soil themes.

EVALUATION OF THE NIMBUS/ATS-6 AND GEOS-C/ATS-6 SATELLITE-TO-SATELLITE TRACKING EXPERIMENTS

Peter D. Argentiero

During the early part of the GEOS-C mission, it is planned to track GEOS-C from the geosynchronous ATS satellite from a position of 94° west longitude. Several months later, we will again track GEOS-C from a position of 34° east longitude. The purpose of the GEOS-C/ATS-6 satellite-to-satellite tracking (SST) experiment is to extract from the resulting data improved estimates of the low frequency terms of the geopotential field. This is an important experiment because several of the critical experiments of NASA's Earth and Ocean Physics Applications Program have as their dominant error source the uncertainty in the low frequency terms of the geopotential field. Among these are experiments associated with satellite altimetry and those related to the satellite determination of tectonic plate motions.

Our problem to date in estimating these low frequency geopotential terms is that we do not have a good global distribution of satellite perturbation data or surface gravity data. Consequently, our estimates have been badly aliased and, in general, lack a good statistical independence. This is essentially an observability problem, and it is an important point; no amount of added data selected from the same well-covered areas improves the situation. What is needed for a significant breakthrough is a more global distribution of data, and this particular experiment should provide it.

Figure 1 shows the coverage of the earth afforded by ATS-6 from its two prime geosynchronous positions—one at 94° west longitude, with the data being relayed to the Rosman tracking station, and at 34° east longitude, where the data is relayed to the Madrid tracking station. This coverage is about six-sevenths of the earth.

This fact, combined with the fact that GEOS-C has a high inclination, about 115°, implies that we should obtain an almost global distribution of data. This assumption is also valid for the Nimbus SST experiment, since Nimbus has an inclination of about 100°. Hence, all the results mentioned below are also valid for that particular experiment.

We used the techniques of covariance simulation to study the experiment to determine what the correct estimation techniques should be for extracting information from the data and, in a sense, to evaluate the experiment, to

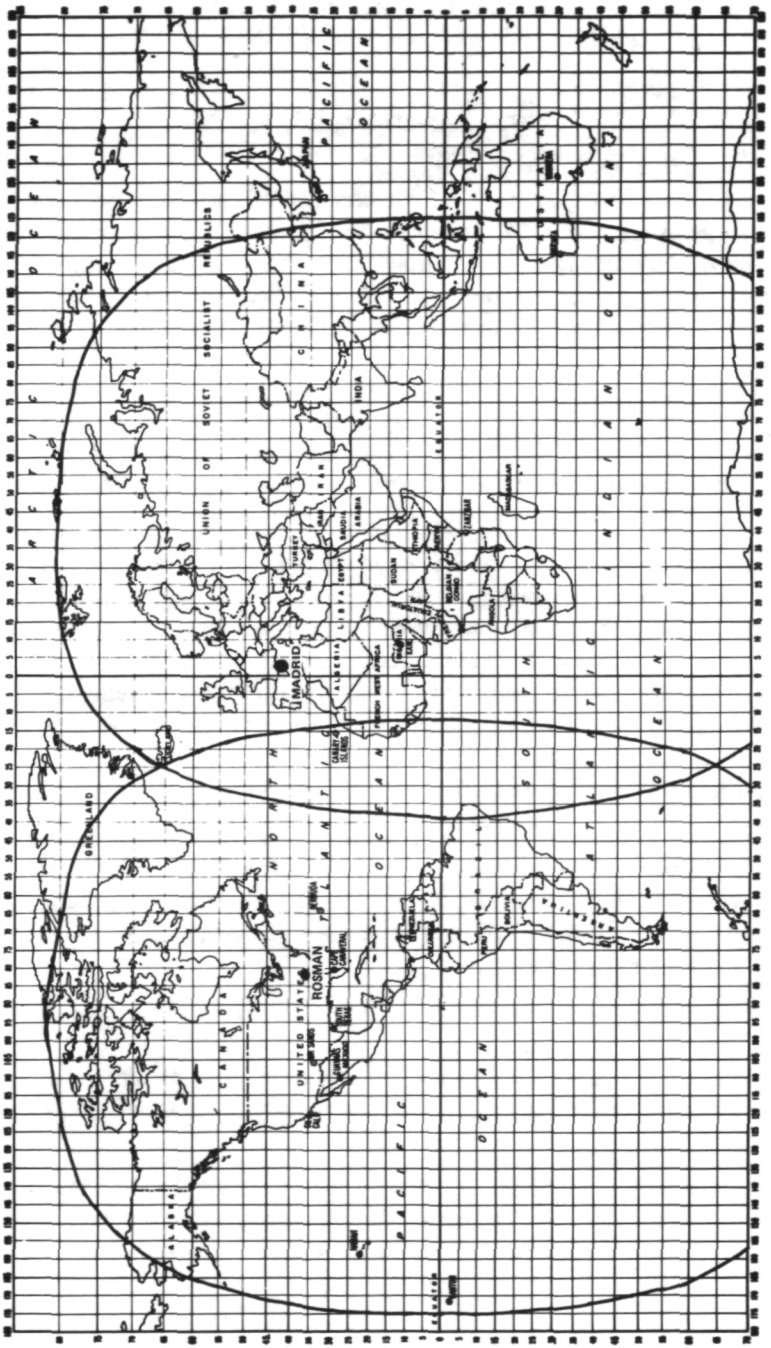

Figure 1. Visibility from ATS-6 for Rosman and Madrid.

see how well we could optimally do. The assumptions of our covariance simulation are listed below. We assumed 5 days continuous tracking from each of the prime geosynchronous positions of ATS; we assumed range-rate sum data, an integration time of one minute, and, for that integration time, we were able to assume an accuracy in the data of 0.3 mm/s. That is independent of bias and gave us about 14,000 observations.

Tracking and Systematic Error Assumptions

Data type	(1)*	Range sum rate
	(2)*	Range sum rate
Data rate	(1)	1/min
	(2)	1/min
Arc length	(1)	5 days
	(2)	5 days
Data noise	(1)	0.03 cm/s
	(2)	0.03 cm/s

Error Source		Standard Deviation
Rosman survey error		10 m in each component
Madrid survey error		10 m in each component
Data bias	(1)	0.1 cm/s
	(2)	0.1 cm/s
Relay (ATS-F) satellite epoch state	(1)	300 m in each position component; 0.3 m/s in each velocity component;
	(2)	300 m in each position component; 0.3 m/s in each velocity component
GEOS-C satellite epoch state	(1)	50 m in each position component; 0.05 m/s in each velocity component;
	(2)	50 m in each position component; 0.05 m/s in each velocity component

*1 = Rosman data arc; 2 = Madrid data arc.

The systematic error sources were the Rosman and Madrid survey errors, 10 meters in each component; large data biases; and uncertainties in four satellite epic states, two for each data arc–one for the high satellite and one for the low satellite. The covariance simulation assumed that all these systematic error sources, together with a full geopotential field to degree in order 8, were simultaneously adjusted in the data.

The standard deviations we attained for the geopotential terms were then compared with the standard deviation of our present estimates of the field, which I obtained from Frank Lerch of the Goddard Space Flight Center, who calibrated his Goddard Earth Model-5 geopotential field against independent observations of surface gravity data. He then scaled his nominal covariance matrix to be statistically compatible with the size of the residuals. We took the Lerch standard deviations and divided them by our standard deviations from the resulting simulation to obtain what we call factor improvement numbers, which can be seen in figure 2, for the cosine terms of the geopotential field. The sine terms were improved in a similar fashion.

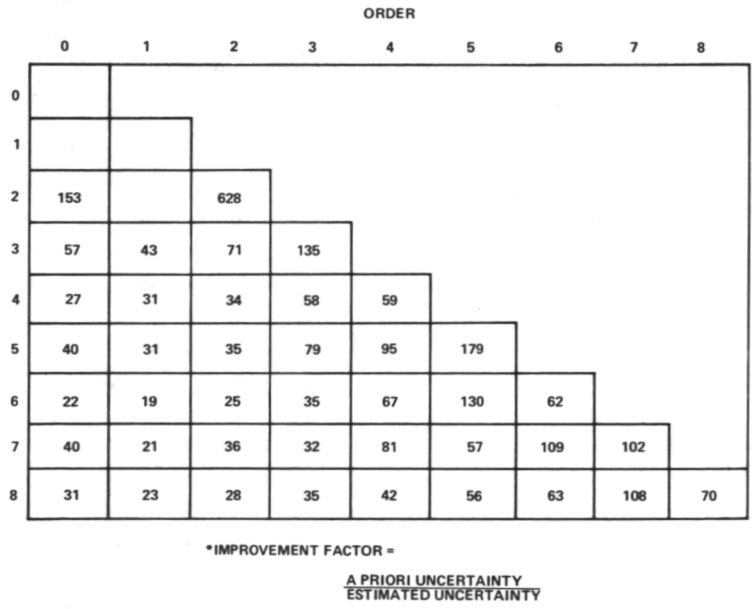

Figure 2. Improvement factor* in cosine terms for GEOS-C/ATS-6 geopotential determination experiment.

It can be seen that all the factor improvement numbers are significantly greater than 10, which would suggest that this experiment should provide more than an order of magnitude improvement in the knowledge of our low frequency terms.

Also important is the fact that the simulations show the correlation structure of the experiment was very good, with only about 150 of the 3200 correlations between geopotential terms of absolute value greater than 0.5 and none greater than 0.9. This is due, of course, to the almost global distribution of data. This simulation is to some extent optimistic, because it does not reflect the aliasing effect due to uncertainties in higher frequency terms, which presumably would not be adjusted in the data. This causes a systematic error which is called aliasing.

However, the covariance techniques are sufficiently powerful so that one can gain some concept of the severity of the aliasing effect. It does appear that aliasing is a significant problem for these experiments, and, that in order to obtain an estimate of the geopotential field to degree in order 8 in this sort of accuracy, it would be necessary to simultaneously adjust in the data of the experiment a geopotential field of at least a degree in order 12. Then it would be necessary to reject the estimates of the higher degree terms because of the aliasing effect.

Our conclusions are that the GEOS-C and Nimbus SST experiments should provide an order of magnitude improvement in our knowledge of the low frequency geopotential field and that this improvement should factor in the significantly greater accuracy in several critical experiments of the Earth and Ocean Physics Applications Program.

DISCUSSION

VOICE: Since I am somewhat associated with these two experiments, I would like to ask a question. When we started out, I didn't expect an improvement of that magnitude. Do you think it will really come to a factor of 10?

VOICE: I'm too pessimistic to sit here and say we have a great improvement by a factor of 10, and this is very significant.

VOICE: Is that a question or a comment?

VOICE: Both. I guess I have to wait for three months to see what GEOS-C is doing.

VOICE: I'll make the counter comment that you can get any results you want out of a covariance simulation.

VOICE: Very good. Here's an honest man.

VOICE: It depends on the validity of the assumptions. So the arguments should boil down to the validity of the assumptions, which I think do stand up.

VOICE: Yes, it was interesting when we did get the values to choose a 0.3-mm/s range rate; we got this in a recent test with ATS and Nimbus. So you have values in here which are not just assumed; they have been tested in the field.

VOICE: Those factor improvement numbers, of course, were 20, 30, and 40, so they may wind up to be 10.

IMPROVED DETERMINATIONS OF THE MASSES OF THE EARTH AND THE MOON

James W. Ryan

In 1971, I was involved with an experiment to use Mariner-9 as a target of opportunity for the unified S-band tracking network. The purpose of the experiment was to gain extremely high accuracy, high quality, three-way Doppler tracking data that we could use to determine the geodetic parameters of the Apollo sites.

Mariner-9 was launched in May 1971, and we acquired and reduced our data that summer. In the fall of that year, I reported to the Significant Accomplishments in Science and Technology review that we had completed a successful experiment and had new coordinates. Those coordinates were used in the final three Apollo missions and are still in use at Goddard.

When our analysis was completed we realized that we had a data set—the Deep Space Network two-way Doppler and range data— and a set of computer programs that were uniquely suited for determining the mass of the earth and perhaps also the mass of the moon.

Figure 1 shows the geometry for launch injection for Mariner-9 which was launched late in the day on May 30, 1971, in a direction away from the position of the moon. This minimized the effects of the moon on the trajectory.

After approximately two hours the spacecraft was moving in a very simple, three-body motion system involving the sun, the earth, and the moon. At this time, the probe trajectory was directly sensitive to the gravitational constant of the earth and also had some direct sensitivity to the gravitational constant of the moon.

In the first 24 hours, the speed of the probe was reduced by approximately 2 km/s directly as a result of the central body term of the earth's gravitational field.

Later, as the probe proceeded away from the earth, approximately a week into the trajectory, it was effectively beyond the gravitational effects of the earth-moon system; it was in a very simple, heliocentric trajectory.

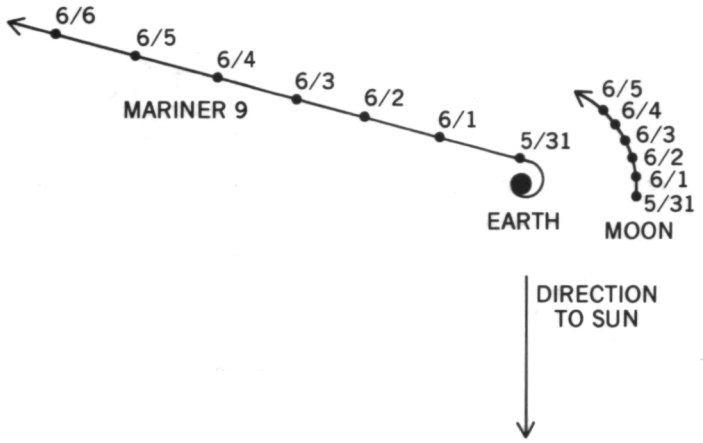

Figure 1. Mariner-9 injection geometry, launched May 30, 1971.

At this time, the data were directly sensitive to the earth-moon mass ratio. This arose because the probe moved at a very smooth trajectory relative to the baricenter of the earth-moon system whereas the tracking stations were rotating about the center of mass of the earth. A sinusoid was impressed on the range and Doppler data with the 28-day period.

We analyzed the tracking data from about 35 days after launch, and we believe we have successfully recovered the mass of moon and the mass of the earth from this data. We also recovered spin axis distances and longitudes of the Deep Space Network sites.

Figure 2 contains the results for the gravitational constant of the moon. Plotted here, as a function of time of their publication, are some of the most recent determinations of the mass of the moon. Note that our value agrees very, very closely with the value by Sjogren at the Jet Propulsion Laboratory (JPL), which was published in 1973, and that the values by Lui Lang, and Micheal and Blackshear well outside our uncertainty—and also outside of Sjogren's uncertainty.

We don't believe that we have actually improved the value that Sjogren recovered; his uncertainty is smaller than ours. However, it is important to note that Sjogren's work was done with a lunar satellite, directly sensitive to the gravitational constant of the moon, whereas ours was done with the deep space probe, primarily involved in recovering the earth-to-mass ratio, and having available a good determination of the mass of the earth.

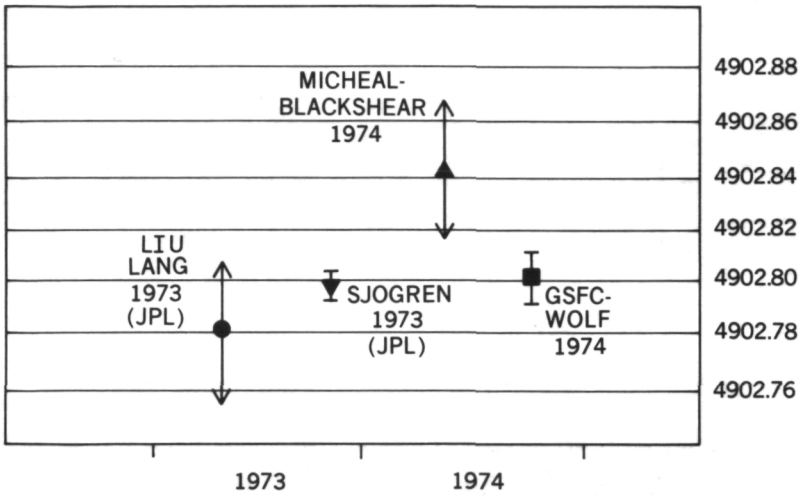

Figure 2. Gravitational constant of the moon Gm_m (km^3/s^2).

Figure 3 shows our recovery from the gravitational constant of the earth. This is important and is a part of the applications program. If you wish to determine the satellite height over some remote area, it is extremely important that you know the semimajor axis of the orbit because it is scaled to satellite height. However, the semimajor axis is not actually observed in tracking data, but rather the period is observed, and it is observed extremely well in tracking data. But the relationship between the period and the semimajor axis involves the gravitational constant of the earth; any error in the gravitational constant of the earth immediately maps into the estimate of height.

By reducing the uncertainty in the determination of the gravitational constant of the earth, we in fact really reduce the uncertainty and improve the accuracy of interpretation of such things as laser data and satellite altimetry data.

Our result is not appreciably different from the latest JPL results published in 1973, but we do believe that the uncertainty in our result, which was deduced from a very thorough error analysis, is less than half that of the latest JPL results. It is reduced from about 6 parts per million to about 2.5 parts per million.

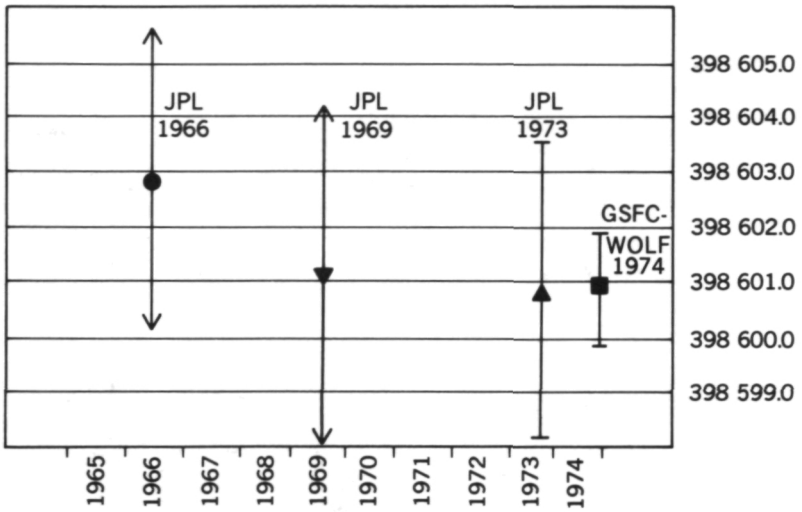

Figure 3. Gravitational constant of the earth Gm (km^3/s^2).

DISCUSSION

RYAN: The gravitational constant is relted directly to the mass of the earth, and it is the number which appears here: the formula for computing the acceleration of the earth on the spacecraft.

VOICE: It is really not the gravitational constant, it is Gm.

RYAN: It is a product of the gravitational constant and the mass of the earth. But that is the important factor for the satellite orbits.

SHORT PULSE OCEAN SENSING

David M. LeVine and Jerome Eckerman

Among the systems which show promise for sensing the ocean surface is a short pulse radar aimed near nadir. I am going to describe some results from our analysis of the potential of such a system for sensing the sea. This analysis consists of modeling the scattering process associated with short pulses to determine what information about the surface is contained in the power scattered back to the radar. I will outline the modeling which has been done and then present a comparison of the theory with the experiment.

Figure 1 shows the idealized geometry used in the modeling. The geometry is two-dimensional with no variation perpendicular to the screen. This figure represents a radar that transmits a short pulse which is assumed to strike the surface and scatter back to the radar. The surface is represented by a composite of a large-scale and small-scale random function. The large-scale random function roughly represents the gravity wave structure of the surface; the small-scale random function represents the capillary wave structure on the surface. The radar antenna is assumed to generate a beam that is pointed roughly near nadir so that α_0, the pointing angle, is small. In addition, the antenna is assumed to have a narrow beam, so that the illuminated footprint, L, is small compared to the distance from the antenna to the surface.

The first step in the analysis is to compute the scattered fields. This is done by using a physical optics approximation to solve Maxwell's equations. The solutions are then specialized to the case of far field (that is, when the antenna is far from the surface) and to the case of backscatter (that is, when the fields scatter back to the source). These solutions for the fields are then used to calculate the spectrum (that is, Fourier transform) of the power scattered back to the source. The results are shown in figure 2.

The $P(\nu)$ in this figure represents the magnitude of the spectrum of the power scattered back to the source. It is a produce of a constant, P_0, which depends on the radar cross-section of the surface, a function $I(\nu)$, which depends on the spectrum of the transmitted pulse, an exponential whose rate of decay depends on the pointing angle, α_0, and on the rms value of the wave height, σ_z, and finally, a function, sinc $(b\nu)$, whose parameter, b, is a function only of geometry, in particular of the pointing angle, α_0, and of the illuminated footprint, L. The information about the surface is contained in P_0, which is proportional to the radar cross-section, and in the rate of decay of the exponential which depends on the rms value of wave height.

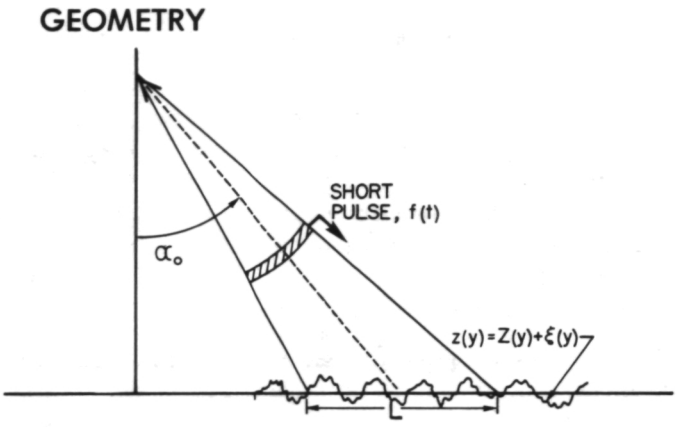

Figure 1. Short pulse ocean sensing.

When short pulses are transmitted, $I(\nu)$ can be very broad compared to the other factors in $P(\nu)$, in which case the last two factors in the spectrum are the dominant terms. An example of this case is shown on the bottom of figure 2 in which the spectrum for a short gaussian pulse is graphed. Based on this theory, the zero frequency term in this graph is a measure of the radar cross-section, and the decay gives a measure of the constant, a, and therefore a measure of the rms wave height, σ_z.

The prediction, $P(\nu)$, of this theory has been compared with the results of the experiment and the comparison is shown in figure 3. This figure contains a representative spectrum from data taken over the North Atlantic in September 1973 (left) and the prediction from the theory (right) for the case corresponding to the experiment. Notice the oscillatory nature of the spectrum obtained from the data and the corresponding oscillatory nature of the spectra predicted by the theory.

A check of these two spectra has been made by comparing the position of the nulls in the spectrum from the experiment with the position of the

$P(\nu)$ = MAGNITUDE OF AVERAGED POWER SPECTRUM

$$= P_0 \; I(\nu)\, e^{-2(a\nu)^2} \; \mathrm{sinc}\,(b\nu)$$

WHERE

$$b = \frac{2}{c} L \sin a_0$$

$$a = \frac{2\pi\sigma_z}{c} \cos a_0$$

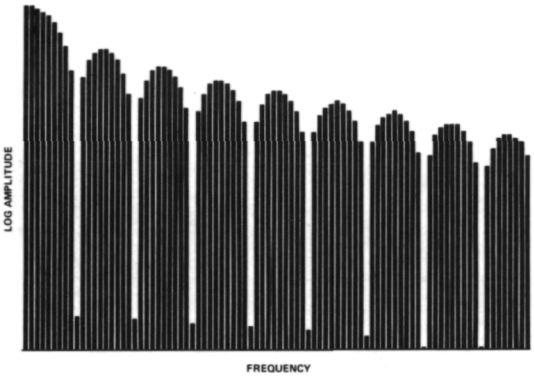

Figure 2. Spectrum of scattered power.

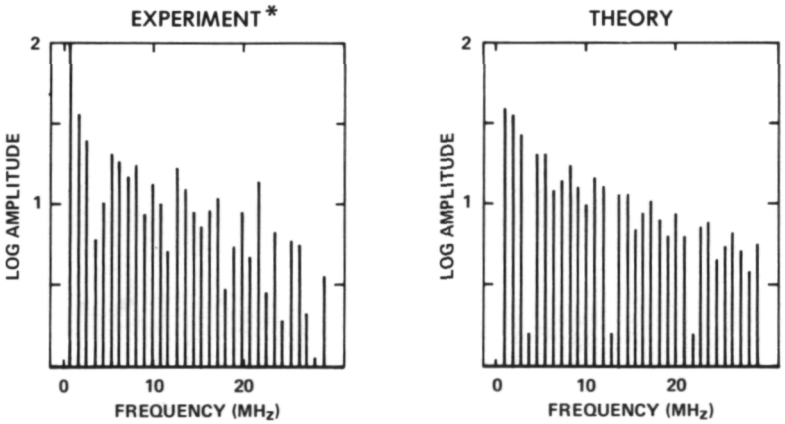

* JONSWAP
NORTH ATLANTIC
SEPT., 1973

Figure 3. Comparison of theory with experiment.

nulls in the spectrum from the theory. This constitutes only a preliminary check, but the agreement has been good enough to warrant some confidence in the theory, and certainly sufficient enough to warrant further pursuit of the theory.

The analysis is continuing and at present we are working to obtain better spectra from the experiments and to obtain measures of the surface parameters for comparison with ground-truth data.

MULTICHANNEL MICROWAVE RADIOMETER ANTENNA SYSTEM

John L. King

The Arctic-Ice Dynamics joint experiment (AIDJEX), Bering Sea experiment (BESEX), and other multichannel microwave radiometer experiments, which have been flown by Goddard and others on aircraft over the past several years, have demonstrated the usefulness of multichannel microwave radiometers for determining such items of interest as sea surface wind speeds, sea temperature, and sea ice thickness. These experiments, as well as the Nimbus-5 electronically scanning microwave radiometer (ESMR) images, are providing data that are of great interest to shipping firms which have to operate in the Arctic regions as well as to meteorologists and oceanographers. During these aircraft experiments, a conglomeration of several separate antennas was used on the aircraft to provide the required coverage. These antennas included 19-GHz electronically-scanned phase arrays, large fixed arrays, and horns located on many areas of the aircraft, with the total antenna complement weighing many hundreds of pounds.

To make multifrequency microwave radiometer measurements on a spacecraft, a much more compact antenna system weighing less than 20 kg was needed. To meet this requirement, Goddard Space Flight Center has proposed a mechanically scanned offset reflector system such as is now being implemented on the Nimbus-G scanning multichannel microwave radiometer. Such a system requires dual, linearly polarized feed systems capable of illuminating the reflector at 5, 10.7, 18, 21, and 37 GHz simultaneously from a common, single feed point with a single phase center. The offset reflector geometry, such as its focal length-to-diameter (f/D) ratio, is a critical factor in determining the feed design as well as in determining the optimum cross-polarization characteristics of the signals. For the Nimbus-G case, an f/D of 0.25 appears most suitable because of the particular spacecraft configuration, but higher f/Ds would be an advantage on future spacecraft to increase the cross-polarization isolation and improve the overall efficiency of the microwave antenna system.

The supporting research and technology (SRT) program is investigating these cases and attempting to optimize the performance of this antenna which has to operate over a 7:1 frequency range.

Shown at the top of figure 1 is the antenna feed system developed to illuminate a 0.25-f/D reflector. This particular model was fabricated and tested by RCA, and it does provide reasonably good coverage of the C-band, X-band, K-band, and K_a-band frequency ranges. It has a little higher spillover than would be desired, but, at present, it appears to be the best approach for feeding the low f/D Nimbus-G reflector. If you want to go to a higher f/D reflector, however, this feed would not be suitable because of the beamwidth.

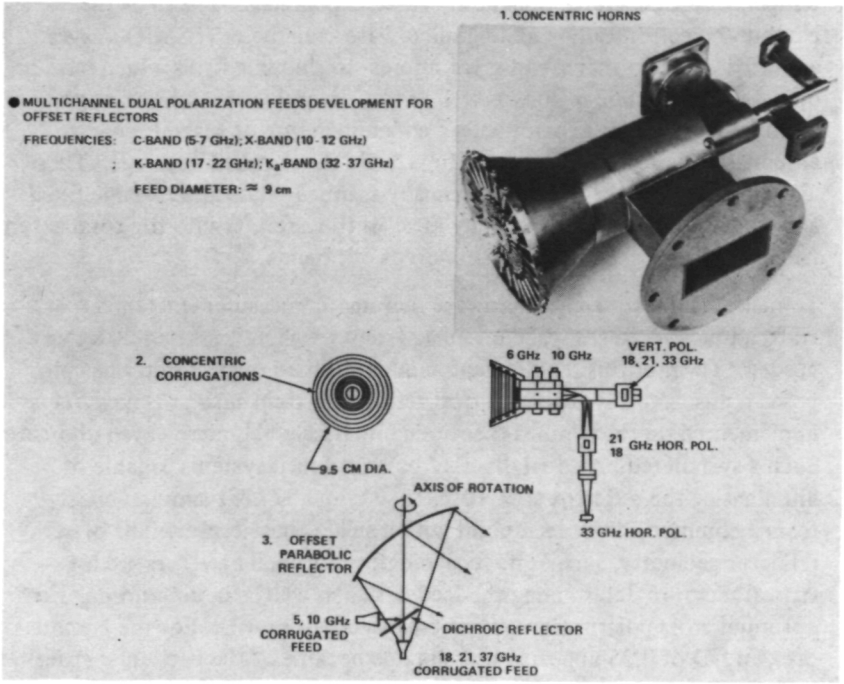

Figure 1. Multichannel microwave radiometer antenna systems.

The second feed which we have been developing for the past year is the concentric corrugated feed. It uses the corrugated mode, with one horn designed to operate at the 6- and 10-GHz frequencies and a second horn, located in the center, designed to operate at 21-, 18-, and 33-GHz frequencies.

Another critical factor in building any of these feeds is the orthomode transducer which is required to separate the vertical and horizontal polarizations with high isolation and low insertion loss.

The RCA concentric horn feed uses a straightforward approach which is somewhat narrowband. The second feed uses a fin-line orthomode transducer structure, and preliminary data indicate the possibility of providing very wide bandwidth and high isolation characteristics which we will want in future models.

A third way of feeding this offset, mechanically scanned reflector is shown at the bottom of figure 1. In this system, we use a reflective dichroic material to create two focal points. This material reflects at 5 and 10 GHz to illuminate the reflector, and it is transparent at 18, 21, and 37 GHz.

This has the advantage of being able to use very straightforward, low-cost corrugated horns for the primary feeding functions without getting into the complicated concentric configurations.

The disadvantage of the dichroic mirror approach is that it requires a rather large area to configure. However, it appears to offer a substantially higher performance for the larger spacecraft such as the Space Shuttle or the Earth Orbiting Satellite.

Figure 2 shows the corrugated horn pattern taken recently. It shows that at 6 GHz, this dish would be suitable for feeding a f/D of 0.25 reflector, although it could also be used to feed a higher f/D reflector with less illumination taper.

In figure 3, the three antenna patterns are overlayed with almost a 4:1 frequency separation. The patterns deviate somewhat at the 5- to 10-dB taper range but are still capable of providing reasonable illumination to the reflector for achieving good beam efficiency.

In figure 4 the antenna patterns for the entire 7:1 frequency range are overlayed, and it is apparent that we still require further development. The 33-GHz feed pattern is too narrow for this larger f/D reflector. However, if we chose to use a reflector with an f/D of about 0.35 to 0.4, this feed could be used to feed an offset reflector providing somewhat lower secondary beam efficiency than desired.

We have built two feed systems which appear to offer a good opportunity for achieving the antenna system's beam efficiencies which will be required on future spaceborne, multichannel, microwave radiometer systems.

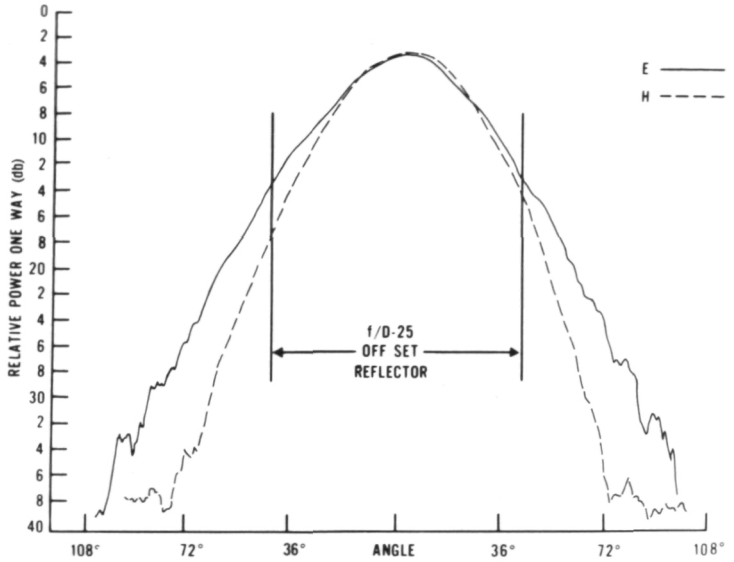

Figure 2. Corrugated horn pattern, 6.6 GHz.

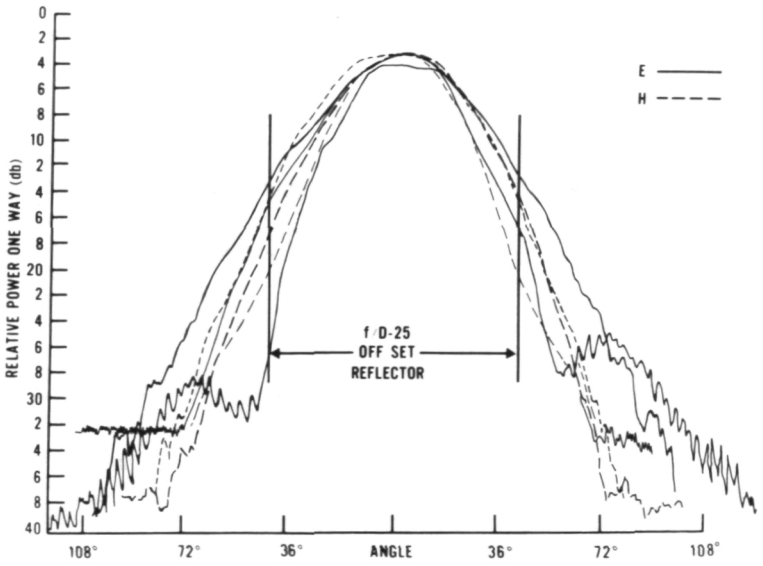

Figure 3. Corrugated horn patterns, 6.6 GHz, 10.2 GHz, 18.5 GHz, 21.5 GHz.

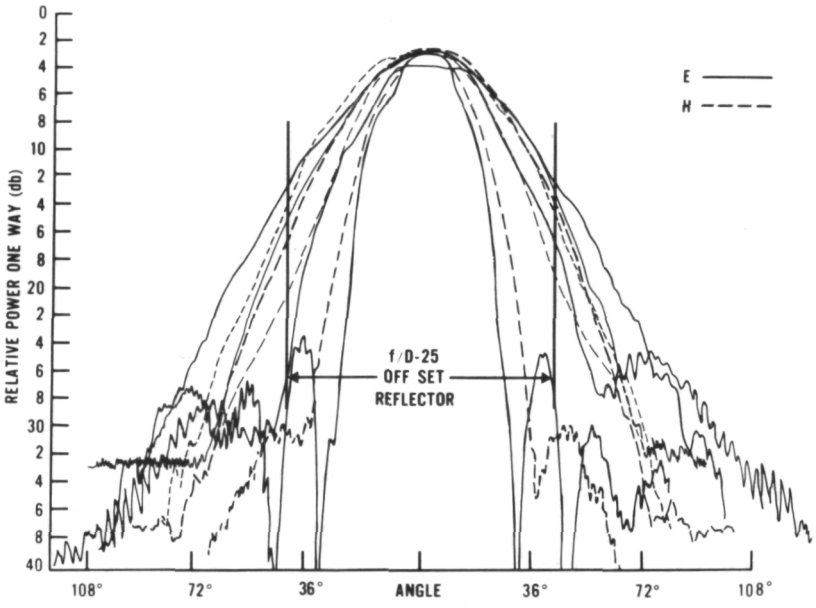

Figure 4. Corrugated horn patterns, 6.6 GHz, 10.2 GHz, 18.5 GHz, 21.5 GHz, 33 GHz, 336 GHz.

ERTS MEASUREMENT OF MASS OF SAHARA DUST IN THE ATMOSPHERE

Robert S. Fraser

Air pollution is becoming a worldwide ecological problem and may cause some drastic climate changes. In order to develop efficient control measures, the aerosol distribution and its dynamics over the entire world should be determined. Satellites have the potential for measuring aerosol characteristics. Currently, the aerosol mass can be derived from satellite measurements under restricted conditions, but no operational method has been developed. We are investigating the use of the multispectral scanner measurements of radiants from ERTS to determine the mass of aerosols in the atmosphere. We shall show how the observations were used to determine the mass of Sahara dust in an outflow west of Africa.

The method consists of constructing an atmospheric model based on surface observations. The radiances computed for the model were found to agree with the values measured by ERTS. This fact gave us confidence in using the model to give the dust amounts. We made this study to understand the observations but do not suggest that this method is a viable operational procedure.

The ocean-atmosphere model was specified with the aid of observations taken from the surface by a NOAA research ship. The surface and ERTS observations occurred at the same time and were displaced by 50 km which was negligible because of the weak gradients.

The ship measured the surface albedo, solar transmission, and wind speed. The atmospheric turbidity was average for that month, and the sea was very rough. The water vapor content was given by a nearby African radiosonde station. These data, plus an estimate of the particle index of refraction, were used to construct the ocean atmosphere model.

The measured and computed radiances are given in figure 1. The absolute radiances have been converted to reflectivity because it is a more familiar unit. The data are given for the four multispectral scanner bands. The low reflectivity measured over Lake Tahoe is given. Here the atmosphere was extremely clean, and the lake was smooth. For the Sahara dust example, the circles give the measured values, and the squares give the computed values for the model based on surface observations. They

agree within 10 percent, which is excellent because there was no absolute calibration and because model computations have not been verified carefully with experiments. The close agreement between the measured and computed radiances give us confidence in using the value of the dust load obtained from the models.

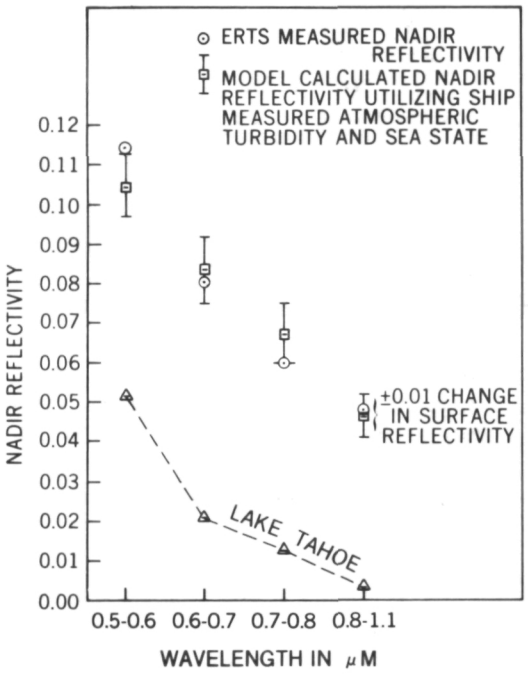

Figure 1. Measured and computed radiances.

The total mass of aerosols in a vertical column of the model is 1.6 g/m^2. The dust was concentrated between the heights of 1.5 and 5.5 km. The average concentration for this layer was 0.4 mg/m^3. The visibility in the dust layers would have been 30 km. The model and observations do not discriminate between dust and other particulates, but the other particulates contribute only a few percent to the total mass. Also, the observations are insensitive to particles larger than roughly 5-μm radius, but their mass contribution is likely to be small. Prospero has made observations of the concentration of the Sahara dust in the elevated dust layer, but only in the

western Atlantic region. He found concentrations one-seventh as large as reported here. However, the dust concentration decreases in its westward travel by means of fallout and dispersion.

The close agreement between the measured and computed radiances show that satellites can measure aerosol mass over water. However, the mass measurements are sensitive to small changes in the surface reflection and also to aerosol scattering characteristics. The surface reflectivity error has to be less than two-thousandths in order to restrict aerosol mass errors to less than 10 percent. The radiances of light scattered from each aerosol type, such as those that occur in dust, industrial areas, forests, oceanic regions, and so on, will have to be correlated empirically with the aerosol characteristics before satellite measurements of major aerosol properties become reliable.

DISCUSSION

VOICE: Roughly how much dust was there in the Sahara, compared to a typical, atmosphere?

FRASER: We do not know very well what the typical atmosphere aerosol loading is, but it appears that the loading on this case was about three standard deviations above normal for total mass loading.

VOICE: Did this show up if the ship was on the shore? Was there dust on the ship or . . .

FRASER: In this case, the surface visibility was very good. The dust was at 1.5 km above the ship. So at the surface there was very little dust. But, the dust for this case was not extreme. It was about the average of the dust flows from Africa. Heavier dust falls have occurred.

VOICE: From your knowledge about general characteristics, scattering characteristics of different types of aerosols in the atmosphere, would you say that a variation from one typical type of aerosol to another could cause twice as much or three times as much dust loading change in terms of these calculations?

FRASER: Yes. The measurements by Bartaneva indicate the back scattering inefficiency for dusts typically vary by an order of magnitude. Considering deviations from the mean to be three times the mean, we see that if the changes in scattering characteristics between different dust types are not accounted for, mass estimates can be in error by a factor of three.

THE ENERGETICS OF A TROPICAL STORM MONITORED FROM NIMBUS-5

John S. Theon, Mirle S. Rao, and Edward B. Rodgers

In order to understand the conditions under which tropical storms develop, intensify, and move, numerical prediction models have been developed to simulate their behavior. The energy transformations which generate such storms involve a conversion of internal and potential energy into kinetic energy. The energy equation in figure 1 indicates that in the total energy budget of a tropical storm we have the terms: latent heat from the water vapor flux that is advected into the storm, latent heat from the ocean that is convected from the surface, sensible heat from the ocean, and the remaining terms that are the main source terms, accounting for 100 percent. The loss terms on the right-hand side are net radiational heat loss, accounting for 3 percent; internal energy change, potential energy change, and kinetic energy change, accounting for the remainder. The first two terms on the left account for nearly all of the latent heat which, as can be seen, is better than 91 percent. For a rough approximation, the latent heat from the water vapor flux and the latent heat from the ocean surface, which are convected in, account for the latent heat released by precipitation. These figures come from the calculations of Riehl and Malthus (1961).

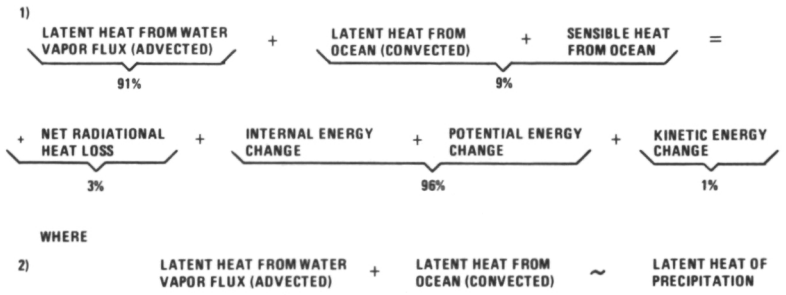

Figure 1. Energy budget equation for a tropical storm.

The problem of measuring the influx of water vapor is exceedingly difficult using conventional methods. Not only must the surface winds be measured

about the storm, but the specific humidity must also be evaluated. This has only been done on one or two occasions, at great expense and difficulty, by sending aircraft into storms to gather the required data.

The total latent heat released can be approximated by measuring the precipitation within the storm. Measuring the rainfall in a tropical storm was virtually impossible before the advent of the electrically scanning microwave radiometer (ESMR) aboard Nimbus-5. The ESMR, which senses the radiance of the earth and atmosphere at 1.55 cm, makes it possible to measure the rainfall rates over the oceans from an earth-orbiting platform. Briefly, rainfall rates were obtained by statistically matching the brightness temperatures measured from a skyward-looking microwave radiometer similar to ESMR with rainfall rates measured at the ground at Goddard during the summer months. These results were then utilized by Chang and Wilheit in a model which includes a tropical atmosphere with a standard raindrop size distribution to represent a given rainfall rate. The liquid water content of the clouds in the model was varied to match the experimental data. Finally, the model was used to compute the brightness temperature versus rainfall rate curve for the ESMR looking downward from space.

Using this calibration it was possible to monitor the rainfall for tropical storm Leila, which moved across the South Indian Ocean during January 1973. Figure 2 shows Leila on January 22, during the developing stage. The ESMR image is shown on the left, and the contour values of rainfall rate are shown on the right. From this quantitative map, total rainfall was computed for the circular area within a 2° of latitude radius of the storm center, as shown. The total rate of latent heat released was then computed. A similar procedure was followed in figure 3, which shows Leila in her mature stage on January 27.

Although the results compare reasonably well with those of Palmen and Rieh, who calculated the mean latent heat release from water vapor influx measurements for a steady-state tropical storm, these measurements do indicate the large variability in the energy budget of a tropical storm. The latent heat released by Leila during her developing stage was 38 percent less than that calculated by Palmen and Rieh. During her mature stage, Leila released 34 percent more latent heat than the Palmen and Rieh value.

Thus we have a new capability for providing the hurricane modelers with daily satellite observations of the energetics of tropical storms. Measurements such as these should improve our ability to predict the intensification and movement of tropical storms, thus saving lives and property.

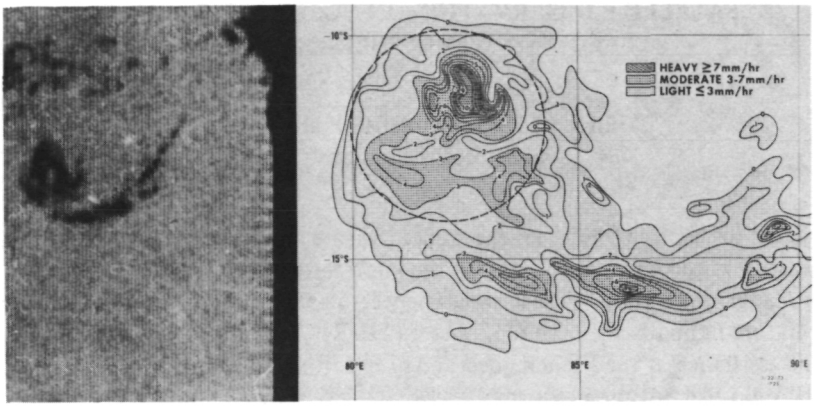

Figure 2. Tropical storm Leila, January 22, 1973, 1726 GMT.

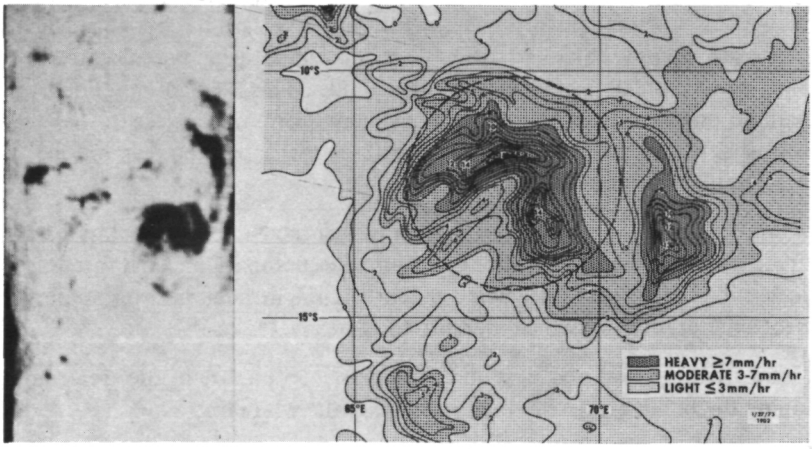

Figure 3. Tropical storm Leila January 27, 1973, 1902 GMT.

DISCUSSION

VOICE: Is the correlation between your calculations and the (inaudible) supposed to be obvious?

THEON: Not necessarily. For the rainfall intensity shown in those two images we used isoplethed values and then used a planimeter to calculate what the total latent heat release was, and there is, between rainfall intensity and latent heat release, a direct relationship, but it may not be obvious from those two figures.

SATELLITE OBSERVATION ON NUCLEAR WEAPON EFFECTS ON ATMOSPHERIC OZONE

Arlin J. Krueger, Cuddapah Prabhakara, and Ernest Hilsenrath

I want to describe briefly an experiment we are able to do with three of the sensors on the Nimbus-4 satellite: the backscatter ultraviolet (BUV) spectrometer, the infrared interferometer spectrometer (IRIS), and the temperature-humidity infrared radiometer (THIR). I also need to acknowledge the assistance of the French government in setting off a nuclear bomb at the right place at the right time.

Nitric oxide has been found to act catalytically in the destruction of atmospheric ozone; thus, very small concentrations, for example, parts per billion of nitric oxide, can cause reductions in parts per million in the atmospheric ozone. Actual atmospheric tests of this mechanism, which is known only from laboratory experiments, are very hard to conduct. Nuclear bombs are intense sources of nitric oxide. In fact, a single one-megaton bomb produces 10^{32} molecules of nitric oxide. This is an amount equal to about one percent of the entire global content of nitric oxide in the stratosphere. So the effect of a nuclear bomb test should be seen on the total ozone column in the atmosphere.

On May 30, 1970, we were fortunate in having the Nimbus-4 satellite pass directly over a bomb cloud about 3 hours after detonation. That satellite carried the backscatter ultraviolet system and the infrared interferometer spectrometer, both of which measure total ozone.

Figure 1 is the THIR scanning infrared radiometer picture of the area containing the bomb test site, which is given by the white dot.

This is the island of Mururoa at 22°S, 139°W, in the eastern Pacific Ocean.

In this picture the satellite moved from the bottom to the top, along the dashed center line, and ozone observations were made along that line. The most important observation is in the box in the center of the picture which contains the cloud from the nuclear test. We believe the semicircular cloud is the nuclear bomb cloud.

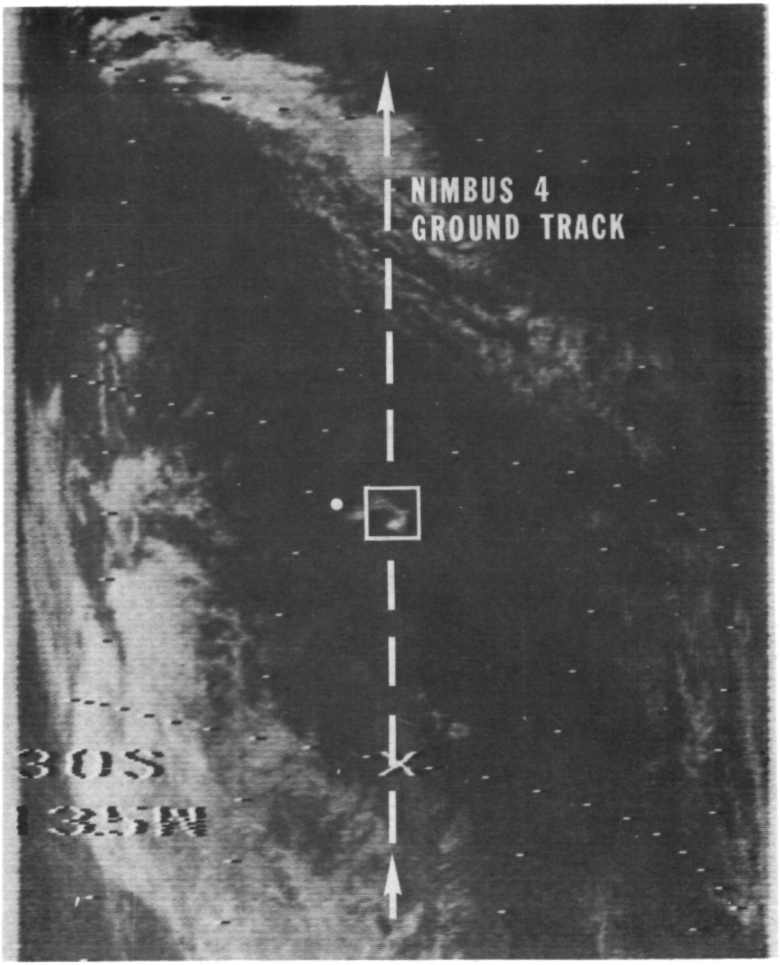

Figure 1. Nuclear cloud with BUV field of view and test site.

This test was about one megaton in size. Although other, larger tests were set off by the French and the Chinese during the lifetime of the satellite, in these cases the clouds were lost in the natural variability of the total ozone field, and a unique identification that is present in this picture was not possible.

It was fortunate that the satellite track did go directly over the cloud. It can be seen that if the satellite track had been a few degrees to the left or right, we would have missed this observation because the field of view of the BUV instrument, as shown by the white square, is about 200 km on a side.

For comparison purposes, I am going to give results from orbits at about 150°W on the day preceding the test and from an orbit at about 130°W on the day after the test.

Figure 2 shows the total ozone variations with latitude along those orbital tracks from the BUV. The results from the IRIS instrument are quite similar.

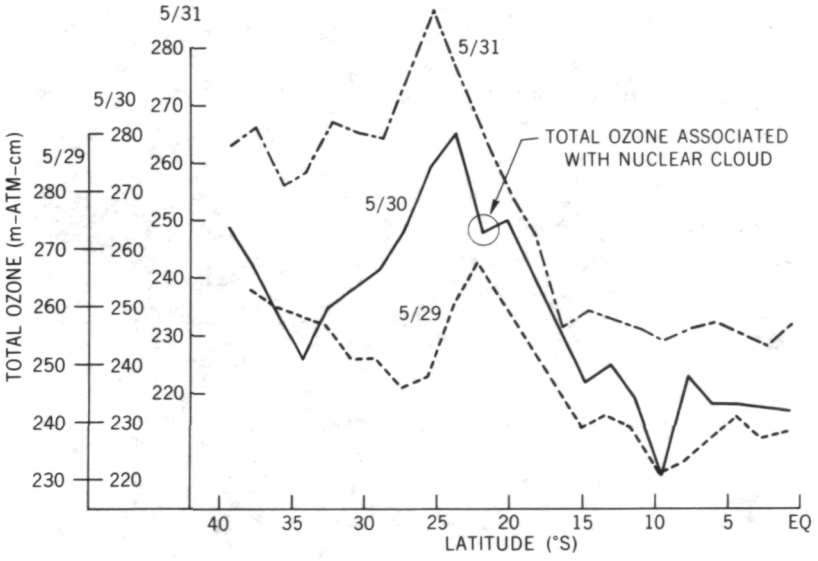

Figure 2. Meridional cross sections of total ozone, May 29, 30, and 31, 1970.

The lower curve is for May 29, the day before the test; May 30 was the day of the test; and May 31 was the day after the test.

The total ozone scales are for clarity. The circled data point is the measurement that is in the box in figure 1, and it is directly over the nuclear cloud.

To interpret the ozone change due to the nitric oxide from the bomb requires several assumptions. First, it must be assumed that the high altitude bomb cloud does not violate the inversion model conditions for both BUV and IRIS. Both systems give similar results in the total ozone-latitude curve, which is an indication that a real change occurred. Secondly, natural fluctuations of several percent exist at all latitudes. One must assume that

this present result is independent of those variations. Thirdly, a strong latitude gradient in total ozone is found in the vicinity of the test site on all three days. This gradient, starting at about 15°S and proceeding to 25° or 30°S, is what we saw on the day before and the day after the detonation. If we assume that the same gradient existed on the day of the test, then we can get a measure of the depletion of ozone due to the bomb.

There are data points about every 2.2° latitude in figure 2. There is one point over the bomb cloud, and the next point is at 20°S. One has to assume that this latitude gradient remained unchanged on the day of the test. If you make those assumptions, then the apparent depletion could be as high as 4 percent of the total ozone column of about 270 matm cm. This amount is comparable to the results of theoretical calculations by Julius Chang of Lawrence Radiation Laboratories, Livermore, California. He finds, under roughly the same conditions, perhaps 1- to 2-percent depletions in the total ozone content.

In conclusion, this observation is a beginning in the attempt to verify the interactions between nitric oxide and the atmospheric ozone under actual atmosphere conditions.

DISCUSSION

VOICE: You said an attempt to make similar measurements without a nuclear test were not successful because of the natural variability of ozone. Was this because the satellite pass was many, many hours later than the test? You said that there had been other nuclear tests, for example, by the Chinese and other tests by the French, which were larger tonnage, but you were unable to get measurements of the ozone depletion. What was the reason for this? Was it because of the timing of the satellite pass, or was there another reason?

KRUEGER: The satellite did not happen to go over the cloud at a time when we knew the cloud location.

VOICE: When you speak of the 4-percent depletion, you are talking about a very localized area. Is it the extent of one of your measurement points, 2.2°?

KRUEGER: The 4-percent depletion is the mean value within the field of view of about 2° latitude on each side, which is about 200 km.

VOICE: You said the BUV and IRIS data are the two sets of measurements. I understand BUV and IRIS, they are essentially different. BUV is more for the upper atmosphere, and IRIS is for the lower atmosphere. Do you see any dramatic differences?

KRUEGER: In the case of total ozone determination, the BUV makes use of contribution functions which are located low in the troposphere. The IRIS contribution functions look much like the ozone vertical distribution itself, weighted by temperature. We do not see any systematic differences because of the two types of contribution functions.

FINAL RESULTS ON FORECASTING IMPACT OF VTPR DATA

Milton Halem and Robert Jastrow

The results on the impact of vertical temperature profile radiometer (VTPR) data are not yet final because of the recent launch of NOAA-4 with new measurement modifications. However, Bonner of NOAA has reported zero impact of VTPR data from NOAA-2 on operational forecasting. The Goddard Institute for Space Studies (GISS) impact tests show a statistically significant 15-percent improvement in accuracy on 2- to 3-day forecasts when satellite data are assimilated. Why are the results of these tests different? We believe the answer lies in the data processing techniques developed by the two groups. The main difference is the factor of three in the GISS yield.

Figure 1 shows three curves indicating the results of tests designed to determine the impact of different VTPR yields and a fourth curve indicating National Meteorological Center (NMC) data impact. Each test consists of a series of six 4-day forecasts using the GISS general circulation model (GCM), but differing in the initial data sets. The initial data sets from which these forecasts are generated are determined in the following manner. At synoptic times during the forecast cycle, temperature, wind, and pressure data over land are borrowed from the NMC operational analysis north of 18°. Over the oceans, upper air radiosonde data are used. Aircraft reports and satellite-derived wind measurements over the oceans are not used directly, but the 300-mbar wind analysis at this single level is used instead. At the surface, pressure and temperatures from the operational analysis are used everywhere. In this way, we exclude the VTPR data from the analysis over the oceans.

The curve labeled NO VTPR shows the average rms surface-pressure errors over the United States obtained when VTPR data are withheld from the analysis. The curve labeled GISS VTPR full yield in figure 1 is obtained in a similar manner, except in this case, the full GISS-derived VTPR data are inserted into the model at each time and place of observation as acquired by satellite. A comparison of the two curves indicates the magnitude of the VTPR impact.

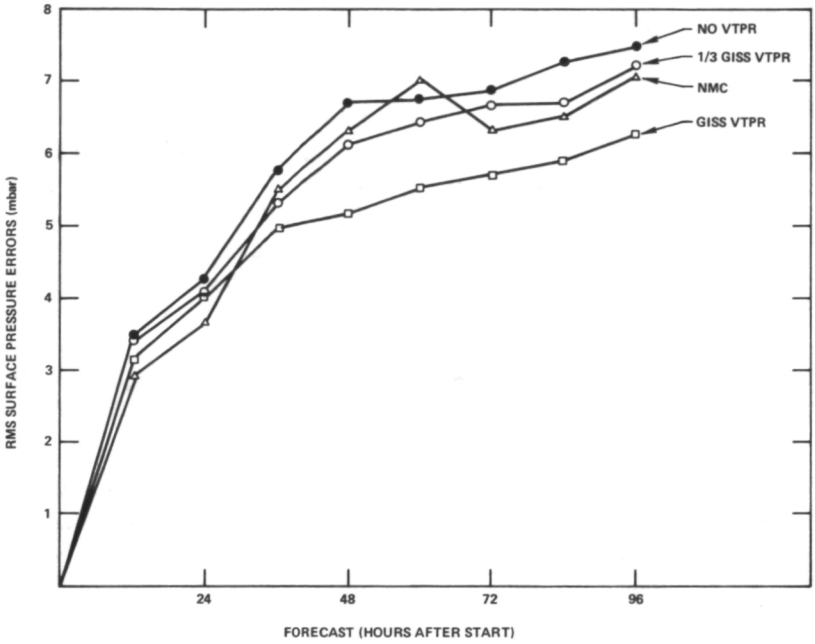

Figure 1. Effects of VTPR yield on forecast accuracy.

A second test was conducted to measure the effect of a reduced yield. Because the National Environmental Satellite Service (NESS) produces roughly one-third the GISS yield, a new data set similar to that leading to the GISS VTPR full yield curve, but randomly selecting one-third the GISS yield, was used. Forecasts from this data set are also shown in figure 1. This result should approximate the NMC impact.

To test this assumption, a third experiment, using the complete NMC operational analysis everywhere, including the operational VTPR sounding temperatures, was carried out. The results are shown in the curve labeled NMC forecast. NMC and the one-third-yield case errors are approximately comparable, as expected. The dotted lines indicate a 15-percent impact, small but statistically significant with nonoverlapping error flags not shown on the curve.

How important is a 15-percent increase in forecast skill? First, it is sometimes possible in a dozen or so cases that this difference can mean catching or missing a severe storm. For example, a major snowstorm hitting the

eastern seaboard from Washington, D.C., to New York last February 8 was missed in the 48-hour and 24-hour forecast; the New York Times carried the weather service prediction for sunny weather. The forecast using the full GISS VTPR data yield for this period indicated a very strong likelihood of snow in the 48-hour forecast; it did occur at the actual times and places predicted. Other improved meteorological features also show up as a result of this degree of improvement.

The second aspect comes from looking at NOAA's skill score record for the past 25 years as shown in figure 2. The impact of numerical weather modeling, computers, and increased radiosonde networks have produced a 22-percent improvement in 25 years.

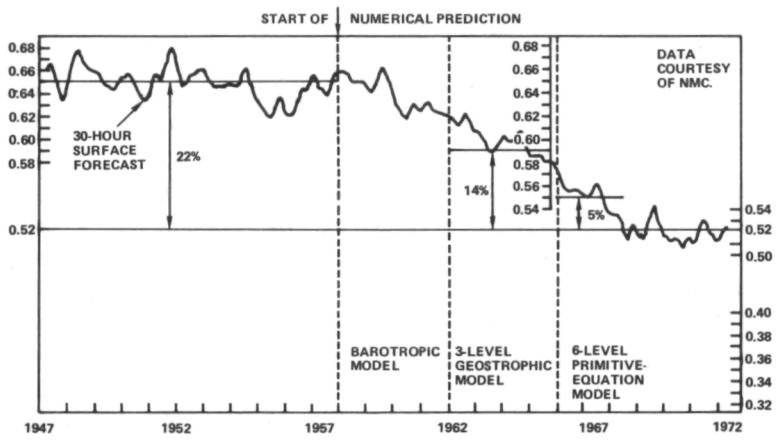

Figure 2. Twenty-five year skill score history of 30-hour sea level forecast.

The use of GISS data processing techniques by NOAA should produce an immediate improvement in the present accuracy of the 48- to 72-hour forecast, nearly as great as achieved in the last quarter century for the 30-hour forecast.

NEW METHODS FOR PREDICTING CLIMATE

Robert Jastrow and Milton Halem

Theoretical studies indicate no predictability in the climate forecasts beyond two to three weeks and, in practice, no skill beyond one week. The reason is that uncertainties in the initial states and errors in the observing systems are magnified by the nonlinearities and turbulence of the basic equations. All memory of the initial state is usually gone after a week.

It should be emphasized that the situation is very much like that leading to Schroedinger's equation. You cannot say where an electron is at any moment, but you can predict the probability of it being there. If you follow many electrons, they will be located according to this probability distribution solution. In the same way, you cannot say what the weather will be at a point in space or time, but, if you calculate over many cases, the average should give the weather.

If you ask something practical, for example, what will the average surface temperatures and rainfall be over a million square kilometers averaged over several days or a week or a month in advance, then information can be provided. This has only been a conjecture that we made and first tested with simulation studies. The way we tested the theory was to produce an ensemble of forecasts generated from 33 separate initial states distributed over a range of winds and temperatures that represent the uncertainties of the observing system. First, we produced the average of the ensemble and then averaged over different space and time volumes. The errors were found to be very small when compared to errors in climatology, errors in Farmers' Almanacs, and errors in NOAA's 30-day forecasts. Now, we wish to report on the first extension of this study to real data.

Figure 1 shows the region in the northeast and the stations selected for verification. Five forecasts were generated, one from the best available global state of the atmosphere and four others varying with probable observational uncertainties, that is, 1° over land, 2° over oceans, and so on. We ran the forecast for 14 days and, using the last 8 days, plotted this period as shown in figure 2. The average temperatures of the five forecasts and the observed temperatures are shown. The dashed line represents climatology during this period.

The criteria of judgment are how closely the temperatures follow the observations and the maximum single deviation. These represent the customer's

Figure 1. Northeast region of United States selected for forecast verification.

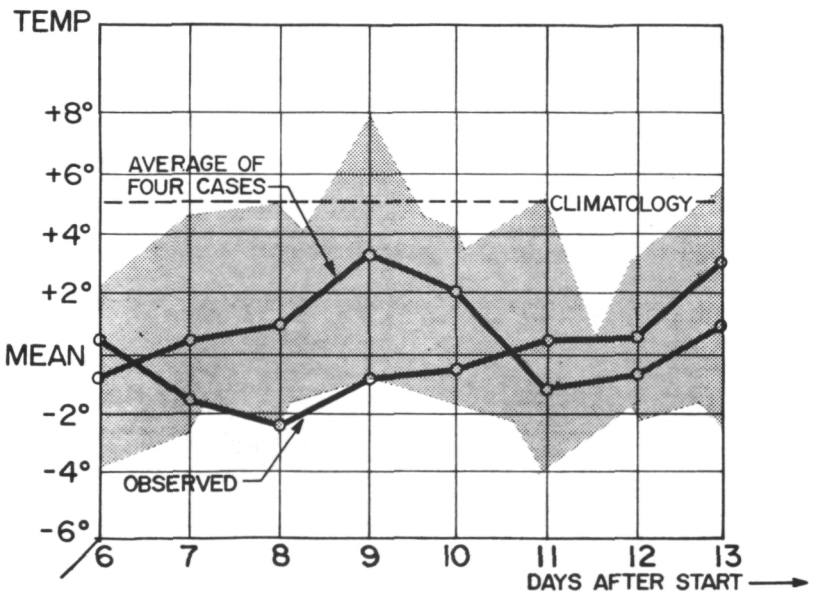

Figure 2. Two-week surface temperature forecast compared with hourly ground station report over the northeast United States (10^6 km^2).

interest. The rms is the most sensitive measure. In this case, the rms error for climatology in this region was 5.9° C. The rms errors for the individual cases range up to 4.5° C over the five cases, and the mean average is 3.6° C. When we computed the statistical ensemble with Schroedinger's equation, the error was cut to 2.5° C. Second, we found the maximum deviation for individual cases ranging up to 8°C as seen by the shading; when you take the ensemble average, the maximum error is 3.0°C.

This is really quite striking because what is involved here is the prediction of temperatures from one to two weeks in advance on a daily basis over a region. We are extremely encouraged. We think it is a real breakthrough on the type of forecast a farmer needs. What we have done is good for only 15 days because the boundary conditions change. For monthly forecasts and larger, we need Seasat-type data, Landsat data for ground albedo, and other available satellite data. We plan to combine this new theoretical approach with other satellite data into a real attack on the crop yield problem.

SMS-1 INFRARED VIEWS OF HURRICANE CARMEN

Edward B. Rodgers, William E. Shenk, and A. Fritz Hasler

The first Synchronous Meteorological Satellite (SMS-1) now provides us the capability, with the 11-μm channel on the visible and infrared spin-scan radiometer (VISSR), of viewing the clouds associated with weather phenomena on a virtually continuous basis. Since its launch in May 1974, SMS-1 viewed the 1974 tropical cyclone season over the North Atlantic and the Caribbean region mostly with a subsatellite point at 45°W. The most intense storm of this season was Hurricane Carmen which struck the Louisiana coast with 65-m/s winds.

Figure 1 shows the cyclone tracks of the 1974 season. Carmen was named late on August 30 as it reached tropical storm intensity with winds of 15 m/s south of Hispaniola. It became a severe hurricane on September 1 with winds greater than 50 m/s. The following day it struck the Yucatan Peninsula. As Carmen crossed the Yucatan Peninsula, it weakened but regained strength as it moved over the Gulf of Mexico on September 4. Carmen once again became a severe hurricane with winds up to 65 m/s late on September 7 before it reached the Louisiana coast. Upon reaching the coast on September 8, it weakened and finally dissipated over eastern Texas on September 10.

To highlight the film that was shown during the Significant Accomplishments review, six images of Carmen during its early period of explosive growth, between 0300 GMT on August 31 and 0600 GMT on September 1, are shown in figure 2. In this figure, the high opaque clouds are observed to be white, while the land and ocean regions are generally dark. Carmen is at the center of each picture.

During the earlier part of this period, an area of thick clouds near the center of the circulation is seen penetrating up to the tropopause and moving outwards, forming a dense cirrus canopy. This outward moving canopy delineates the upper level wind flow that diverges from the center of Carmen. As the canopy continued to expand outwards during the later part of this period, an area of clearing in the canopy is first evident to the south at 0000 GMT on September 1. The clear area then expanded north and westward by 0600 GMT on September 1. The circular clearing is caused by subsidence induced by the convergence of the outflow of Carmen

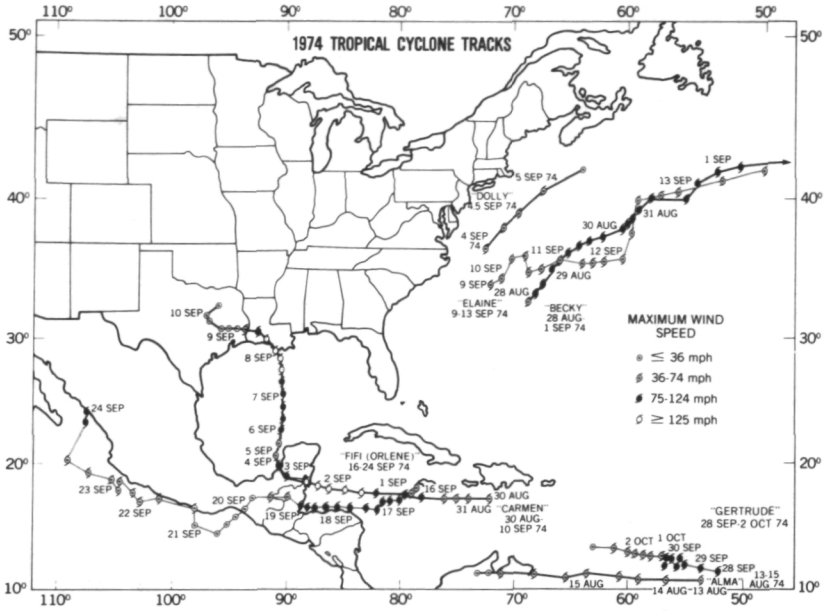

Figure 1. Tracks of the seven tropical cyclones that formed over the North Atlantic and Caribbean during the 1974 season.

with the surrounding air. This is an indication that the outflow has intensified. The outflow at the upper level is produced by upward vertical motion within the convective cells at the center; therefore, the stronger the outflow, the more intense the storm. Thus, this area of circular clearing is a good indication of the intensification of Carmen.

The line of clouds to the north of the dense cirrus canopy during the earlier part of the period was observed in the film to be rapidly moving away from the canopy towards the east-northeast. These clouds indicate a strong, upper level, west-southwesterly flow. This helps to remove the upward moving air and moisture from the areas of convection. This enhances the upward vertical motion within the convective cells.

It is evident that, from this continuous viewing of tropical cyclones, a much better insight into the evolution of the storms can be obtained. It has also given us a chance to observe the diurnal variability of tropical storms and their cloud structures.

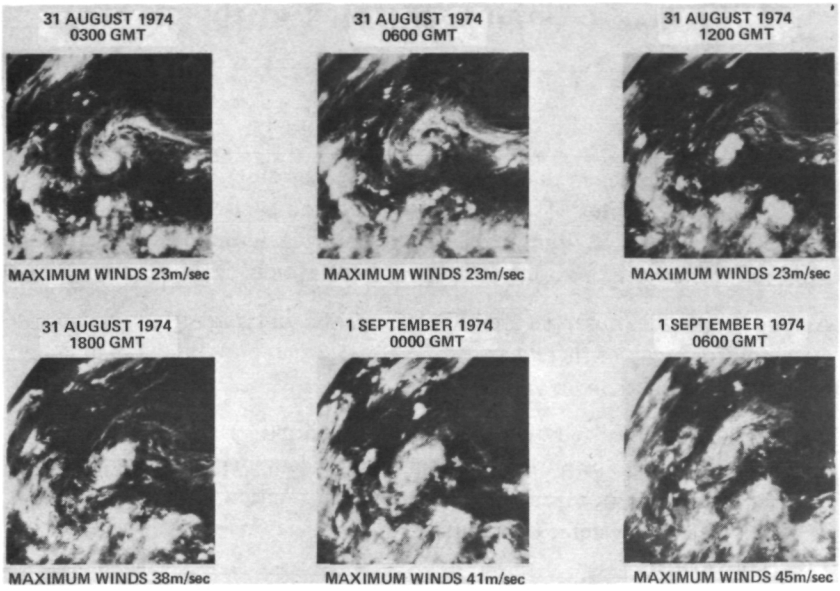

Figure 2. Six infrared images of Hurricane Carmen obtained from the SMS-1 VISSR sensor between 0300 GMT August 31, and 0600 GMT September 1, 1974.

INFRARED ASTRONOMY FROM EARTH ORBIT

Stephen P. Maran

Recently, we have begun to analyze infrared stellar observations made from U.S. Air Force satellites. The data consist of broad-band photometric measurements in the 2.7-μm wavelength region, which cannot be observed from the ground due to strong atmospheric absorption.

Among the sources observed are both long period and semiregular variable stars, and for many of these stars we have by far the most extensive and detailed infrared light curves yet obtained.

The observations received by us date back to February 1972, and new ones are still coming in. The group working on these data includes Tom Heinsheimer and Tom Stocker of The Aerospace Corporation, Hamilton Wright of Aerojet ElectroSystems Corporation, and Robert Chapman and Robert Hobbs of Goddard.

The first figure shows a light curve of Mira (omicron Ceti), the first star studied by us, and historically the first variable star that was known to Western astronomers. In the early days of infrared research at Mt. Wilson Observatory, Petitt and Nicholson discovered that the maximum intensity in infrared light occurs significantly after Mira reaches maximum visible light, and you can see this effect clearly in figure 1. It appears that the maximum visible light occurs at the phase of the cycle when the star is hottest, while the infrared maximum occurs near the phase when the star is largest, as shown by the computations of Strecker at the University of Minnesota.

Figure 2 shows our light curve for another long period variable star, R Aquilae. This is an example of what an astronomer will usually publish under the heading of "typical data," or in other words, his best-looking data. It should be noted that the plotted points do not represent individual observations; each point represents the mean of several observations made on the same day. The "bump" near Julian Day 2,441,700 (and probably also that at 2,441,410) is a real feature of the light curve, which is in need of a good theoretical explanation. A smaller bump or inflection point near Julian Day 2,441,750 may also be real; since it occurred near the time of maximum visible light as reported by the American Association of Variable Star Observers, it presumably indicates a slight temperature effect on the infrared light curve.

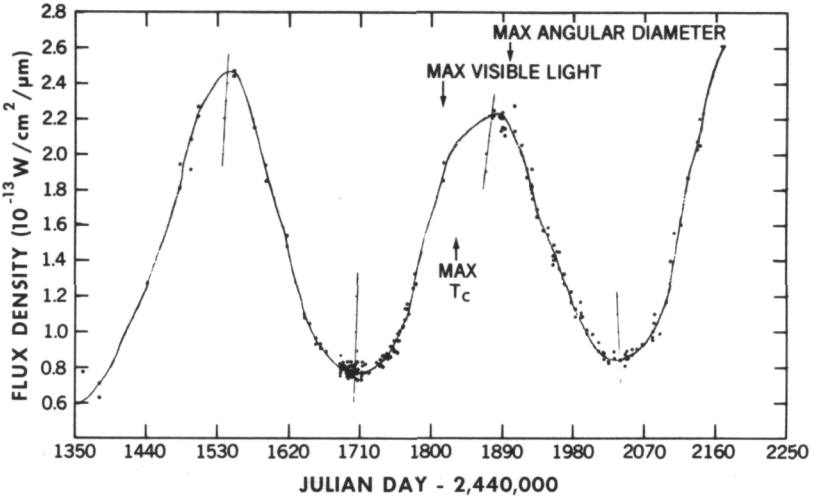

Figure 1. Satellite observations of the variable star omicron Ceti (Mira) from February 13, 1972, to May 12, 1974.

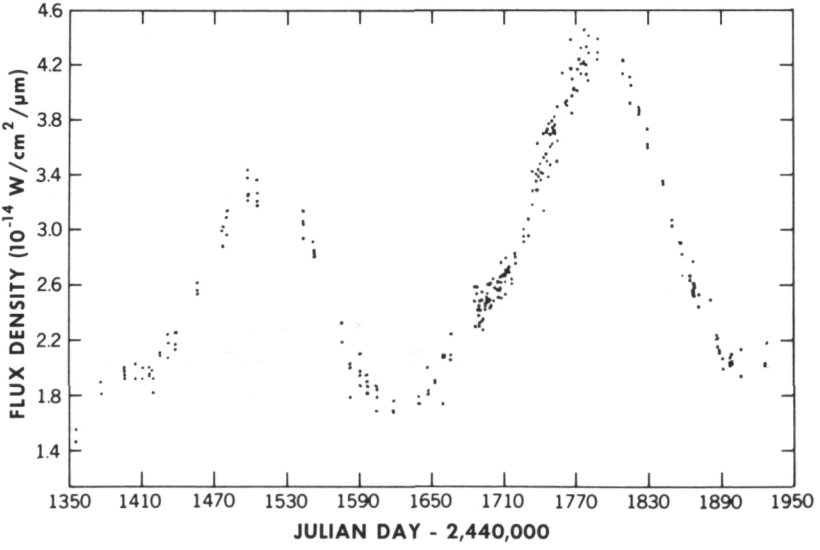

Figure 2. Satellite observations of the variable star R Aquilae from February 8, 1972, to September 3, 1973.

Some long period variable stars are associated with circumstellar clouds that produce radio emission in spectral lines of both the hydroxyl radical and the water molecule. The intensity of this radio emission varies roughly in unison with the infrared light, and indeed Litvak at Harvard University has suggested that the radio lines are produced by maser processes that are pumped by light emitted by the star in the wavelength range of our satellite observations. The molecular clouds are dynamically decoupled from the pulsating stars, as shown by the fact that the radio emission lines do not exhibit Doppler shifts that can be associated with the known motions of the star's photosphere.

We have compared the data shown in figure 2 with radio observations of variable OH and H_2O emission from the R Aquilae circumstellar cloud, and we find rather good correlations for both the ascending and descending branches of the light curve, as shown in figure 3. Different symbols here denote the respective branches of different cycles of the star. The linear relationships that are exhibited in these data would be predicted if the masers are saturated, and this is an important conclusion that should be checked by additional measurements.

This talk summarizes just our first analysis of a small sample of the Air Force satellite data that we have received. We are currently producing a modest atlas of infrared variable star light curves that will make this information available to interested astronomers and that will also serve as a basis for statistical analyses. We expect to learn much more about these stars as the work progresses.

DISCUSSION

VOICE: What is the nature of the stellar spectrum in the region observed photometrically with the satellites?

MARAN: According to the Stratoscope II findings, the most prominent spectral feature is the absorption band of water vapor. By contrast, the adjacent spectral bands that can be observed from the ground, at 2.2 and 3.4 μm, are essentially located in the stellar continuum.

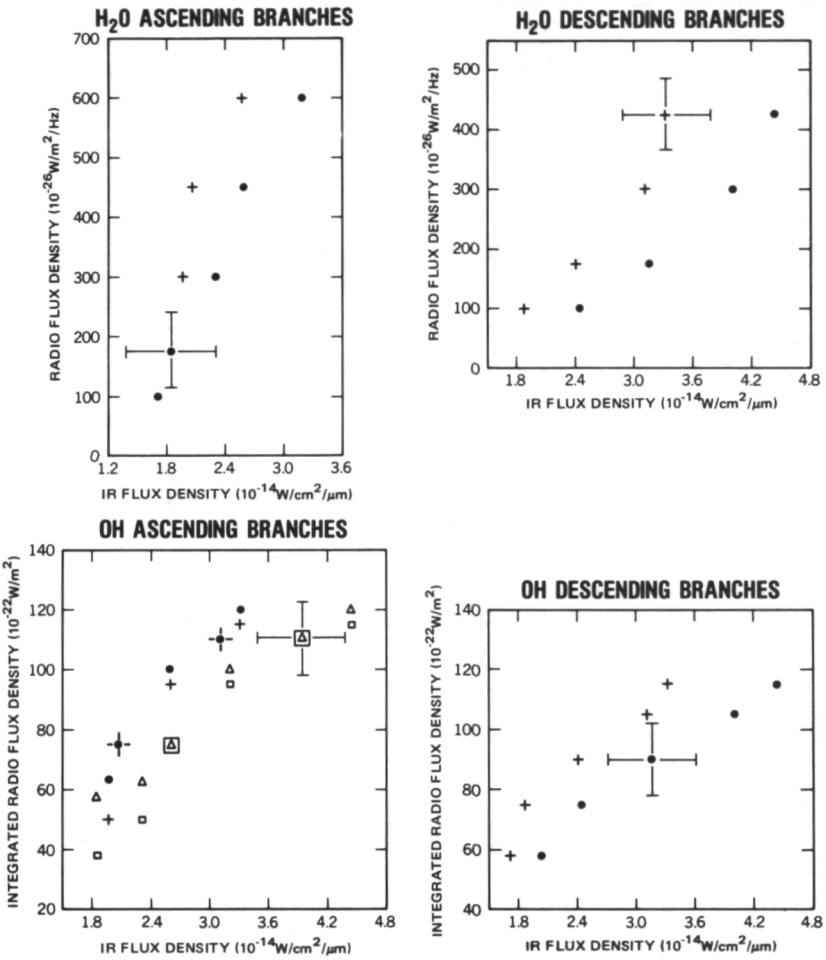

Figure 3. Relationship between radio emission (OH and H_2O lines) and infrared emission from R Aquilae.

INFRARED UPCONVERSION SPECTROSCOPY OF LABORATORY AND REMOTE SOURCES

Theodore Kostiuk

The infrared region of the spectrum is of great interest in astronomy since major constituents of stars, comets, interstellar clouds, and planetary atmospheres exhibit strong spectral emissions in this range. Unlike visible detectors, which can operate in the quantum noise limit, the sensitivity of IR detectors is considerably poorer, and more complicated systems have to be developed for the infrared in order to improve the signal-to-noise ratio for narrow-band detection.

One such system being developed in the Laboratory for Extraterrestrial Physics at Goddard is the infrared upconversion spectrometer. The upper part of figure 1 shows the principle of its operation. A weak infrared signal from a telescope is mixed with a visible laser in a mixing element. The resulting sum frequency generated is in the visible and has a one-to-one correspondence with the infrared frequency. This visible upconverted signal can then be readily detected with the high sensitivities available with visible photon-multipliers.

The main components of our instrument are shown in the lower half of figure 1. The beams from our IR source and the argon ion pump laser emitting 5145-Å radiation are combined at the beam splitter and mixed in a heated $LiNbO_3$ (lithium niobate) crystal. The upconverted beam is then separated from the high intensity pump laser beam at the pump light filter and monochromator, and subsequently detected with a photomultiplier. This spectrometer can be tuned from 2.7 to 4.3 μm by controlling the environmental temperature of the $LiNbO_3$ crystal and thus creating the conditions for mixing for particular infrared input wavelengths.

We have succeeded in accomplishing upconversion, and a recording of an observed He-Ne laser line at 3.39 μm is shown in figure 2. By scanning the temperature of our crystal (shown along the X-axis), we were able to tune the wavelength and observe the laser emission. It occurs at ~583 K (~312° C). The origin of the secondary peaks is as yet not known, but it is suspected that they are due to internal reflections in the crystal. (If the faces of the crystal are not parallel, any reflected beam will be at a slight angle to the axis and thus upconverted at a different temperature.)

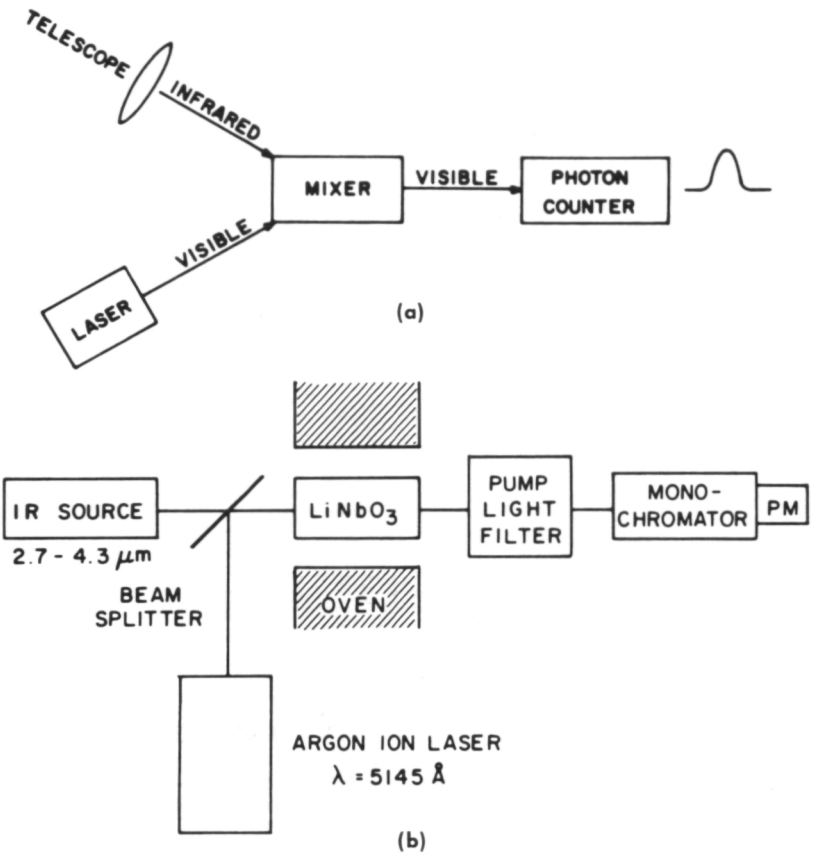

Figure 1. Infrared upconversion spectrometer: (a) principle of operation, (b) lower portion contains main components.

We have also succeeded in detecting 1300 K blackbody radiation in a narrow 6-cm^{-1} bandwidth, with limited optical alignment and focusing. The present performance of our instrument as well as its design goals are given in table 1. Almost no attempt has been made, however, to optimize the performance.

As can be seen, the minimum detectable power is 10^{-13}W. The system goal is 10^{-16}W, which is an order of magnitude better than conventional detectors. This number is closely linked to the system conversion efficiency which at present is quite low, ~0.001 percent, compared to >2 percent we hope to achieve. This discrepancy is primarily due to inefficient filtering of the pump laser, and at present we have the components to improve the number by 2 orders of magnitude. This in turn will decrease the minimum detectable

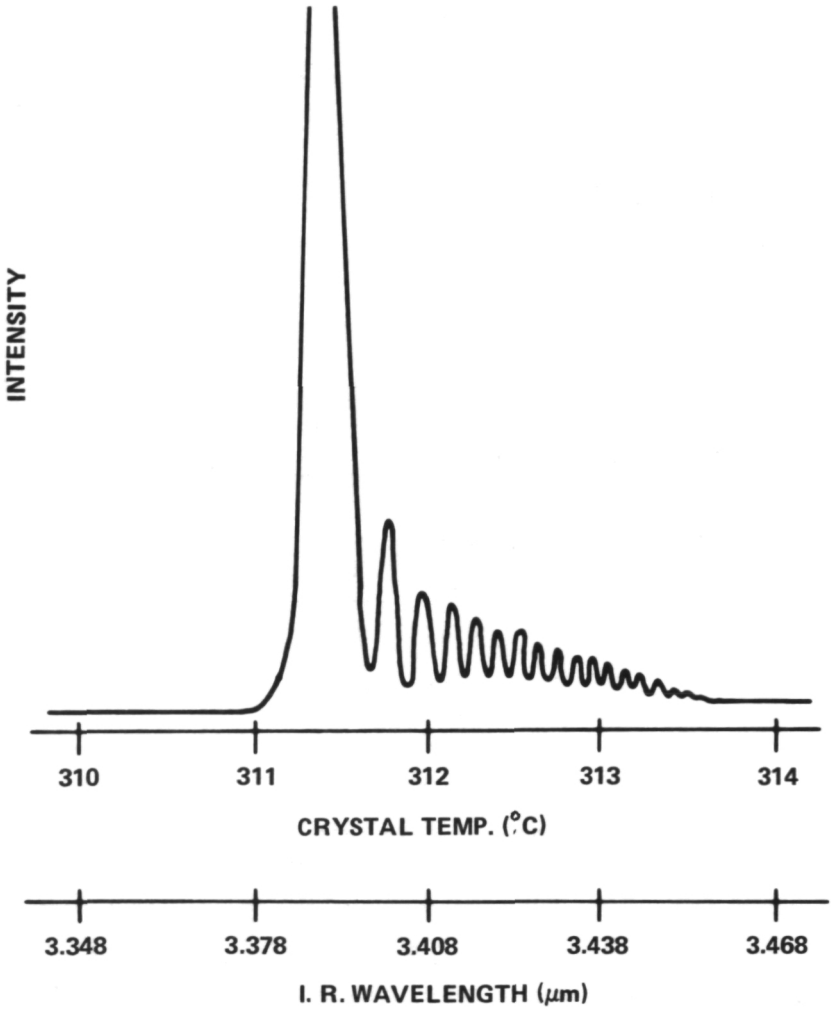

Figure 2. An observed He-Ne laser line.

power. The crystal quantum efficiency is, however, closer to the expected value and will approach it with improved alignment and increased pump laser power. The resolution is 2 parts in 1000 and is close to the theoretical value, as is the field of view.

Table 1
Infrared Upconversion Spectrometer

	λ_c	MDP (W)	N_c (system) (percent)	N_c (XTAL) (percent)	Spectral Resolution	Tunability (μm)	FOV (degrees)
Present Status	3.39	10^{-13}	0.001	0.4	$2/10^3$	2.7-4.3	<1
Design Goal	2.7-4.3	10^{-16}	>2.0	5.0	$1/10^3$	2.7-4.3	0.8

Unlike conventional infrared spectrometers, an upconverter does not require cryogenic cooling to achieve its ultimately high sensitivity, nor does it contain any mechanical constraints. The operating wavelength of the device includes the 3.8-μm atmospheric window. These properties of the upconverter, along with its relatively broad tuning range and relatively high resolution, make it a potentially useful instrument for astronomical spectroscopic observations. An extension of this technique can also lead to the development of an imaging upconverter capable of simultaneously giving a spatial as well as a spectral picture of a remote source.

INFRARED HETERODYNE SPECTROSCOPY OF LABORATORY AND REMOTE SOURCES

Michael J. Mumma

Until now, high-resolution infrared detection techniques near 10 μm have been unsuited for studying molecular line profiles in remote low-pressure sources. This inadequacy was a consequence of instrumental resolutions which were much wider than typical Doppler line profiles. Line profile measurements typically require instrumental resolutions on the order of 1 part in 10^6, whereas conventional ground-based instruments (even Fourier spectrometers) typically have resolutions of 1 part in 10^3 to 1 part in 10^4. In addition to having insufficient resolution to see the line profile, conventional systems also suffer from sensitivity degradation because the rather narrow line source contributes signal over only a small part of a resolution interval while noise is collected over the entire resolution interval. These disadvantages can be overcome using the technique of infrared heterodyne spectroscopy. Our group at Goddard has built the first heterodyne spectrometer which uses tunable, semiconductor diode lasers as local oscillators and provides extremely high spectral resolution ($>10^6$) and also high sensitivity detection (NEP $< 10^{-15}$ W/Hz$^{1/2}$) at 8.5 μm.

In this technique, radiation from a remote source is beat against coherent laser radiation from a local oscillator (LO), which is brought very close in frequency to the molecular line we want to detect. The beating process produces a signal at the difference frequencies ($\upsilon_{LO} - \upsilon_s$) which now lie in the radio range of the spectrum. Essentially, the zero of the frequency scale has been shifted to the position of the LO frequency, and the molecular line from the remote source appears in the radio range, where the techniques of RF electronics may be used to determine the line profile and the line intensity. These are the same techniques that have been used so successfully to measure line profiles from interstellar molecules.

The problem of spectral dilution in conventional detection systems is illustrated in figure 1, the laboratory absorption spectrum of ammonia from approximately 1200 cm^{-1} to about 700 cm^{-1}. This vast array of rotational-vibrational lines constitute one particular vibrational band in the ammonia molecule, and each line (in fact these are groups of lines) originates in a transition from one rotational level of the excited vibrational level to a rotational level of the ground vibrational level. One line that we have

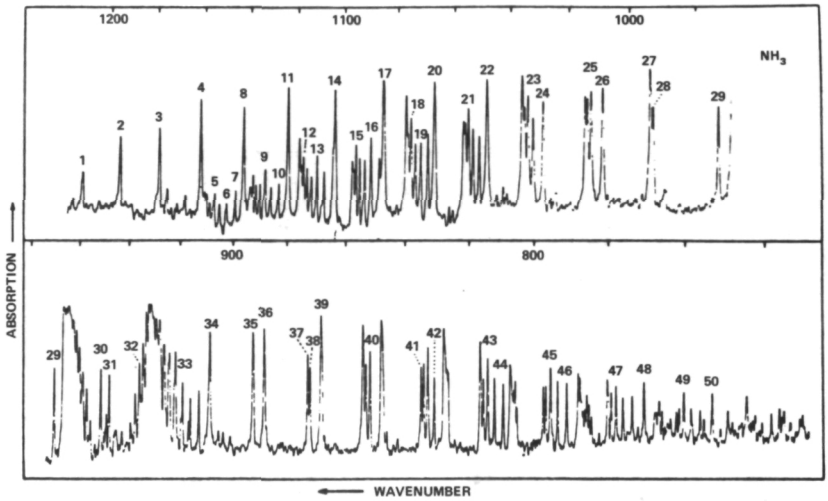

Figure 1. The laboratory absorption spectrum of ammonia.

investigated using our diode laser system is the line labeled 3, which, even at the very highest conventional laboratory resolution (about 0.05 cm^{-1}, shown here), is seen to be a single element. However, when we scan this line with our ultrahigh resolution, diode laser technique, it is found to consist of eight components, as predicted by theory.

The resolution of our heterodyne spectrometer is illustrated in figure 2, which shows the line profiles measured for nitrous oxide (N_2O). Here you see one of the N_2O absorption lines near 8.5 μm depicted as a function of wavelength or frequency. This is a single, fine structure, rotational-vibrational line of a vibrational band as for ammonia in figure 1. The resolutions of the best available Michelson spectrometers at this wavelength are about 0.1 cm^{-1}, whereas the absorption line width is of the order of 0.006 cm^{-1}. This line was already slightly pressure broadened. The best tilting filter instrument, a new technique which has just been developed, has a resolution of about twice the pressure-broadened line width (~0.012 cm^{-1}). We expand this range to show you the line profiles measured by us in the direct and heterodyne modes.

The N_2O line profile was first measured by passing the diode laser radiation directly through the gas cell and tuning it over the absorption line (dashed line). This constitutes an active measurement and requires a local infrared source and a local gas cell. On the other hand, the histogram was measured by passing the radiation from a 1300 K blackbody through the gas cell and then detecting the absorption line in a remote way by beating the blackbody

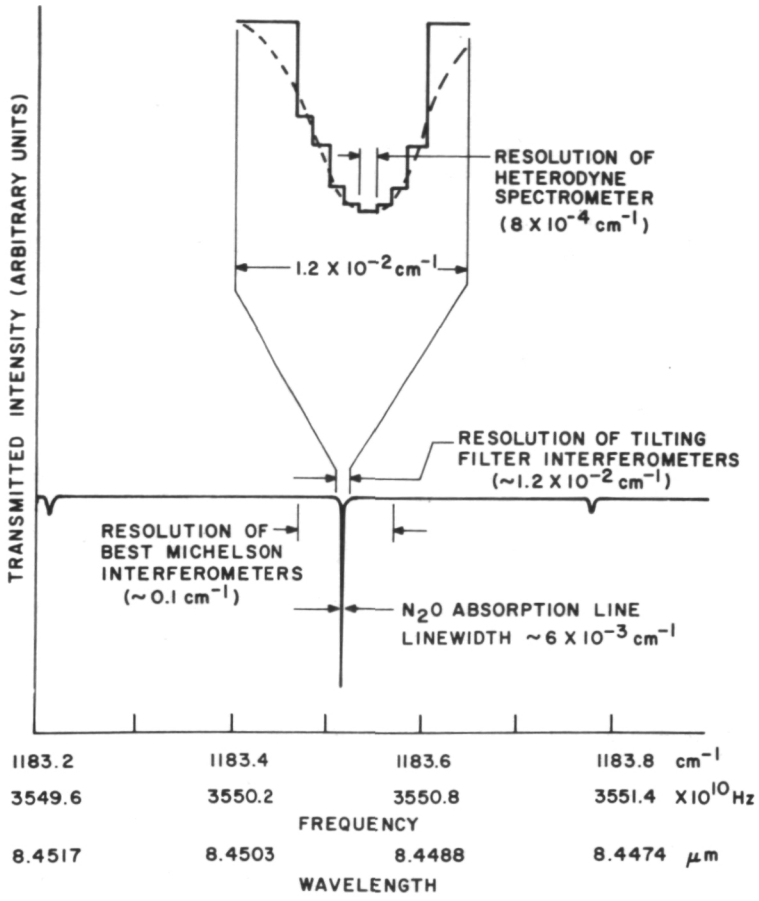

Figure 2. Line profiles for nitrous oxide.

radiation against the local oscillator. The noise is slightly greater on this profile, because the power detected in the heterodyne experiment in each 25-MHz interval is $\sim 10^{-13}$ watts, whereas the power detected in the direct absorption experiment is $\sim 10^{-4}$ watts, or 9 orders of magnitude higher.

The sensitivity of the heterodyne technique is further illustrated in figure 3, which shows the results of measurements of thermal emission from the surface of Mars and from the moon. The 8 channels of our intermediate-frequency filter bank are shown; each was 25 MHz wide, and they were sequentially located in frequency. Thus, our instrument had a frequency bandwidth of approximately 200 MHz centered near 8.5 μm (or 3.5×10^{13} Hz). The

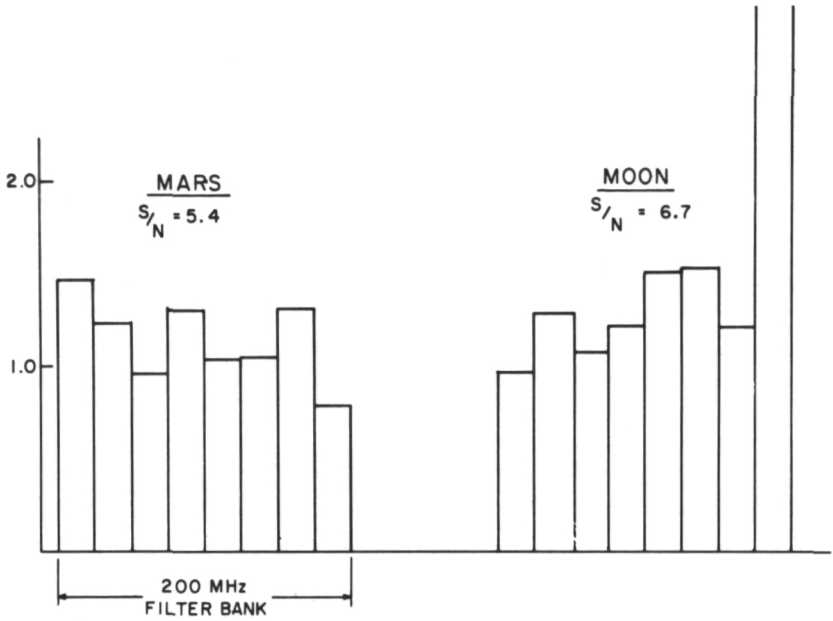

Figure 3. Heterodyne signals at 8.5 μm.

signal in each channel represents a very tiny slice of the blackbody spectrum emitted by this rather cold surface (T ~ 275 K) and yet is observed with a signal-to-noise ratio of 6:1 in 8 minutes of integration. The power in each 25-MHz interval is approximately 10^{-14} watts. This experiment was carried out last winter at the Goddard Optical Site. We are now building a second-generation system which we expect to enable us to measure Doppler-broadened lines from interstellar clouds and the upper atmospheres of planets.

DISCUSSION

ROMAN: This paper and the preceding one describe detection in opposite 'side bands.' How do the techniques compare?

MUMMA: One advantage of using the low frequency side band (heterodyne detection) is that the spectral resolution is inherently much higher. This is because the line is shifted into the radio range where filters are available; therefore, resolutions of the order of 1 part in 10^6 can be achieved easily. The spectral resolution is limited only by the line width and stability of the laser, which set an upper limit on the resolutions in excess of 1 part in 10^8.

The upconversion technique more closely approaches the true quantum noise limit of operation, but it has a poorer spectral resolution. Its resolution is approximately one wave number at a thousand wave numbers, or one part in a thousand.

PIEPER: You said that the two techniques would appear to be complementary?

MUMMA: Yes, they are complementary. For example, we could look at many rotational lines in a vibrational band with the upconverter thus determining the rotational temperature, and we could look at the individual line profiles with the heterodyne receiver and thus measure the kinetic temperatures and Doppler velocities.

VOICE: (Inaudible question.)

MUMMA: The heterodyne approach is actually considerably better than that; we know what the theoretical noise limit is. In our case, it is approximately 20 times lower than the sensitivity we actually achieved this winter. I would like to point out that when we started this project, we did not have diode lasers with sufficient power to heterodyne. No one had ever done this kind of experiment before. We were very pleased to achieve heterodyning within a factor of 20 of the theoretical quantum limit. We think that now, given improvements in the lasers and so forth, which have been achieved, we can get to within a factor of three of the theoretical limit.

BOGGESS: What is the status of semiconductor diode lasers?

MUMMA: We have just returned from a visit to the M.I.T. Lincoln Laboratories where Dr. Melngailis's group is working very hard on building better diode lasers. We are pleased to report that they now have successfully grown lasers which can be tuned over the entire range from 8 to 10 μm with approximately 25-percent coverage of that spectral interval and which put out about 1 mW of power. These diodes will be commercially available in the near future. Using these diodes we would have the ability to build heterodyne systems using a single LO that can cover a 2-μm range. By using different LOs and different detectors, we can, however, cover the entire range from 1 to 30 μm.

RED GIANT STARS: VIBRATIONALLY EXCITED STATES IN SILICON MONOXIDE

David Buhl

This paper is concerned with a discovery that Dr. Lewis Snyder and I made in December 1973, and with the implications it has for infrared astronomy. We have discovered a new molecular maser in the circumstellar shells of variable red giant stars. These stars are rather late in their evolutionary sequence and have burned most of their hydrogen. They are also recycling a lot of their material into the interstellar medium in the form of shells of dust and gas. The molecules in these shells are detected by radio emission from rotational transitions. The newest molecular maser comes from vibrational levels of the silicon monoxide (SiO) molecule.

Figure 1 shows the energy level diagram of the silicon monoxide molecule. For comparison, the energy levels for the H_2O and OH masers are indicated. What are illustrated here are the very small changes in the energy due to changes in the rotation of the molecule while the molecule is simultaneously vibrating. The V quantum number refers to the vibrational action of the atoms while the J quantum number refers to the rotations in this molecule. The rotational energy separations have been exaggerated because the vibrational transitions are at 8 μm, while the rotational transitions are at 7 mm. There is a factor of 10^3 between the changes in energy due to rotation and changes in energy due to vibration.

The interesting point about this discovery is not that we found silicon monoxide; that was known to exist in these stars. What is quite exciting is that there is no sufficient excitation to keep these molecules in a high energy, vibrationally excited state long enough for them to emit a radio photon. Subsequently, Dr. Patrick Thaddeus and the group at the University of Texas detected two other transitions which confirm the identification of the SiO molecule. In addition, we have recently detected very weak emission from the ground state (V=0, J=2-1). Several suggestions have been made attempting to explain the unexpected vibrational excitation of SiO. Nothing satisfactory has yet been proposed.

It is now important to ask if there are similar population inversions at infrared wavelengths, because, obviously, some of the starlight is being converted into infrared and microwave energy. Such lines would be extremely narrow

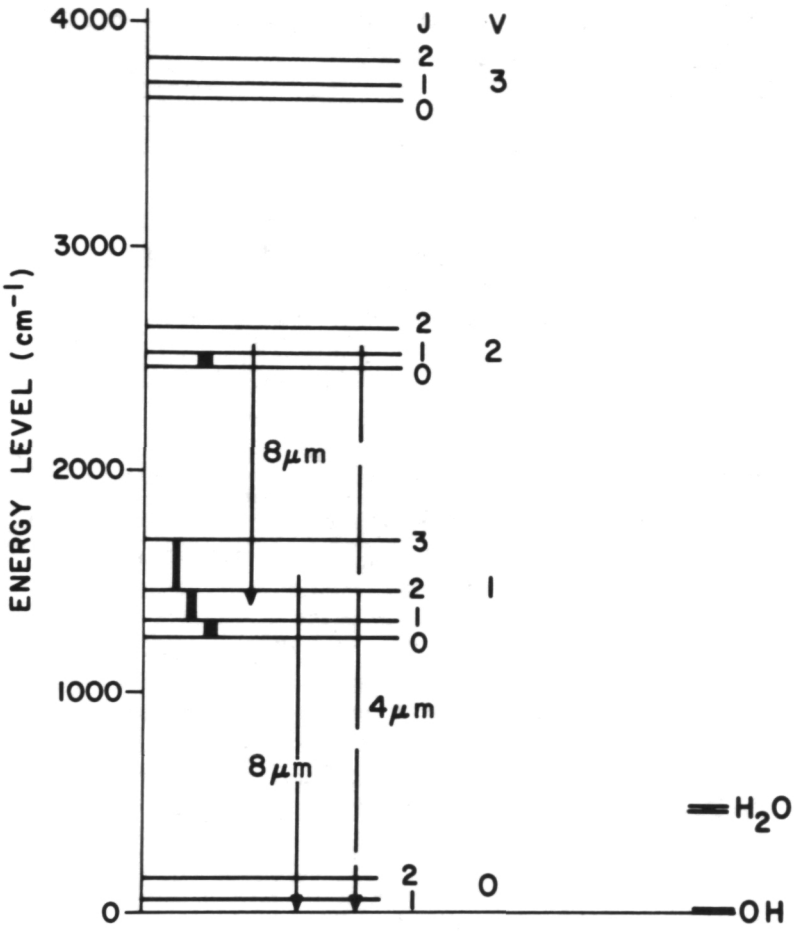

Figure 1. SiO energy level diagram.

as shown in figure 2. These radio lines have a width of about a part in 10^5. Conventional infrared techniques have insufficient resolution to be able to see these lines.

Therefore, we would like to take an infrared spectrometer, such as that discussed by Dr. Mumma in the previous paper, and look at very high resolution at the vibrational transitions of these molecules to determine what excitation processes are going on. There are enormous amounts of energy tied up in the conversion (figure 3), and, in some way, the infrared energy from the star which has a 2000° temperature is pumping up the infrared transitions shown by the vertical lines.

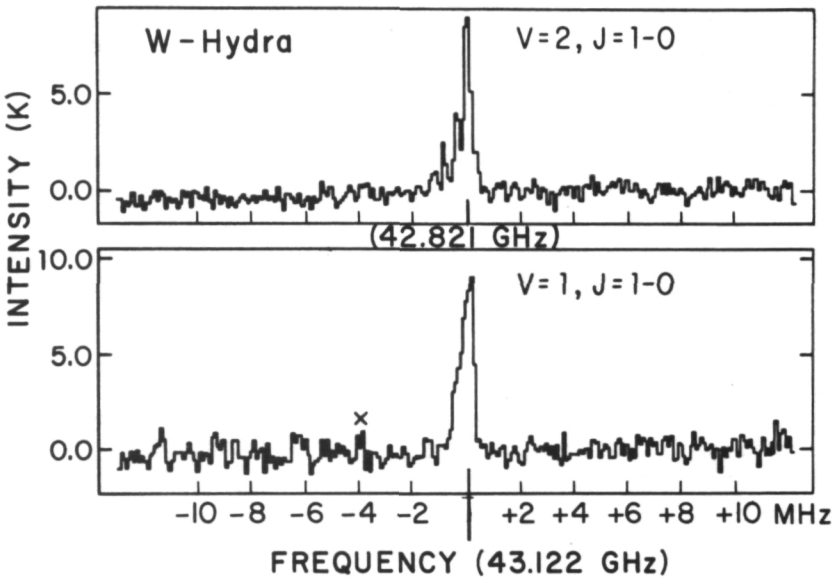

Figure 2. SiO spectrum of the first and second vibrational states in the red giant star W-Hydra.

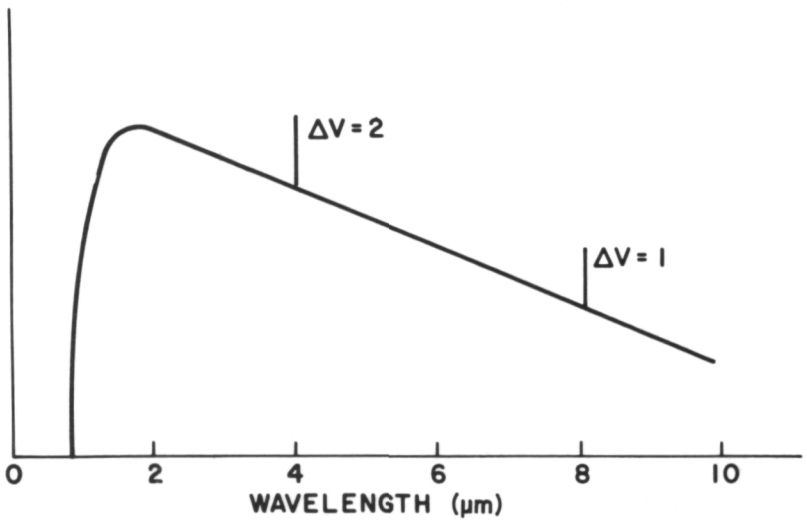

Figure 3. Planck emissions for a red giant star (2000 K).

Hence, there is an energy conversion process occurring where the star is not only losing material but is also losing energy, and some of this energy is converted into radio and infrared signals which we can detect with high resolution spectrometers.

INFRARED RADIATIONS FROM H1 REGIONS IN SPACE

John J. Hillman

I shall discuss some of the results of a model calculation used to determine the infrared surface brightness of a unit interstellar cloud due to rotationally excited molecular hydrogen. The sole excitation mechanism is taken as the Stecker and Williams pumping mechanism, suitably amplified to include rotational quantization of the vibrational levels.

In figure 1 this excitation scheme is explained. It is assumed initially that the molecular hydrogen is in the ground electronic and vibrational state, and a further constraint is that the ortho-to-para ratio be defined simply by statistics as 3:1. The pumping mechanism is allowed to act on these hydrogen molecules. The absorption of an ultraviolet photon from the interstellar radiation field causes the molecule to become electronically excited to the B state. It will be in a discreet vibrational level, denoted as V_i, and in either the rotational level of 0, 1, or 2. This is followed by a dipole-allowed cascade to the ground-electronic state. Approximately 23 percent of these cascades will terminate in the vibrational continuum; that is, they will be lost to disassociation. The remainder will terminate in bound vibrational levels, with the highest probability being centered around the sixth or seventh vibrational level. Finally, these vibrationally excited molecules are allowed to cascade to the ground vibrational level, and, being rotationally constrained by the quadruple selection rule, ($\Delta J = 2$), they will fill up the rotational levels. What one desires from the calculation then, is the final rotational state population, given this excitation mechanism.

In table 1 the results of this type calculation are shown. This table gives the final rotational state population of the ground-electronic and -vibrational level. Note that almost half of the rotationally excited molecules are in the rotational levels of 2, 3, 4, and 5. Also in table 1 are the wavelength of the transition and its notation, S_0 and S_3.

Figure 2 contains the results of the cloud brightness calculation. To estimate the expected intensities of the infrared lines from interstellar clouds, one assumes an average radiation field in an intercloud medium of 3×10^{-8} photons/cm^2/s/Hz over the wavelength region from 912 to 1010 Å. In figure 2, this corresponds to the quiet radiation field. The absorbed flux is about 10^4 photons/cm^2/s/line, where a typical line width of a tenth of an Angstrom was assumed over the optically thick Lyman and Werner bands.

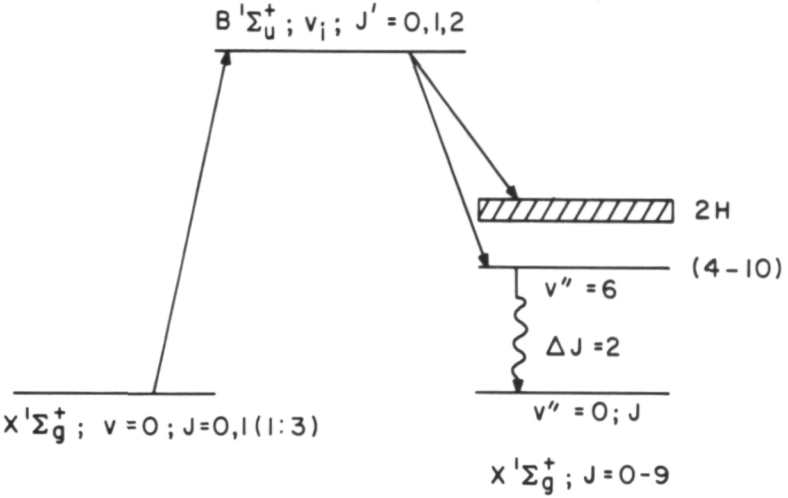

Figure 1. Mechanism of exciting H_2 in dense H1 regions.

Table 1
Final Rotational State Population

J	TRANSITION	PROBABILITY	
0		1.409×10^{-3}	
1		3.842×10^{-2}	
2	$S_0 = 28.1\ \mu m$	2.818×10^{-3}	46%
3	$S_1 = 16.9\ \mu m$	8.071×10^{-2}	
4	$S_2 = 12.1\ \mu m$	3.966×10^{-2}	
5	$S_3 = 9.4\ \mu m$	3.362×10^{-1}	
6		5.995×10^{-3}	
7		1.065×10^{-1}	
8		5.096×10^{-2}	
9		3.373×10^{-1}	

In the ultraviolet molecular hydrogen spectrum, there are about 50 such lines, yielding an expected excitation rate of 5×10^5 excitations/cm^2/s.

From figure 1, recall that approximately 77 percent of these excitations will result in a bound, vibrationally excited hydrogen molecule, of which about half terminate in S_0 to S_3 emission. One therefore obtains a surface brightness of about 2×10^{-15} W/cm^2 into 4π ster in these lines. In the

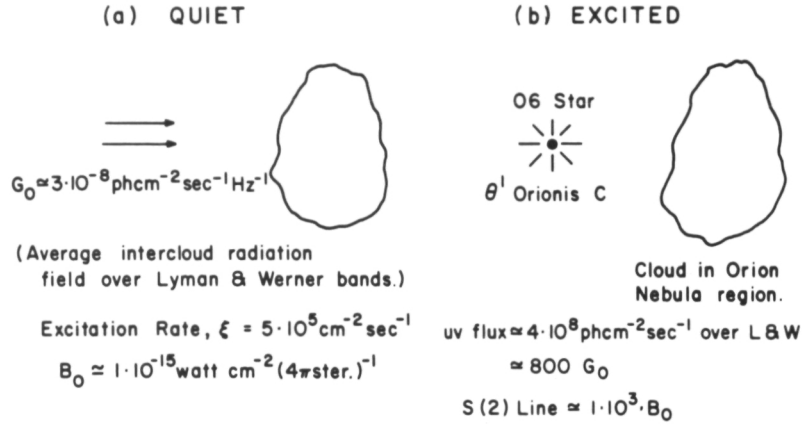

Figure 2. Expected cloud brightness in the infrared.

outskirts of the cloud, rotationally inelastic collisions will reduce the surface brightness to about 1×10^{-15} W/cm^2 into 4π ster. At the present time, this flux is below the detection limit of state-of-the-art infrared interferometers and heterodyne spectrometers.

For the case of a BO star that condenses in a portion of the cloud, or near it, this is depicted as an excited region in figure 2. We will assume that the average distance from the remaining molecules is about one parsec. In this case, the ultraviolet flux incident on these molecules would be at least 100 times greater than the quiet intercloud radiation field. These sources should be detectable with presently proposed instrumentation, using reasonable integrating times.

An example of such a nonequilibrium area can be found in the Orion Nebula region, which is approximately what I have depicted in (b) of figure 2. The exciting radiation comes from the 06 star, θ^1 Orionis C. The ultraviolet flux is calculated to be a factor of 800 higher than the quoted intercloud radiation field.

In conclusion, this expected intensity would be observable with a signal-to-noise ratio of 1 by an ideal heterodyne system with a 100-MHz bandwidth and 100 seconds integrating time.

DISCUSSION

PIEPER: That is an observation that we eventually hope to make.

HILLMAN: Yes, it is.

MARAN: I have two questions. First, what was the assumed column density, and how much of this radiation would come out at 28 μm?

HILLMAN: The column density was assumed to be approximately 10^{17} to 10^{18} hydrogen molecules per square centimeter, which resulted in the 0.1-Å line width that we assumed.

For how much of this radiation comes out at 28 μm, see table 1. Over the S_0 to S_3 transition, that is the four lines, about half of the total brightness will be in these four lines.

Actually, the calculation is being refined, in order to establish some relatively meaningful numbers in terms of percentages at the various wavelengths. It looks like the shorter wavelengths will be a more likely prospect for observation, around 9 μm.

NEW THEORY OF THE EXCITATION OF INTERSTELLAR GAS

Minas Kafatos*

In the last few years, much information has become available for the density, temperature, and ionization structure in the interstellar medium. This is accomplished by widely different measurements in different fields of astronomy.

In table 1, various quantities averaged over pathlengths of observation are shown along with the techniques used to deduce them. The neutral hydrogen number density is referred to by n_H; n_e refers to the electron number density; and T refers to the temperature of the gas.

The satellites OAO-2 and OAO-3 provide information for n_H, as do the recent, important measurements by the "Copernicus" (OAO-3) satellite, on the higher ionization stages of heavy elements (such as carbon, nitrogen, and oxygen).

The ionization rate ξ is not determined directly; it is only determined indirectly by combination of the other measurements.

In table 2, typical values of the observed quantities are shown. The observations give evidence for a two-component medium: one, which is called the cloud medium or cold component, with a mean temperature of around 70 K, and a hot component, of intercloud medium, with a lower limit of 600 K. Notice also that NIII and CIII, from the intercloud medium observed by Copernicus, are very low. This will be important in our discussion.

Theories of excitation of the interstellar gas can be classified as steady state or time dependent. In the steady-state theory, the assumption is made that the average time interval between exposures of the gas to heating and ionization is short compared to the characteristic time scale for the gas to cool or recombine. This, of course, is a particular case of a more generalized time-dependent theory which allows the opposite to be true. In the steady-state theory, a unique relation exists between the temperature and the degree of ionization.

*NRC Resident Research Associate at GSFC.

Table 1
Observational Input to Theory

Quantity	Observation	Technique			
		UV Spectroscopy			
		OAO-2	OAO-3 "Copernicus"	Radio Telescope	Optical Telescope
$\langle n_H \rangle$	21-cm Emission			X	
$\langle n_H \rangle$	L_γ-α Absorption	X	X		
$\langle n_e \rangle$	Pulsar Dispersion Measure			X	
Ionic Abundances of C, N, etc.	Interstellar UV Absorption Lines		XXX		
$\langle n_H/T \rangle$	21-cm Absorption			X	
$\langle n_e^2/T^{1/2} \rangle$	Diffuse H_γ, H_β Emission				X
$\langle n_e^2/T^{3/2} \rangle$	Low-Frequency Absorption			X	
$\langle n_e^2/T^{3/2} \rangle$	Radio-Recombination Lines			X	
ζ	By Combination of Above				

Any theory of the interstellar gas must first identify the source of excitation; second, identify the heating and ionizing agent; and third, identify the excitation as steady state or time dependent.

The physics can be solved independently of knowing the source of excitation. A theory can give answers, but, if it is not tied to reality, it is not a good theory. The steady-state theory of interstellar medium excitation as proposed in 1969 by Field, Goldsmith, and Habing enjoyed wide recognition due to its initial successes and theoretical simplicity. However, as more observations became available, the theory became untenable. Among the objections to the steady-state model are the low abundances of higher ionization stages that I mentioned before were observed by Copernicus. The model is also objected to because all plausible sources of excitation are time dependent rather than steady state and because density contrasts of 100:1 between clouds and the intercloud medium predicted by it are not usually found. (On the average, a contrast of only 2:1 is observed.) For these reasons, the steady-state theory is considered to be untenable.

Drs. Gerola and McCray of the University of Colorado and I formulated the time-dependent theory of the interstellar gas. We took a constant, low

Table 2
Typical Values of Observed and Time-Dependent Theory Quantities

Observations	Time-dependent Theory*
$\langle n_H \rangle \approx 0.35$ cm^{-3}	$\langle n_H \rangle = 0.3$ cm^{-3}
$T_{CL} \approx 70$ K	$T_{COLD} = 58$ K
$T_{IC} > 600$ K; $T_{IC} \approx 5300$ K	$T_{HOT} = 2000$ K
$\langle n_e \rangle \approx 0.025$ cm^{-3}	$\langle n_e \rangle = 0.012$ cm^{-3}
$10^{-8} \lesssim \left\langle \frac{n_e^2}{T^{3/2}} \right\rangle \lesssim 10^{-5}$ cm^{-6} K$^{-3/2}$	$\left\langle \frac{n_e^2}{T^{3/2}} \right\rangle = 4.3 \times 10^{-7}$ cm^{-6} K$^{-3/2}$
$2 \times 10^{-5} \lesssim \left\langle \frac{n_e^2}{T^{1/2}} \right\rangle \lesssim 2 \times 10^{-4}$ cm^{-6} K$^{-1/2}$	$\left\langle \frac{n_e^2}{T^{1/2}} \right\rangle = 2.7 \times 10^{-5}$ cm^{-6} K$^{-1/2}$
$10^{-15} \lesssim \zeta \lesssim 10^{-13}$ s^{-1}	$\zeta = 7 \times 10^{-15}$ s^{-1}
$\langle$N III/N$\rangle < 10^{-4}$	$\langle$N III/N$\rangle = 10^{-6}$
$\langle$C I/C$\rangle \approx 10^{-3}$	$\langle$C I/C$\rangle = 1.3 \times 10^{-3}$
$\langle$C III/C$\rangle \approx 5 \times 10^{-5}$	$\langle$C III/C$\rangle = 4 \times 10^{-5}$

*Source: Supernova bursts once every 30 years; heating and ionizing agent: 150 eV X-rays; total energy in bursts: 7×10^{50} erg.

density medium with a mean density around 0.3 cm^{-3}, exposed to soft X-ray supernova bursts that occur randomly in space and time. The structure of the gas was calculated by computing the time record of temperature and ionization at a given point by a Monte Carlo simulation. The calculation yields probability distributions for the temperature and the ionized fraction, and their observable combinations.

With the first version of the theory, which is admittedly simple because of its assumption of constant density, we were able to account for the observations concerning the galactic-disk. Notice this also true of the observations of Copernicus.

In figure 1, the probability distribution of the temperature versus the ionized fraction is shown. Notice that in contrast to the steady-state theory, which is shown by the heavy curve, our theory does not predict a 1:1 relationship between T and the degree of ionization. Notice also that there are two regions in this two-dimensional diagram, one which would correspond to a hot component, or the intercloud medium, and another one which would correspond to the clouds. As I mentioned before, this is a constant-density medium. Therefore, a constant-density medium appears as a two-component medium in this theory.

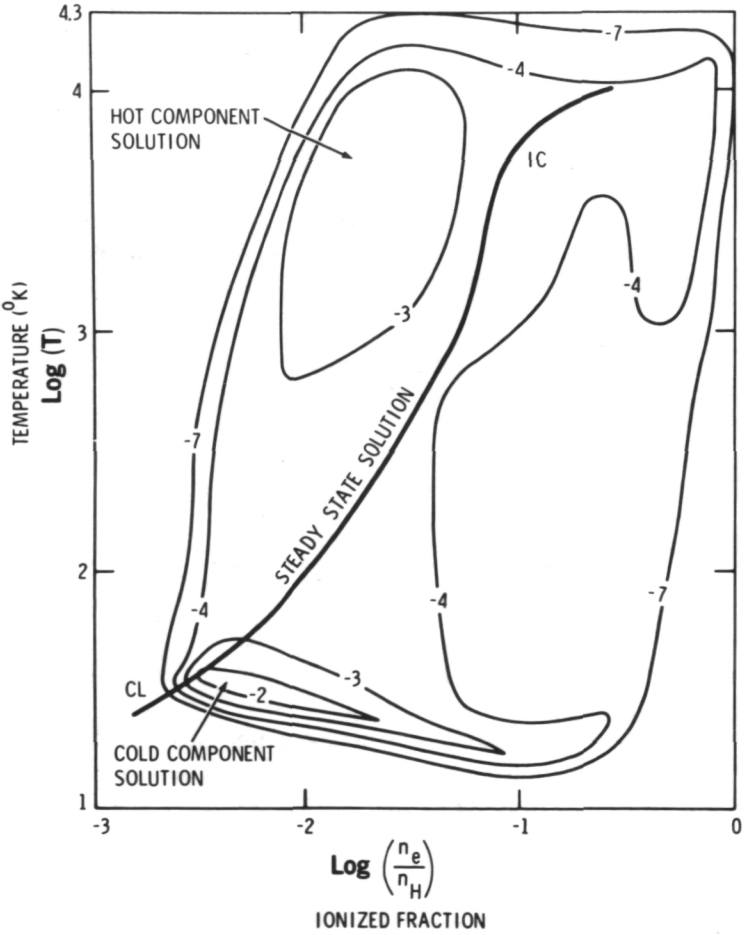

Figure 1. Theoretical probability contours in the temperature-ionization plane for the time-dependent theory.

Regions of low T, but still significant ionization, are expected to occur with an appreciable probability in our theory, about 5 percent. They are completely forbidden in steady state. We were able to account for the Copernicus observations in the direction of λ Sco by assuming that the medium between the sun and that star is in such state.

Recently, Cowan and Rose of the University of Maryland and I have extended the original theory. We found that all plausible sources of ionization and heating are time dependent, and this includes O and B stars, hot XUV stars, and assumed bursts from supernova.

We examined the role played by the galactic distribution of these sources in determining the physical state of the gas in the spiral arms and in the interarm regions of our galaxy. We calculated that the electron densities must be about equal in the arms and the interarm regions, while the rest of the quantities are higher in the arms. Higher densities in-going in the inner arms caused the enhanced free-free radio absorption, radio combination line radiation, and diffuse Hα emission seen towards the galactic center. O and B stars can account for the pulsar dispersion measures and Hβ emission within a kiloparsec of the sun, but the postulated supernova bursts are needed in the denser inner arms. Finally, hot XUV stars are the most likely source of excitation in the interarm regions.

In conclusion, the addition of another dimension, namely, time, to the theory of excitation of the interstellar gas provides much better agreement with the observations.

DISCUSSION

VOICE: How is your theory related to the dust distribution in the galactic disk?

KAFATOS: This theory does not really refer to the dust or molecule distribution, only the neutral hydrogen and ionized hydrogen. Admittedly, it has to be extended later. As you realize, there are many problems in the interstellar medium, and it is hard to do all of them at once. And, as I emphasized, the original statistical theory was able to account for most of the observations in the galactic disk, simply with a constant-density medium. Of course, we know that this is not the case, that there are density variations.

The next thing we did was to take the spiral arms into account, and we got a better agreement.

Other considerations, such as the variation of the gas density with height, would have to come later, as well as dust.

COPERNICUS OBSERVATIONS OF THE INTERSTELLAR ABSORPTION AT LYMAN ALPHA

Ralph C. Bohlin

The column densities of neutral hydrogen toward early-type stars can be directly determined from the interstellar absorption line at Lyman Alpha. The measurements of the gas at 21 cm and at Lyman Alpha complement each other, because the Lyman Alpha data extend to only about 1 kpc while the 21-cm emission measures are ambiguous for this nearby gas.

With a 0.2-Å resolution, the Orbiting Astronomical Observatory-3 (OAO-3) Copernicus satellite reveals significantly smaller values for the gas density than were deduced from the OAO-2 Lyman Alpha data at 12-Å resolution. For 27 stars that have negligible amounts of molecular hydrogen, the Copernicus value for the gas-to-dust ratio is in agreement with the ratio of the mean 21-cm density to the mean reddening of interstellar dust. The OAO-2 result was some 70 percent higher.

For 11 stars behind dense interstellar clouds, where at least 5 percent of the gas is molecular hydrogen, the gas-to-dust ratio varies from 1 to 3 times the mean obtained outside of clouds. In order to better understand the physical conditions in clouds when a large fraction of the gas is molecular, a survey is in progress to observe a larger sample of fainter and more reddened stars.

Figure 1 shows a comparison of the 21-cm radio data with the Lyman Alpha data. The dashed line is the line of equality, where the two measures of the column density would be equal. We see in almost all cases that the 21-cm density lies above that measured by the Lyman Alpha line. This is because the 21-cm emission measures extend to infinity and most of the gas often lies behind the stars, as is particularly true in the region of Orion. This is somewhat surprising, because this group of stars lies about 140 pc below the galactic plane. An interesting point on the slide is δ Sco, where we have a larger Lyman Alpha column density than from 21 cm. This suggests that there is either a very small cloud, smaller than a 21-arc-min radio beam centered on δ Sco, or else the 21-cm emission measures are becoming saturated.

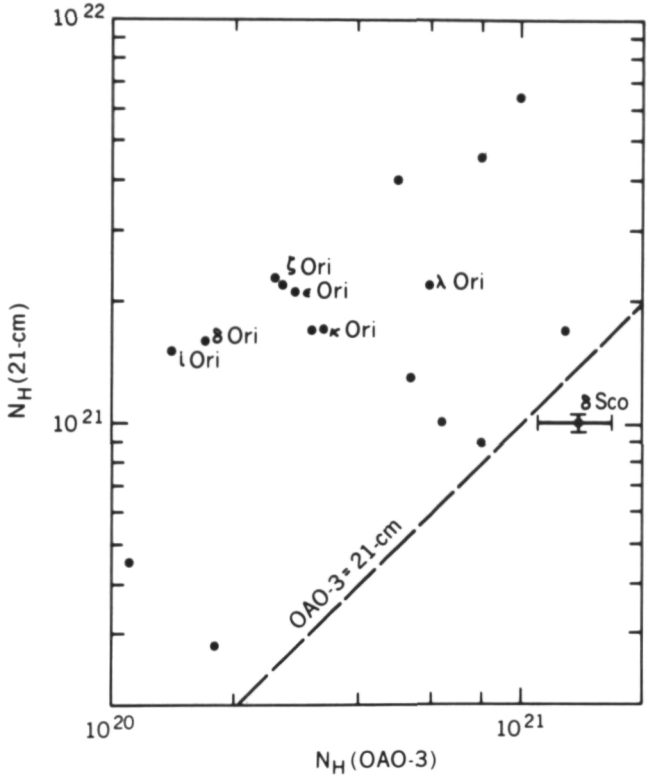

Figure 1. Comparison of 21-cm radio data with the Lyman Alpha data.

Figure 2 shows the general correlation between the gas measured by the column density and the dust measured in magnitudes of color excess. The dashed line is the mean gas-to-dust ratio defined by the filled circles, the 27 stars with negligible amounts of molecular hydrogen. The open circles are those stars that have a lot of molecular hydrogen, at least 5 percent in the line of sight. The lower open circle is the amount of atomic hydrogen, and the upper open circle connected by the bar is the total hydrogen found by adding on the molecular hydrogen. In a few cases, the atomic gas is below average and adding in the molecular hydrogen brings the total near the mean line. In many more cases, however, the amount of gas in the atomic form is greater than expected and, when we add in the molecular hydrogen, it becomes even larger. In all cases, when the molecular hydrogen is included, 1 to 3 times the mean amount of gas expected is present in the molecular cloud.

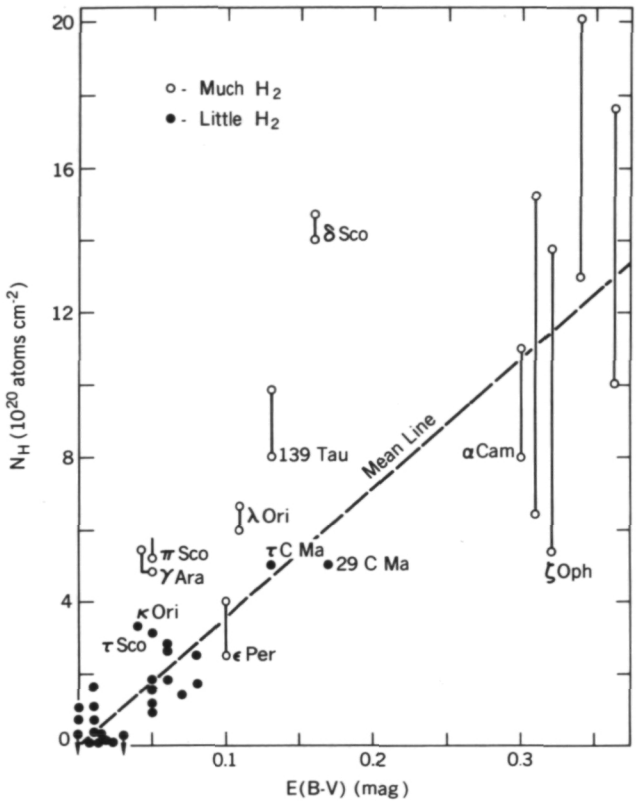

Figure 2. Correlation between gas measured by column density and dust measured in magnitudes of color excess.

Figure 3 shows an attempt to divide the stars based on the dust density and the Lyman Alpha measurements. We see in all cases observed so far that the black dots, those stars with little hydrogen, have a dust density less than 0.3 or a cloud density less than 2.4×10^{20}.

The best indicator of molecular hydrogen seems to be the atomic hydrogen, with only the lower open circle for ϵ Per below the horizontal dashed line. Future observations will test whether this picture is true in general.

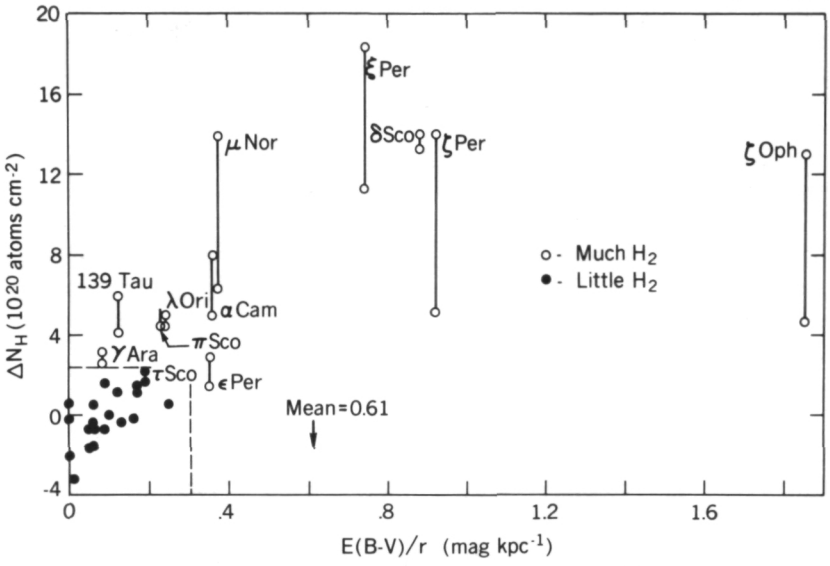

Figure 3. Division of stars based on dust density and Lyman Alpha measurements.

THE ABUNDANCE OF INTERSTELLAR BORON

Andrew M. Smith

I would like to address my remarks to a small part of the material covered by Dr. Kafatos, namely, the subject of the heating of the interstellar gas. As he has indicated, in the steady-state picture of the interstellar medium, it is assumed that the various gas phases are in near-hydrostatic equilibrium, in ionization equilibrium, and that the heating rates equal the cooling rates in each phase.

While we think we know something about the cooling mechanisms, there has been considerable speculation about the sources of heat. One of these which has been discussed over the past decade is low energy cosmic rays. The idea is that the cosmic rays will ionize the atoms of the interstellar medium and part of the energy of the liberated electrons will go into heating the gas. The energy range in consideration is less than 30 MeV per nucleon, and obviously there are great difficulties in measuring the primary cosmic rays in this energy range because of the shielding effect of the solar magnetic field. So we have to resort to some more indirect method.

It happens that cosmic rays will engage in nuclear spallation reactions with residual interstellar gas nuclei in which the light elements are produced, one of these being boron. Furthermore, the predominant ion state of boron, which is singly ionized boron in the interstellar medium, has a very strong resonance transition in the vacuum UV which should be observed in absorption against the background of a hot star.

Ted Stecher and myself at Goddard and Dr. Morton at Princeton University have used the Copernicus (OAO-3) instrumentation to look for this line in the spectrum of ζ Ophiuchi. We did not observe it, but we were able to establish a good upper limit. The results are given below.

Boron Abundance

Source	B/H (10^{-10})
Sun	< 6.3
Achondrites, ordinary chondrites, and enstatites	(1.1 to 24)

Source	B/H (10^{-10})
Carbonaceous chondrites	(38 to 59)
Carbonaceous chondrites, corrected	110
Interstellar medium	<0.75

As shown in the bottom row, our measured boron abundance, expressed in terms of the hydrogen abundance, is less than 0.75×10^{-10}. Boron has not been observed in the solar atmosphere either. A good upper limit on the relative solar boron abundance is 6.3×10^{-10}. In the meteorites, boron has been observed, and I have grouped together several types in the second row which give abundances at the lower end of the scale. The ordinary chondrites give the lowest measured abundances of boron, but they are rather erratic, varying with the sample. By contrast, the carbonaceous chondrites give a larger relative abundance of boron, and the variation with the sample is not quite as bad. For this reason, it has been assumed that the carbonaceous chondritic abundances are more valid.

There are some workers who feel that even the carbonaceous chondrite abundances for boron should be increased, and their corrected value is 110. Recently, Dr. Leckrone of Goddard and some fellow workers in Europe positively identified the same line in the atmosphere of Vega, and they estimate an abundance of 2×10^{-10}, which falls toward the lower end of the relative abundance scale and is closer to the upper limits for the sun and for the interstellar medium. Assuming that our upper limit is valid, we can use it to estimate the primary proton flux in the low energy range which is necessary to produce the boron. This is shown in the listing below.

Derived Quantities

Cosmic-ray proton flux $5 < E < 30$ MeV/nucleon	< 5 cm^{-2} s^{-1}
Hydrogen ionization rate, ζ_H $5 < E < 30$ MeV/nucleon	$< 6 \times 10^{-17}$ s^{-1}
ζ_H, all cosmic-ray energies	$< 8 \times 10^{-17}$ s^{-1}
Required ζ_H for steady-state pressure equilibrium in interstellar medium	$> 10^{-15}$ s^{-1}

Here we have to use the measured spallation cross sections, and we have to make a correction for the loss of the reaction products from the galaxy and for the loss due to subsequent nuclear reactions. We assume that this boron production has been going on over a period of 1.2×10^{10} years and that less than half of the boron produced in this time is consumed in stars.

With all these provisos, we come up with the cosmic-ray proton flux in the 5- to 30-MeV range as being less than 5 cm^{-2} s^{-1}. We can relate this to the hydrogen ionization rate due to protons in the same energy range, ζ_H, which turns out to be less than 6×10^{-17} per second per atom. If we take into account the protons of energy greater than 30 MeV, ζ_H is increased to 8×10^{-17} per second.

However, the steady-state picture requires a ζ_H in excess of 10^{-15} per second, so there is obviously a big discrepancy here. The fact that the boron is very likely depleted by something like a factor of 3 in the interstellar medium will not help us significantly in reducing the discrepancy. This result, considered together with results of other approaches, implies that the low energy cosmic rays are really not an important source of heating in a general sense.

DISCUSSION

RASOOL: What is the measured flux of low energy cosmic-ray protons?

PIEPER: The flux in interplanetary space is about 3 cm^{-1} s^{-1}. That is about the best measured number that I know of, and he found a number like 5 cm^{-1} s^{-1} so it is very close.

MOLECULAR HYDROGEN IN THE GALAXY AND GALACTIC GAMMA RAYS

Floyd W. Stecker

Molecular hydrogen is an important component of the interstellar medium because it is the most stable form of hydrogen at low temperature. It is the predominant form of hydrogen in cool clouds of sufficient density.

However, it is difficult to obtain the galactic distribution of molecular hydrogen directly. Molecular hydrogen has been seen in the ultraviolet observations of Copernicus (OAO-3) in absorption, by studying reddened nearby stars, as was discussed by Dr. Bohlin. But, in the ultraviolet we cannot see beyond 1 kpc because of the high extinction of ultraviolet radiation by interstellar dust.

Rotational-vibrational features in the infrared are inherently weak because they are quadrapole features; that is, because the hydrogen molecule does not have a permanent dipole moment. As mentioned by Dr. Hillman, these infrared features have not yet been detected.

I will discuss here the implications for studies of the molecular hydrogen distribution which can be obtained from recent galactic surveys of both 100-MeV gamma radiation from SAS-2 and 2.6-mm carbon monoxide emission observed by Scoville and Solomon.

The 100-MeV gamma radiation is a product of the interaction between cosmic rays and all interstellar gas nucleons. It is therefore proportional to the column density of interstellar gas along the line of sight of the detector.

Figure 1 shows a comparison of the SAS-2 measurements of the galactic longitude distribution of gamma-ray emission with the fluxes that are expected from the atomic hydrogen as seen in 21-cm radio surveys, interacting with a nominal cosmic-ray flux. By that I mean a cosmic-ray flux with the magnitude observed in the solar vicinity of the galaxy. As can be seen, there is fairly good agreement in directions away from the galactic center. However, if we look within 30° of the galactic center, the agreement is bad by roughly an order of magnitude. Therefore, a predicted gamma-ray distribution based on 21-cm surveys alone would be both too flat and predict much too small a flux in the region of the galactic center.

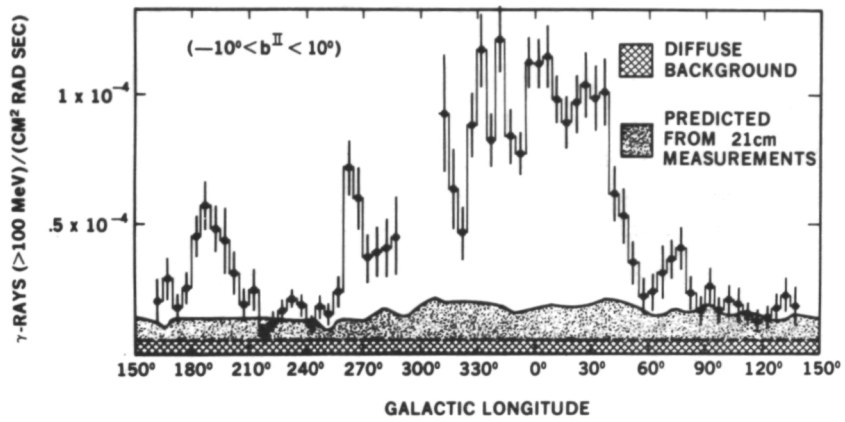

Figure 1. SAS-2 measurements of gamma-ray emission with the fluxes expected from atomic hydrogen based on 21-cm radio surveys.

In figure 2 the SAS-2 longitude distribution of gamma rays as shown by the vertical lines is compared with that calculated using the carbon monoxide distribution of molecular hydrogen clouds observed between 0° and 90° galactic longitude as well as the 21-cm atomic hydrogen distribution. The calculations have been integrated over ±10° in latitude and averaged over 5° in longitude to compare them with the SAS-2 observations. They also include smaller gamma-ray fluxes from Compton interactions and bremsstrahlung important at small longitudes and a relatively small cosmic-ray enhancement in the inner galaxy.

As one can see, there is excellent agreement between the calculations and the observed distribution.

Carbon monoxide emission is believed to be proportional to the molecular hydrogen density because the molecular hydrogen collisionally excites the carbon monoxide in cool, dense clouds. Estimates of the column density of molecular hydrogen can only be made to within a factor of 5, based on the CO emissions survey. But estimates in the galactic-center direction, from infrared and X-ray absorption, indicate that there is enough molecular hydrogen to account for a significant fraction, if not all, of the gamma rays observed in the inner galaxy.

Also, the CO and gamma-ray measurements give evidence for a molecular arm or ring at 5 kpc, corresponding to a galactic longitude of 30°, with a volume averaged density of between 1 and 5 molecules per cubic centimeter.

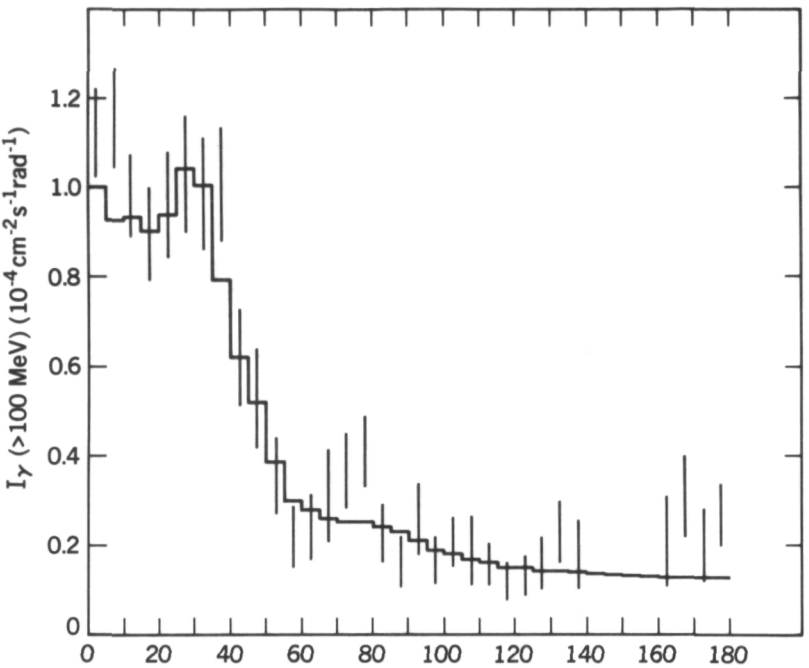

Figure 2. SAS-2 gamma-ray measurements compared with those calculated using carbon monoxide distribution and 21-cm atomic hydrogen distribution.

The lower limit is obtained here from the CO measurements, and the upper limit is obtained from the gamma-ray flux measurements.

These observations support a suggestion made by Ted Stecher and me approximately five years ago—that molecular hydrogen could be an important key in understanding galactic gamma-ray emission.

However, more importantly, they allow us to study an important component of the interstellar medium which is invisible in 21-cm surveys, and which can add to our understanding of galactic structure.

A GAMMA-RAY VIEW OF THE STRUCTURE OF THE GALAXY

Giovanni F. Bignami

The recent data obtained by the SAS-2 satellite on the high energy gamma-ray emission from our galaxy are shown in figure 1. The flux of photons (>100 MeV) is plotted against galactic longitude, summed between ±10° in b^{II}. In the context of a general discussion of the data, the two sharp peaks at 180° and 270° will not be considered, as they are due to localized sources in the Crab and Vela region.

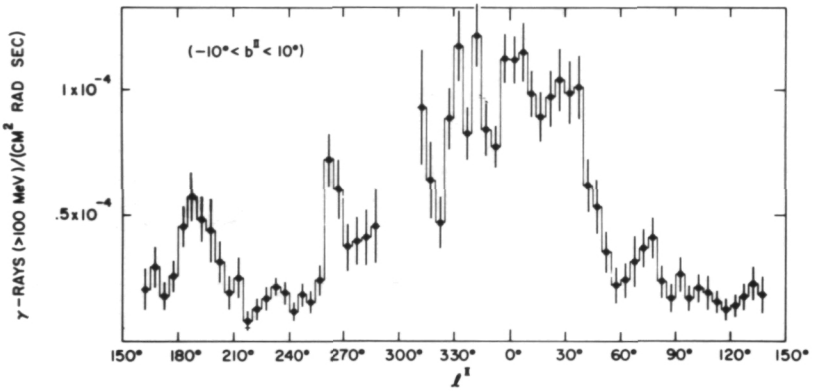

Figure 1. Longitude distribution of (>100 MeV) high energy galactic gamma-ray emission observed by SAS-2.

It is natural to try to interpret the gamma-ray data in terms of interactions of cosmic rays and interstellar matter, and the energy spectrum of the galactic radiation is compatible with at least a strong component coming from the decay of π°-mesons. The first step is to construct a model of the spatial distribution of the total interstellar gas, against which an assumed cosmic-ray distribution will interact.

The interstellar gas is known to consist mostly of hydrogen in its various physical states: neutral atomic, ionized atomic, and molecular. Of these three components, the H1 has been mapped in best detail, because of its line emission at 21 cm, both in terms of spatial distribution proper and absolute density.

Figure 2 shows a schematic map of the spiral structure of our galaxy obtained from 21-cm radio measurements smoothed with the help of the density-wave theory. Although only the "ridges" or the density maxima of the arms are shown, a width of 1 kpc has been given to each arm in the calculation. Furthermore, the general assumption is made that all the interstellar gas is modulated by the gravity wave spiral pattern, so that the H2 component is assumed to have density maxima and minima in agreement with the H1 distribution. The fraction of hydrogen in molecular form is taken to be roughly constant within the solar circle and equal to 50 percent of the total; it is taken to decrease to 30 percent outside the sun's circle.

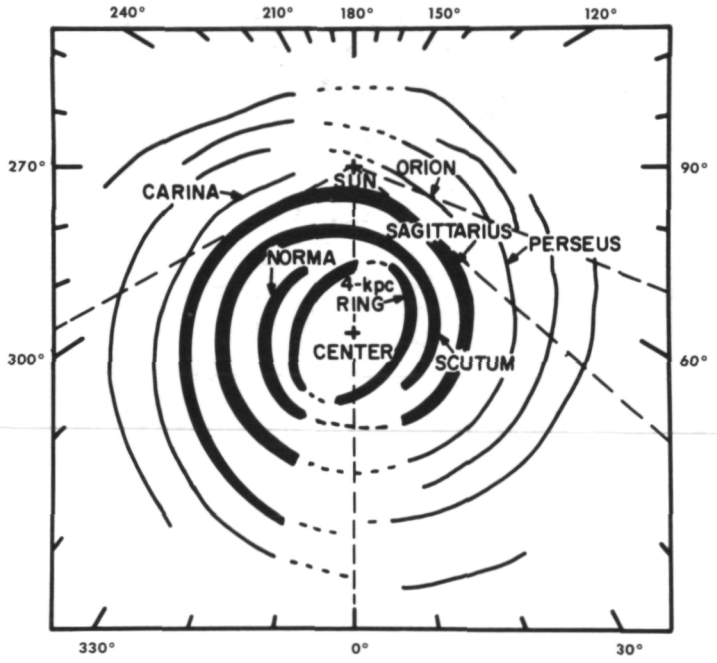

Figure 2. Schematic of the spiral structure of our galaxy obtained from 21-cm radio measurement as interpreted by the density wave theory.

Using classic assumptions on the vertical distribution of the gas, as well as the best available numerical data on the densities, it is then possible to calculate the amount of matter along a given line-of-sight. It is interesting to note that for $b^{II} = l^{II} = 0°$, the calculated column density is equal to 5.3×10^{22} H atoms/cm^2, a number that, because of its good agreement with

other measurements, gives confidence to the density values used in the present model.

Turning now to the cosmic-ray distribution in our galaxy, one must note that for the present problem the important production of gamma rays is due to protons with energies between 1 and 10 GeV. For these particles representing the bulk of the cosmic-ray energy density, it is then possible to invoke the well known argument of confinement by the weight of the interstellar gas. In other words, the balance between cosmic rays, magnetic and turbulence pressures on the one side and the self-gravitational pull on the other, allows one to make the assumption that, on the scale of arm segments, the GeV cosmic-ray density may be taken to be proportional to the gas density. Under these assumptions, the gamma-ray production is proportional to the square of the matter density and thus one can compute the predicted gamma-ray longitude distribution, making use of the individual source function for the π°-decay process. The result is shown in figure 3, together with the experimental data.

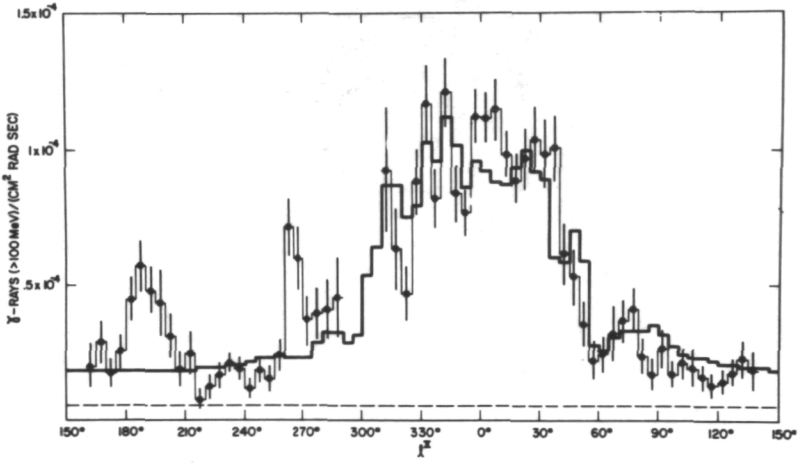

Figure 3. Comparison of model (thick line) and SAS-2 data.

The agreement between the model (thick line) and the data is seen to be good. In particular, the peaks due to the tangential directions of the arms are well reproduced as well as the ratio of center-to-anticenter emission. The small deviations can be due to the inherent imprecision on the assumed gas density distribution as well as to the presence of a component of electromagnetic origin in the very central regions.

The high energy galactic gamma-ray data seem to provide a new tool for the investigation of the large distant features of our galaxy, and that a refinement in the data quality (angular resolution, statistics, energy resolution) will give even better insight into the structure of our galaxy through the study of its high energy phenomena.

GAMMA RAYS FROM SUPERNOVA REMNANTS

David J. Thompson

A supernova is the most energetic phenomena known in our galaxy. Supernovae are generally thought to be responsible for the formation of neutron stars, pulsars, and black holes. They also appear to be the only sources with sufficient energy to keep the galaxy supplied with cosmic rays.

The SAS-2 experiment was designed to study the high energy gamma rays associated with such energetic phenomenon. It is only natural, then, that supernovae and supernova remnants should be subjects of interest in the SAS-2 data.

The two peaks outside the central region and the longitude distribution described in the preceding two papers (Bignami and Stecker) are two supernova remnants. The results I will discuss concern the two supernova remnants which stand out most clearly in the SAS data.

These are the Crab Nebula and the Vela supernova remnant. Although they are similar in many ways, their gamma-ray emission shows a sharp contrast.

The Crab Nebula and its associated pulsar have been observed over most of the electromagnetic spectrum, so it is not surprising that it emits gamma rays as well. The principal result obtained from SAS-2 is shown in figure 1. This figure shows the distribution of gamma-ray arrival time in fractions of a pulse period for the pulsar. The arrows labeled M and S refer to the main and secondary pulse times determined from radio observations.

Clearly, most of the high energy gamma rays are coming from the pulsar. This result is in marked contrast to the X-ray region, where only about 10 percent of the photons appear to be coming from the pulsar. In fact, combining the X-ray data with the SAS-2 data shows a relatively continuous shift from predominantly unpulsed radiation to predominantly pulsed radiation. This striking shift in the fraction of pulsed radiation has important implications for the photon production mechanism. The pulsed and unpulsed production mechanisms must have different energy dependence. Qualitatively, at least, these results are consistent with the model in which the pulsed radiation comes from synchrotron radiation at the speed-of-light cylinder, and the unpulsed radiation comes from regions of smaller magnetic fields.

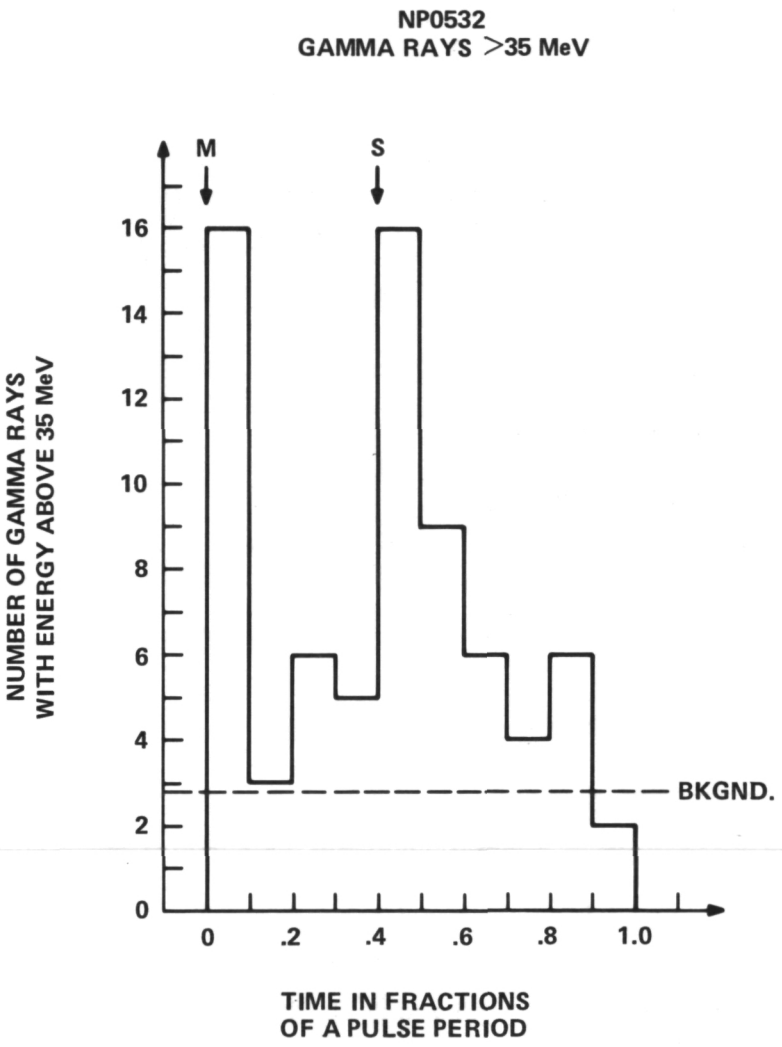

Figure 1. SAS-2 gamma-ray data above 35 MeV for the Crab Nebula (NP0532).

The Vela supernova remnant is closer to the earth than the Crab. Like the Crab, it is a radio source, and, also like the Crab, it contains a pulsar—the third fastest pulsar known. Unlike the Crab, however, it is not a strong X-ray source—only 1 percent as intense as the Crab. It is perhaps a bit surprising, then, that the gamma-ray emission from the Vela region is almost the same as for the Crab and, therefore, lies substantially above an extrapolation of the X-ray data.

We have carried out a time analysis for Vela, similar to the one shown from the Crab, using the Vela radio pulse for reference. No peak stands out, leading us to the conclusion that the pulsar is not primarily responsible for the gamma-ray emission as it is in the case of the Crab.

The energy spectrum seen from Vela is similar to the galactic plane emission which Bignami and Stecker discussed in the previous papers. This is the type of spectrum associated with cosmic rays interacting with matter. This spectrum, coupled with the fact that the gamma-ray flux lies above an X-ray extrapolation, suggests that another mechanism is involved in the gamma-ray production.

The second figure shows the Vela region as photographed in ultraviolet. The supernova remnant shell can be seen in this photograph more clearly on one side than the other, but nevertheless forming a nearly circular shell. If the Vela supernova remnant produced cosmic rays, then this shell is the logical volume of containment for these cosmic rays.

Assuming the cosmic rays are interacting with the local matter, we can then ask, "How much energy in the form of cosmic rays would have been required to produce the gamma-ray flux which SAS-2 observes?" Depending on the specific assumptions made, the result is from 10^{50} to 10^{51} erg emitted in the form of cosmic rays.

One possible set of parameters is shown in the following list.

Vela Supernova Remnant

5×10^{-6} γ-rays (> 100 MeV)/cm^{2}s

460 pc distant

1.5 protons/cm^3

3×10^{50} erg in cosmic rays

This provides a value in the range predicted by theoretical supernova calculations. It is consistent with the energy needed to keep the galaxies supplied with cosmic rays, and it is in agreement with the energy needed for the ionization of the interstellar medium as Dr. Kafatos discussed in his paper. We feel, therefore, that these gamma-ray data may be providing the first direct experimental evidence for the supernova origin of cosmic rays.

In summary, the Crab and Vela supernova remnants show very different results in the gamma-ray data of SAS-2, with the Crab being an extension of the X-ray producing mechanisms to higher energies, primarily pulsed radiation, while the Vela gamma radiation results from interactions of the supernova cosmic rays with the surrounding matter.

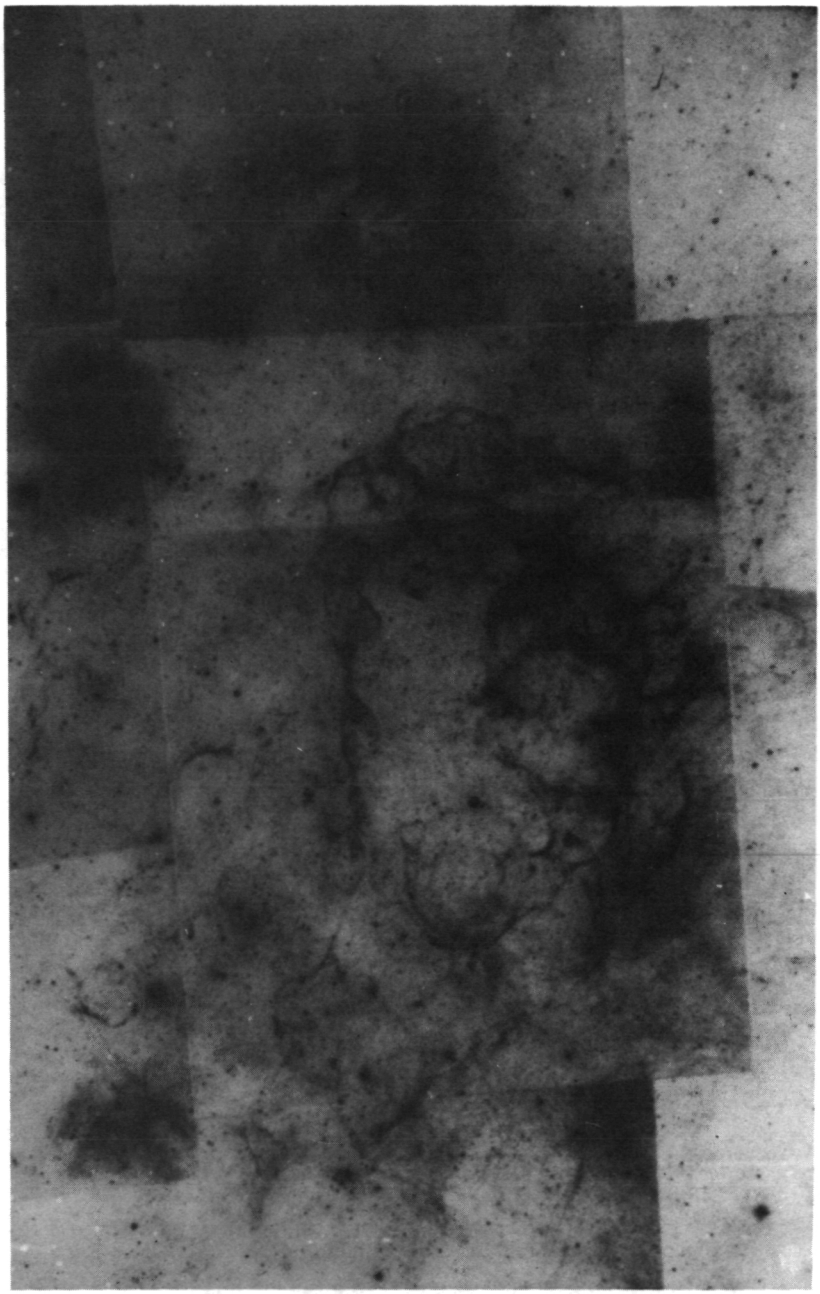

Figure 2. Vela supernova remnant photographed in the ultraviolet.

DISCUSSION

VOICE: Are you saying that the Vela supernova was responsible for our local cosmic rays?

THOMPSON: No. If you assume that we have one supernova every 30 to 100 years then it takes this much energy to keep up the flux of cosmic rays.

VOICE: How large is the gamma-ray source you observe? Is it a point source?

THOMPSON: We cannot resolve with SAS-2, anything smaller than about a 5° circle, which is about the size of the supernova shell. We know that the gamma rays are coming from this region, and therefore, we interpret the high-energy cosmic rays as being contained within this region.

We should point out at this point that future gamma-ray experiments with better angular resolution should be able to pinpoint exactly where in this region the gamma rays are coming from. But at the present time, all we can say is, it is approximately the size of that supernova shell.

VOICE: Can you explain why you do not observe a pulsed emission, if Vela is similar in other ways to the Crab?

THOMPSON: The Vela supernova remnant is much older than the Crab, and, although it is observed in the radio as a pulsar, it may or may not even be observed as an X-ray pulsar–very marginal. It appears that whatever mechanism is involved in producing the pulse, it falls off very rapidly with energy, in the case of Vela. We know in the case of the Crab Nebula, that the pulse mechanism has a rather flat spectrum.

So exactly what mechanism it is, I cannot be sure. I should mention, though, that there is the question of why, if the Crab was a supernova, it does not produce the same sort of flux that we see from Vela. The answer is that the Crab is about four times farther away; therefore, the same type gamma-ray production that we see from Vela would not be observed.

VOICE: Could you comment on the observations of pulses from Vela at lower gamma-ray energies?

THOMPSON: In the gamma-ray region, there are only two measurements so far of pulsed gamma rays, or attempts to measure pulsed gamma rays. One is by the Case Western Reserve group, which was dealing with a somewhat lower energy range.

X-rays, hard X-rays, are extremely contradictory. I do not know why. It is possible that it is turning on and off. If it is, I should mention that we do have another exposure to the Vela supernova that we have not analyzed, and we are going to try to do a timing analysis on that, too. Perhaps, if it is turning on, we will see it in the second exposure, where we definitely did not see it in the first. It's possible.

UK-5 OBSERVATIONS OF X-RAY SOURCES

Stephen S. Holt

UK-5 (Ariel-5) is the latest in a series of joint U.S.-U.K. cooperative satellite programs in which NASA generally provides the vehicle and technological support for an essentially British scientific payload. Goddard has an experiment on this spacecraft, which I shall discuss.

Figure 1 is an artist's conception of UK-5, which has been operational for about a month. It is spin stabilized in a low altitude, equatorial orbit, and it is entirely devoted to the study of X-ray astronomy. There are six separate experiments on board, four of which point out along the spin axis, and the other two, including GSFC's, are used in a scanning mode.

Our experiment is an X-ray pinhole camera, and we image the X-ray sky through two 1-cm^2 pinholes onto position-sensitive proportional counters. The whole experiment has a fan-beam field of view, about 4° wide, from spacecraft pole to antipole. There are some blind spots right at the poles and at the equator. The fan beam is rotated by spacecraft rotation for viewing the entire X-ray sky, or most of it, every rotation. Unfortunately, the spacecraft data storage only allows us 512 data words, once each orbit. So our finest time resolution is about 100 minutes, and our typical spatial resolution is about 5°.

The purpose of the experiment is to measure temporal variations in X-ray sources anywhere in the sky, all the time. I chose two very different types of effects to discuss because I believe they are important scientifically and because they are illustrative of what we will be able to do with the satellite during the next two years.

The experiment already has seen all the strong sources in the UHURU catalog. It did that the first day. We have not yet found any new strong sources to add to the catalog, but we have found what appear to be very intense, very short duration transient sources.

Figure 2 contains portions of the raw data from three consecutive orbits. The numbers on the matrix boundary are grid coordinates which should enable reading our data matrices. These orbits have accumulation times of approximately one hour and have an average background of a few counts per resolution element.

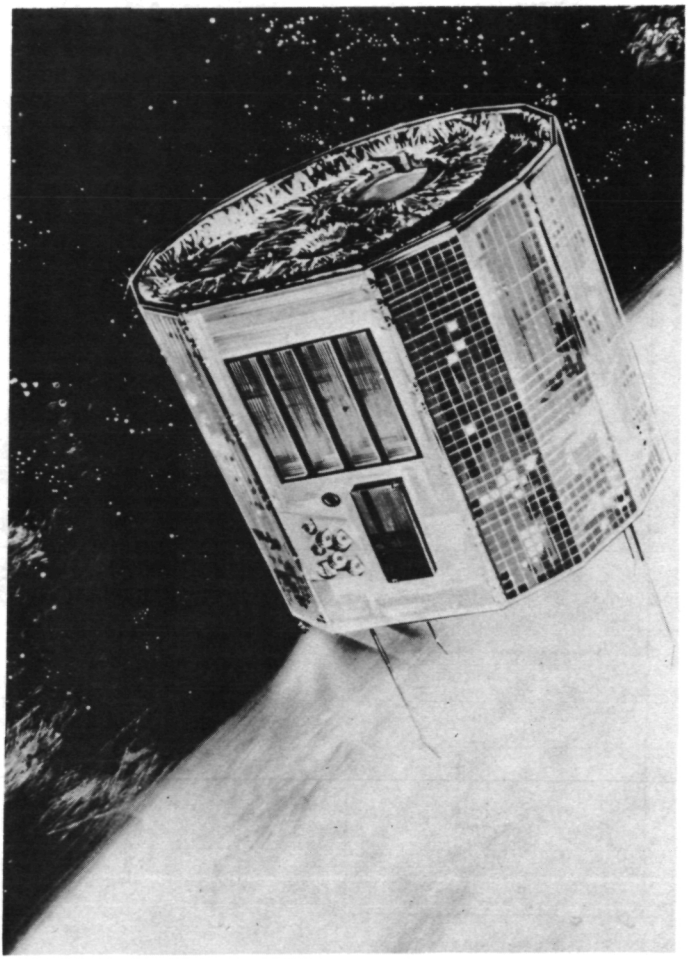

Figure 1. The UK-5 satellite.

In orbit 533, we get 35 counts in the box corresponding to the boundary between two elements, while we have only two counts in the same box in orbits 532 and 534. There is no catalogued source anywhere near this point, and there is no chance of the effect being a bit error. If the source was on for the whole orbit, it had an apparent magnitude of twice the Crab Nebula, but because we only see it during one orbit, it was probably on for a much shorter period. If the source was only on for a few seconds, it had an apparent magnitude of about 1000 times that of the Crab Nebula while it was on.

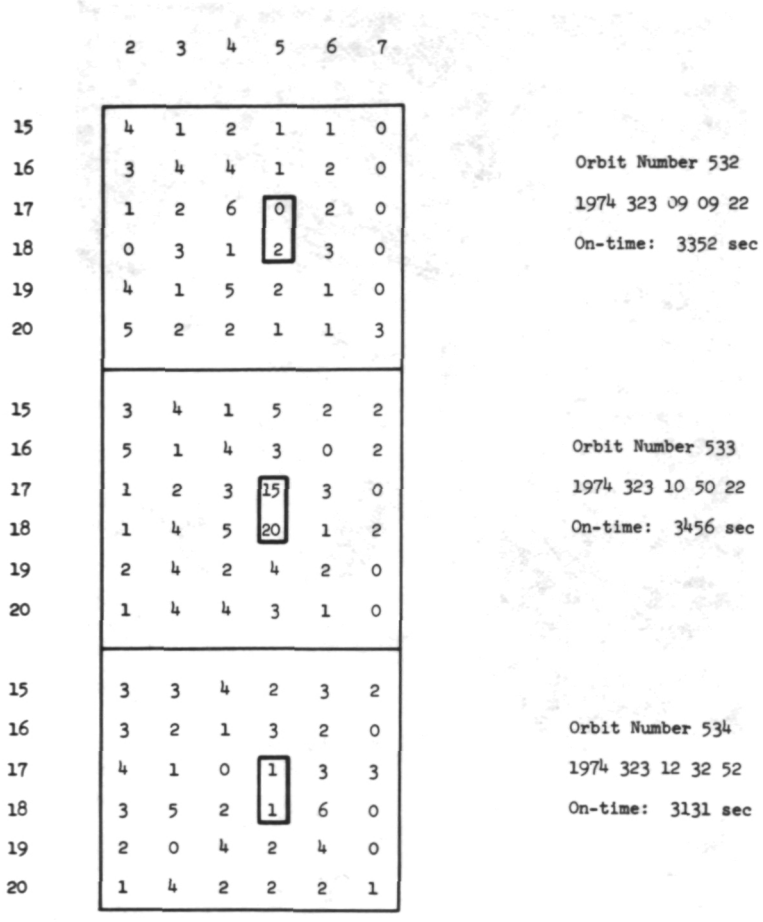

Figure 2. Raw data from UK-5 orbits 532 to 534.

The obvious possibilities for association are in supernovae in external galaxies and nearby flare stars, and perhaps even gamma-ray bursts. We sent a telegram to the International Astrophysical Union (IAU) giving the position and the time for the source, and we have also notified Tom Cline, whose paper follows ours and who is our resident gamma-ray "burstician."

The other result from UK-5 data to present is the apparent periodic modulation of the X-ray intensity of Cygnus X-1. Cygnus X-1 is supposed to be a black hole, accreting mass from its ordinary stellar companion in a binary system. Many groups have measured all types of intensity variations on all

time scales. But there is no verified modulation of the intensity with the 5.6-day period of the binary system.

If you view figure 3 closely, there is a very suggestive 5.6-day trend. The arrows I plotted are where the minima in the X-ray intensity would be if the source were eclipsing. The phase is a little bit doubtful, because I extrapolated from optical data. Because there are large variations in the source, which are uncorrelated with the binary period, I think we need more data to either prove or disprove the conjecture that the emission really has a 5.6-day modulation.

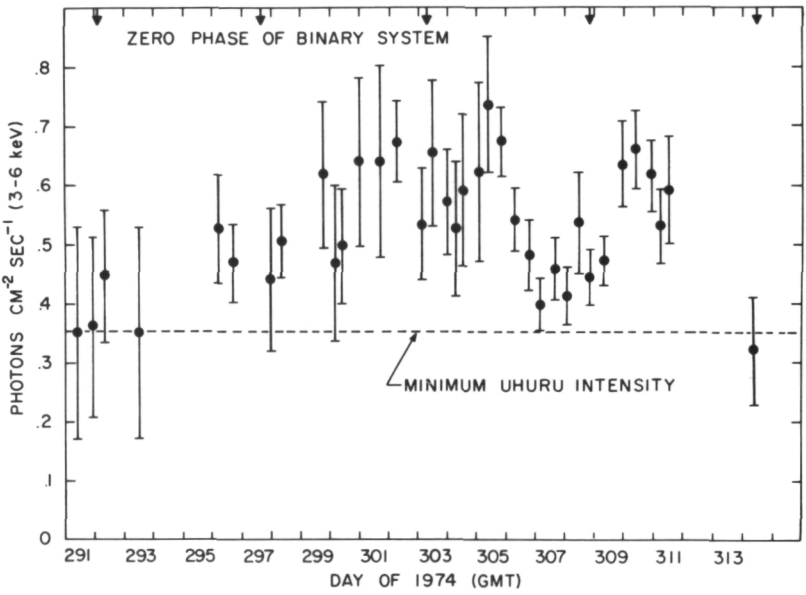

Figure 3. Apparent periodic modulation of Cygnus X-1 X-ray intensity from UK-5 data.

We do not need to fly another experiment to acquire the data. In fact, we do not even need any more money from Headquarters. The data just keep coming in, we keep folding it, and, if the effect is real, we expect it to be enhanced. If the effect is not real, we expect it to wash out.

Similar trends will be investigated in the data from other strong sources, all of which we will keep monitoring quasi-continuously for the lifetime of the satellite, because we see most of the sky every orbit. This assures us

that we will continue to find transient sources of both the short-lived variety and the longer lasting ones, which I think may provide us with the biggest scientific payoff of all.

We have the cooperation of the Information Processing Division here at Goddard processing virtually all our data within hours, and with such a monitor, the world is not going to miss anything spectacular. When the next, big, long-duration source occurs, we can be sure not only that we will see it, but also that every satellite in the sky and every telescope on the ground is going to have the opportunity to observe the infancy of an X-ray source within hours after its birth.

THE ENERGY AND SIZE SPECTRA OF COSMIC GAMMA-RAY BURSTS

Thomas L. Cline

Cosmic gamma-ray bursts are a newly discovered phenomenon in nature, having been found about a year and a half ago with the Vela satellite nuclear bomb-test monitoring system. One year ago, we reported that our IMP-6 results were the first independent confirmation of the existence of gamma-ray bursts, and they were the first unambiguous demonstration that the bursts did consist of photons. These results showed that the spectra peaked in the region of a few hundred keV, quite distinct from all other X-ray astronomy phenomena. Since that time, considerable progress has been made in the study of the phenomenology of cosmic gamma-ray bursts. Twelve or thirteen NASA and European satellites, in addition to the Velas, have occasionally detected gamma-ray bursts and have studied their spectra, their time histories, and their source directions in some varying detail. However, no identification of any source object has been made. Thus, we still do not know where the bursts come from or even how far away their sources are, what produced them, and what is the mechanism of that production. They may come from the edge of the solar system, which would require some bizarre phenomenon to be postulated. This source distance would make their source strength something like 10^{21} to 10^{23} J (10^{28} to 10^{30} erg). They could come from stellar distances, with source strengths at 10^{31} J (10^{38} erg), metagalactic regions at 10^{41} J (10^{48} erg), or cosmological distances at 10^{45} J (10^{52} erg). This maximum energy is the rest-mass equivalent of a star.

Since our report on the IMP-6 results in 1973, we have made two advances; the first, with IMP-7 data, concerns the energy spectra. Studies of the energy spectra may, of course, ultimately contribute to the understanding of the production mechanism. The first figure shows the spectra of the nine events seen with IMP-7 during the first year. All of these are clearly similar; a unique comparison spectrum is plotted in each case with the dashed curves. At the higher energies, the deviations are statistical in nature, and at the lower energies, where the statistical errors are very small, the curves follow the data very closely. The spectra on the right of figure 1 were taken in the eclipsing scan mode, in which the detector is turned on for only the half of each rotation during the time the experiment is facing the

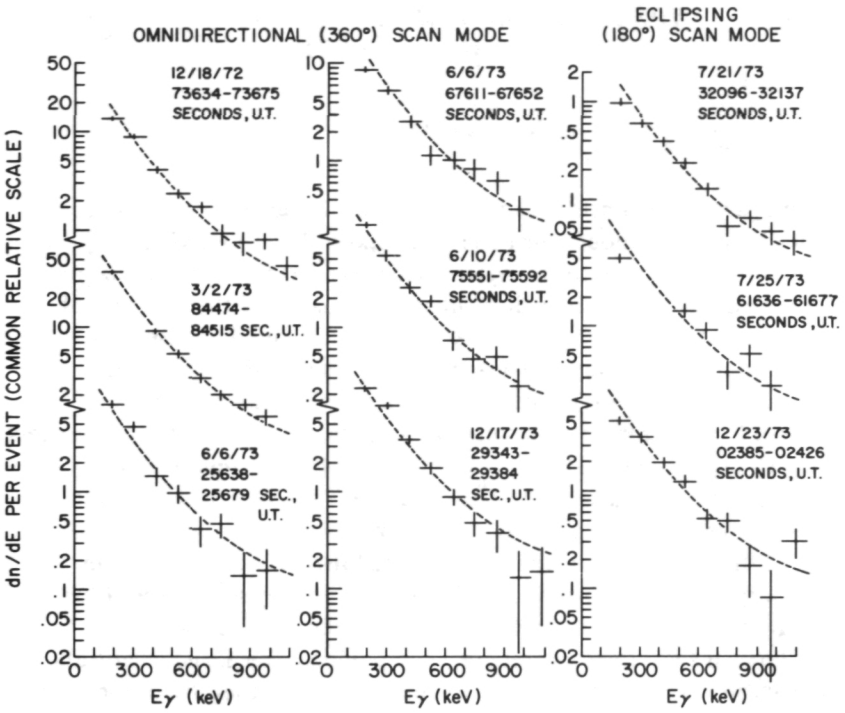

Figure 1. The event-average differential energy spectra of the nine gamma-ray burst events observed with IMP-7.

sun. In these cases, if the source is not in the solar hemisphere, there might be some attenuation due to interposed satellite material. This seems to have happened in perhaps two events, considering the low-energy lack of perfect fit; however, it is clear that all nine spectra are at least consistent with this common fit. This result indicates something unusual, considering the diversity and variation one normally sees in solar X-ray flares and other cosmic X-ray phenomena. Not only do all of these nine events fit this same spectrum, but every spectrum of every other gamma-ray burst measured with any other detector fits the same curve. J. Trombka discusses one of these as seen with Apollo in the following paper. There have also been several others, seen with OSOs; Ken Frost, Palumbo from Milan, Wheaton of the University of California, and a number of others have spectra of events which all fit this curve. As yet there is no satisfactory theoretical explanation of the observed spectral regularity of the bursts. In any case, the fact that all of them have the same spectrum is a feature which, of course, must come out of any model proposed for the production mechanism of gamma-ray bursts.

Quite separate from these considerations is the study of the size spectrum of gamma-ray bursts. This second study is one which has not yet produced a result as definitive as the study of energy spectra. The size spectrum is the distribution of event number versus apparent energy flux or size. The study of the size spectrum ultimately relates to the question of the spatial distribution of the origin volume of the sources. For example, an indefinitely extended, three-dimensional source volume, such as all of metagalactic space, would give a power-law index of -1.5, whereas a restricted source volume, such as the galaxy, would produce a size spectrum with a bend or even a cutoff, due to the two-dimensional disk shape and ultimately to the edge of the galaxy. As shown in figure 2, the raw spectrum of the original 1½ dozen Vela events does depart from the -1.5 index power law. Whether this bend is due to a source volume cutoff, such as that of our galaxy, or to an instrumental effect is the subject of immediate concern.

Our contention is that there is no convincing evidence for a bend in the size spectrum. Using IMP-7 and SAS-2 in coincidence, we have found some events that were too small to be seen by two Velas in coincidence. In fact, the Apollo event, discussed by Trombka, was not seen by two Velas in coincidence. The nine IMP-7–Vela events detected in one year are plotted in figure 2, indicating that with more sensitive instrumentation, the size spectrum can be continued with the same power law of a -1.5 index. (The other point shown represents the three SAS-2–Vela events.) These are verified events, as seen with at least two satellites in coincidence.

We had a successful balloon flight in May of a very large, 0.8-m^2 burst detector, for which we plotted the results at the top of figure 2. These are, of course, candidate gamma-ray bursts because they have been seen only with one detector and are not verified as such. The rate is corrected to take into account the fraction of the sky obscured by atmospheric collimation; as can be seen, it is over several per hour, or over a hundred a day. If this is the case, it would indicate a much greater extension of the -1.5 power-law size spectrum into the region of very weak, very distant events. It is not consistent with a galactic cutoff in the gamma-ray burst size spectrum.

Clearly, it will be necessary to fly two balloons in coincidence, separated by perhaps several hundred miles, in order to establish that this is a real effect. And that is, of course, what we intend to do next.

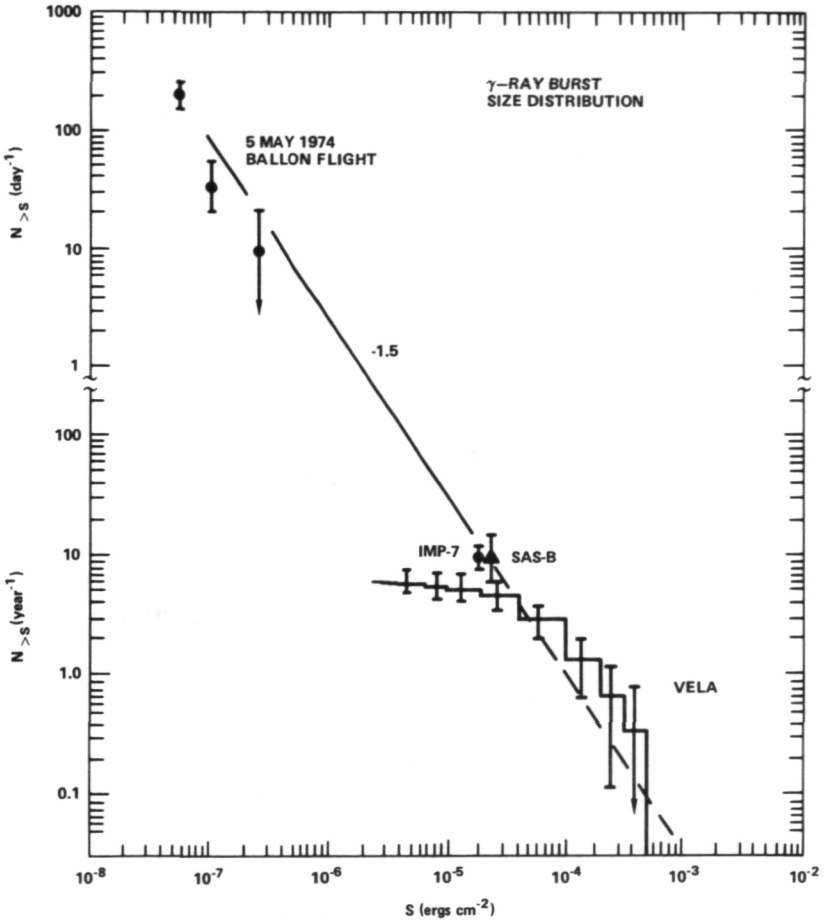

Figure 2. The size spectrum of gamma-ray bursts, including the candidate events observed with a May 4, 1974, balloon flight.

A GAMMA-RAY BURST FROM APOLLO-16

Jacob I. Trombka

The Apollo-16 X-ray and gamma-ray spectrometer observed a gamma-ray event on April 27, 1972, at approximately 10:50 GMT. This event was also observed by the Vela-A satellite. The members of the Apollo gamma-ray and X-ray team analyzed the data and also looked through the records of the total period of time of operation of both Apollo-15 and -16. We have obtained about four major results to present.

First, relative to this intensity distribution of burst events, we have not been able to find in over 322 hours of Apollo-15 and -16 data any other event with a magnitude of one-fourth of the intensity or greater than the burst discussed here. I think this is rather relevant to what Cline presented. Secondly, we have found a temporal distribution, detailed to the millisecond scale. Next, a gamma-ray differential energy spectrum over three decades, that is, from the keV to MeV range, was observed. And finally, a source direction was determined.

In figure 1, the temporal distribution is shown. This temporal distribution is characterized by what we think may be a precursor event, then an onset event, the main burst, an afterburst, and there is some evidence of a further pulse. The main burst contains three events: the first event about 2 seconds wide; the second event about 1-1/2 seconds wide; and finally, the last event about 1 second wide. The scale here is 300 milliseconds per division. This is the accumulation time we used to prepare this particular temporal distribution. This is not the finest time resolution that we are capable of, but, because of statistic problems, we had to use this scale. We are now looking at finer time resolutions and indeed seem to see even substructure within the structure shown.

Figure 2 shows the position location of the event. Essentially we used two methods to determine the position of the source. We were fortunate that the X-ray and gamma-ray burst occurred in the viewing direction of our X-ray and gamma-ray burst occured in the viewing direction of our X-ray detector, which is sensitive in the energy region from 1- to 7-keV and, therefore, very easily columnated. It has a very well defined 60° view of the sky. This is shown in figure 2 plotted in celestial coordinates.

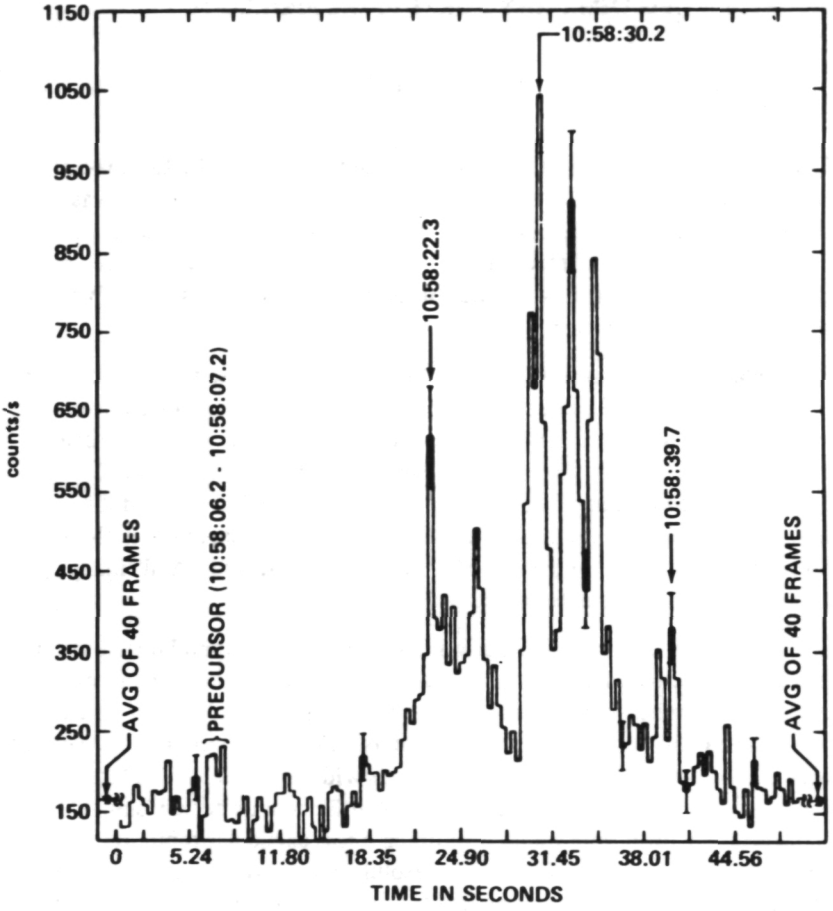

Figure 1. Temporal distribution of event of April 27, 1972.

The second method of localization was determined by the time of arrival of the gamma-ray pulse at Apollo and Vela. The Apollo and Vela spacecraft were 230,000 km apart, and we found that, by matching time profiles, the Vela detector saw the burst 250 ± 40 ms prior to the Apollo spacecraft. From the difference in time of arrival, we were able to describe a time cone shown in figure 2.

The intersection of these two observations of the X-ray detector and γ-ray detector indicate the direction, and, from the spectral shapes, we were able to localize the shaded region in figure 2 as the most likely area for that particular burst. The center of this region is about 22° to 23° R.A. and 60°dec.

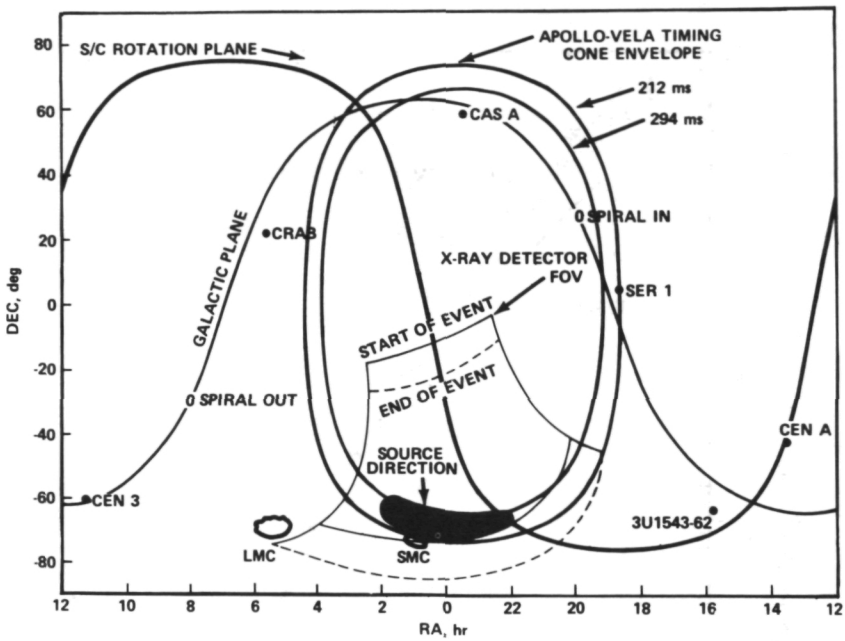

Figure 2. Position of the event of April 27, 1972.

The closest identified celestial object is the Small Magellanic Cloud, which is just at the edge of our observational cone.

The differential energy spectrum (figure 3) was obtained over four energy decades. This 1- to 7-keV region was observed by the X-ray detector, and the gamma-ray detector produced the rest of the spectrum from about 50 or 60 keV up to 5 MeV where the observation was made. We find that this distribution can be fitted either by two power laws or, if plotted on semilog paper, three exponentials.

In terms of the power-law distribution, we find that in the region from approximately 2 to 200 keV, a power of about 1.45, and from about 0.3 MeV to 3 MeV, a 2.6 slope seems to fit the case.

We also seem to indicate an excess above 3 MeV—an excess above this power-law distribution. How real that is is a little hard to say right now, but it seems to be real.

The result indicated by Tom Cline is observed in our data, that is, the spectral shapes are the same in that particular spectral region which is common to our detectors and those observed on OSO.

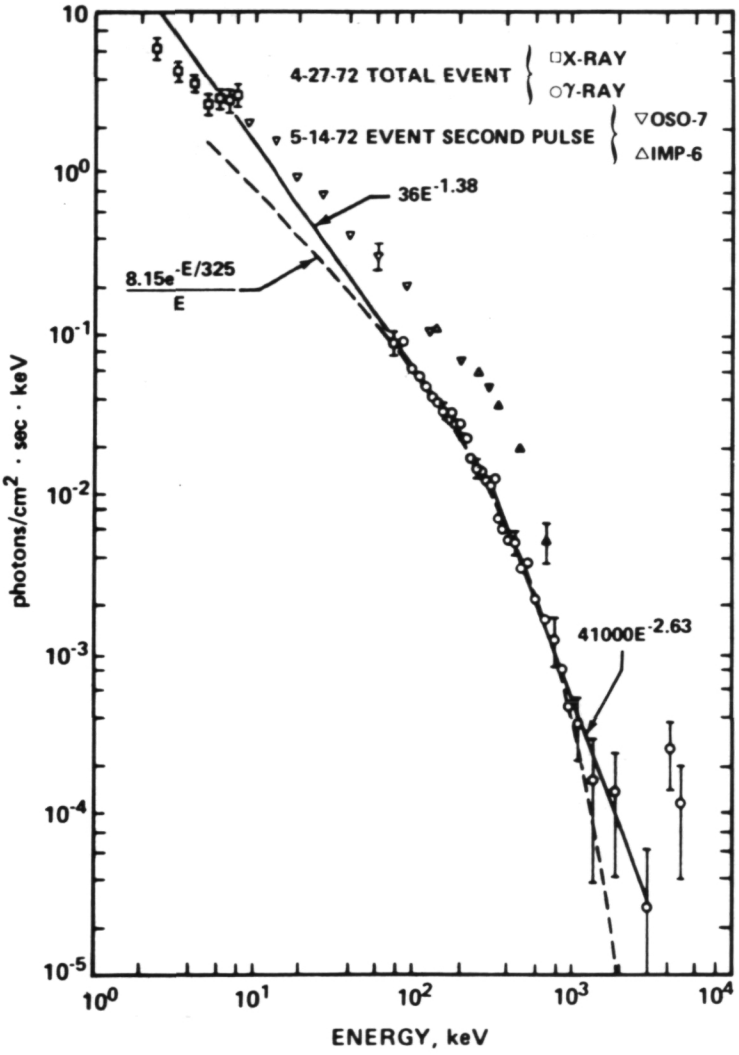

Figure 3. Energy spectrum of the event of April 27, 1972.

We have also observed the spectral shape on a finer time scale. If one looks on a very short time scale during the burst, one finds a persistent hard component which seems to stay. Then, as the burst goes into its most explosive mode, a very soft component rises and then decays. The average shape is shown in figure 3.

Our observations seem to be inconsistent with the Colgate-type supernova events but does not seem to be consistent with either accretionary or stellar flare modes of production.

THE MAGNETIC FIELD OF MERCURY

Kenneth W. Behannon

On March 29, 1974, the Goddard magnetometer onboard the Mariner-10 spacecraft made the first measurements of magnetic fields near the planet Mercury. The purpose of this paper is to briefly outline the results of the most recent analysis of these data. It should be stressed that with such a limited body of data from a single pass, it is not possible to be sure about the uniqueness of the results, but we feel there is a reasonable consistency among the various aspects of the picture we now have, and we look forward to another encounter to provide another set of measurements and verification of the model.

Figure 1 is the previously published plot of our 6-second average data during the encounter period. It is in the usual format in which we display our data, with the magnitude of the field, $\bar{F}$, the direction angles, ϕ and θ, and the RMS deviation of the field. These data illustrate dramatically that Mercury provided a global-sized obstacle to the solar wind, and it is the discovery of this field that is the major result of the mission for us to date.

Against the background interplanetary magnetic field of approximately 19 or 20 γ, it can be seen that there was a very dramatic increase in the field at the incoming bow shock around Mercury; a magnetosheath field; another substantial increase at the magnetopause boundary, accompanied by a rather significant change in angle, that is, the direction of the field; and then a relatively steady increase up to a maximum field of about 98 γ at closest approach of about 700 km above the surface, followed by a decrease. Unfortunately, on the outbound leg after closest approach, temporal variations made the interpretation of the spatial field characteristics in that region more difficult, but boundaries can be identified in more detailed data.

Figure 2 shows the 42-second average data in the magnetosphere in vector form. We have the data along the trajectory projected in a plane parallel to the ecliptic plane with X toward the sun and a perpendicular plane as viewed from the sun with positive Z toward the north ecliptic pole. We see in the latter projection that the field between the magnetopause crossings was essentially northward throughout the pass. In the ecliptic plane

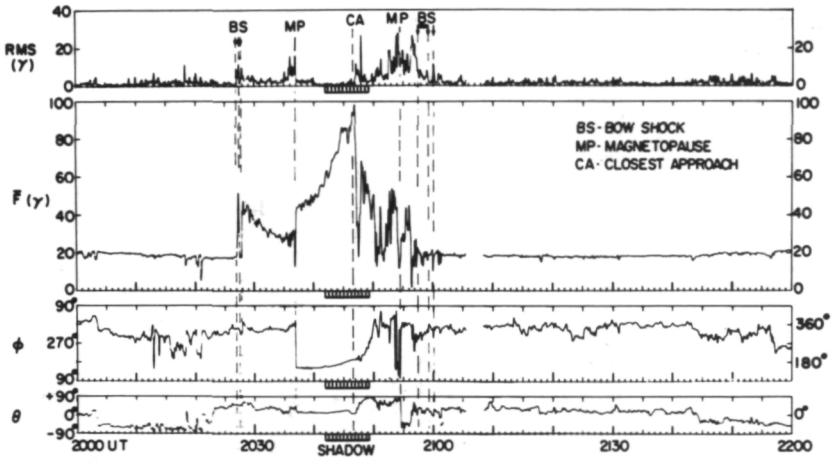

Figure 1. Magnetic field data for Mercury, March 29, 1974.

projection, we see that, as we came into the magnetosphere, the field was essentially pointing away from the planet, and then, after passing through this plane and going into the outbound approach of the magnetopause, we found the field rotating mostly into the Z direction, that is, out of the XY plane.

We have boundaries on this figure that have been scaled from the case of the earth—the magnetopause and a bow shock boundary. These boundaries fit both the locations and orientations of the observed boundaries taken from our data. The initial fit of an undistorted dipole model, which we presented as our preliminary result for this field, gave a moderately good fit to the data but required that the dipole be offset about one-half planetary radius from the center of the planet. This allowed the dipole moment to be about three-fifths of the value that could be inferred from the observed orientation and locations of the boundaries and the solar wind ram pressure. We now believe that these discrepancies were simply a result of neglecting the distortion of the field by the solar wind.

Figure 3 shows a Chapman-Ferraro field, or magnetosphere cavity for the earth. If there is such a cavity at Mercury, the planet as shown would fill a much larger volume of that cavity than the earth does. In that case, there would most probably be a much larger contribution to the observed field from distortion effects than for the earth, due to the difference in scale as we traverse the cavity. The fields that result from the distortion of the magnetosphere are those due to the current flowing on the cavity boundary,

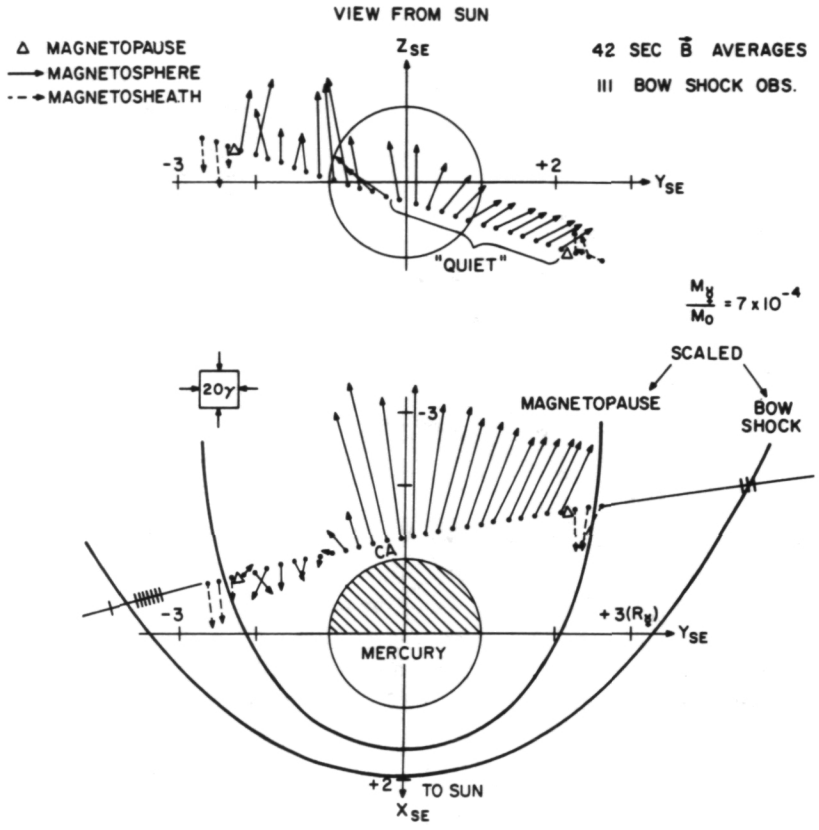

Figure 2. Mariner-10 42-second average magnetosphere data, March 29, 1974.

the Chapman-Ferraro fields, and then, with the formation of a tail field, the field due to a neutral sheet as shown in figure 3. If you imagine flying a trajectory on the antisolar side of the planet through this cavity, coming in below the equatorial plane and then going out above it in the direction parallel to the equatorial plane, we see that the field would first be away from the planet, and then, going outbound, it would be toward the planet; in a direction perpendicular to the equatorial plane, the field would be largely southward due to this neutral sheet contribution.

We are referring to the perturbation field part of the observation, and it would probably be somewhat less near the boundaries due to the oppositely-directed fields due to the surface currents. Our most recent analysis has consisted of a least squares fit to a spherical harmonic expansion of the

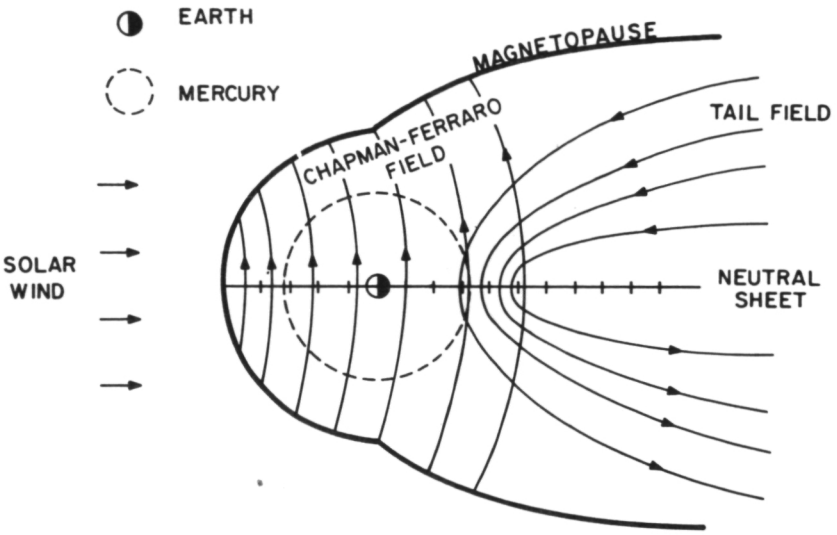

Figure 3. Chapman-Ferraro field for earth.

field. Our best result has been obtained for the case of a centered dipole that is internal to Mercury and includes external terms to the second degree. It is these external source terms which describe the additional distortion field. Figure 4 shows what we call the perturbation or distortion field. It is simply the observations minus the dipole part of our best fit to the data.

When we think back to figure 3, the Chapman-Ferraro cavity, we see that inbound we have the field in the ecliptic plane, generally pointing away from the planet and, when outbound, mostly pointing toward the planet. In the plane perpendicular to that as viewed from the sun, this perturbation field itself is mostly southward, growing larger toward the center of the magnetospheric cavity. So we feel we have quite good qualitative agreement with the concept of a magnetosphere with a magnetic tail and then a neutral sheet. Further, we have, for our centered dipole in this best-fit solution, a moment magnitude of 5×10^{22} gauss cm^3 compared to the moment of 5.6×10^{22} which is inferred from the boundary positions and the solar wind ram pressure. So we now have much better agreement with an independently determined value of magnetic moment.

In conclusion, we now believe that there is reasonably good agreement between the observations and a model which includes, in addition to an internal dipole, the effects of an earth-like distorted magnetosphere. In this case,

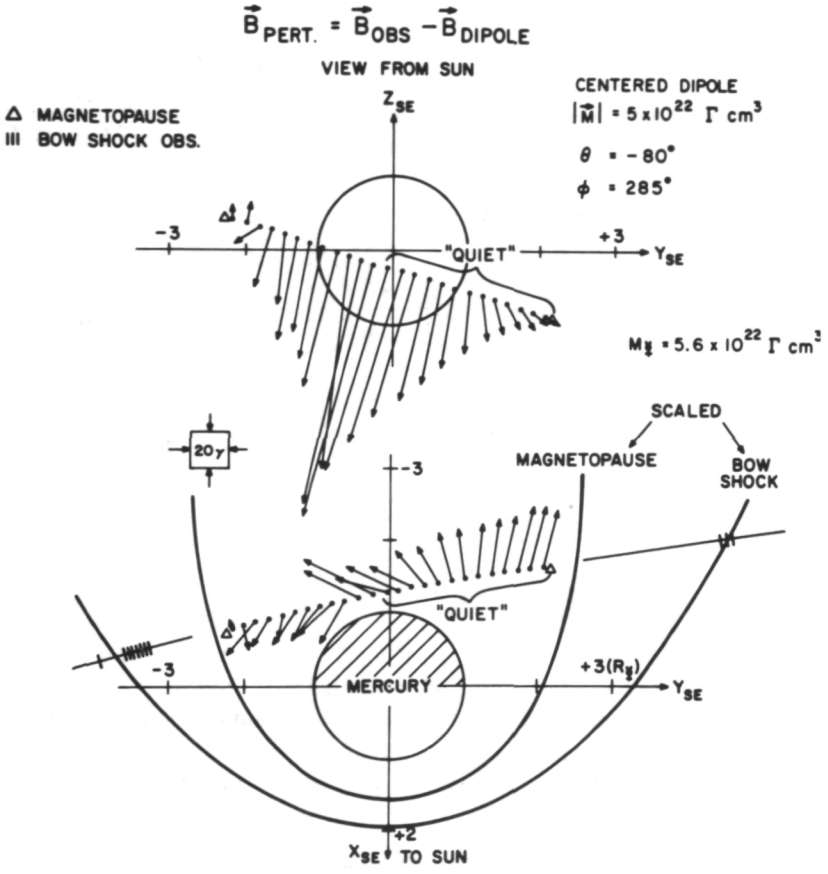

Figure 4. Perturbation field around Mercury.

the main difference is that the planet occupies a much larger volume of the magnetosphere, and therefore the effects due to the distortion are much more important.

The principal investigator on this experiment was Norman F. Ness and the coinvestigators were Kenneth W. Behannon, Ronald P. Lepping, and Y. C. Whang.

DISCUSSION

KING: How near to being perpendicular to the best-fit dipole was the incident solar wind?

BEHANNON: It was coming from slightly below the equatorial plane, but it was fairly close to being perpendicular. The best-fit dipole itself was very closely directed in the same orientation direction as our preliminary fit, although that one was offset. But it is close to being perpendicular to the planet's orbital plane around the sun.

PIEPER: All right, thank you very much, Ken. That's a great deal of information to get out of one pass by a planet. There was a second one but it was for television only and did not get these kinds of data.

INTERACTION OF THE SOLAR WIND WITH MERCURY

Richard E. Hartle

The electron measurements made by the Mariner-10 plasma-science instrument and the interpretations proposed by the plasma-science team are the basis of my discussion. Specially emphasized is how the solar wind interaction related to the atmosphere of Mercury.

Electron measurements were made by a hemispherical electrostatic analyzer facing the antisolar direction. Some of the measurements made at Mercury encounter are indicated in figure 1, which represents one hour of data during the encounter period on March 29, 1974. The time scale is indicated at the bottom of the figure: zero is the time of closest approach. The upper two panels correspond to 2 of our 15 energy windows. The middle panel is our lowest energy window, and the upper one is an intermediate energy channel. The bottom panel gives the electron density derived from the spectrum. The left of figure 1 contains typical solar wind spectra, giving an electron density of about $17/cm^3$ and a wind speed of about 630 km/s.

At encounter, we observed a strong interaction when Mariner-10 crossed a bow shock at about -19 min, indicated by the abrupt increase in the density of about a factor of two. This is due to the fact that there was a strong increase in the fluxes in all energy channels except the lowest one. The spacecraft then traversed into a magnetosheath-like region similar to the earth's. At approximately -10 min, Mariner-10 crossed a boundary very similar to the earth's magnetopause, which was characterized by a strong increase in the high energy channels and an abrupt drop in the fluxes in the low energy channels, being reflected by the drop in the density to $1/cm^3$. The spacecraft then passed through the cavity region and encountered a second magnetopause boundary at about +5 min, went into a magnetosheath again, and finally, between about +12 and +17 min, passed through a highly disturbed region which we interpret as a pulsation shock.

The features that I have described here are consistent with the observations made by the magnetometer team as discussed by Behannon previously. These observations clearly indicate that the obstacle to solar-wind flow is global in scale. Thus, the solar wind is deflected around the planet, resulting in the formation of a bow shock.

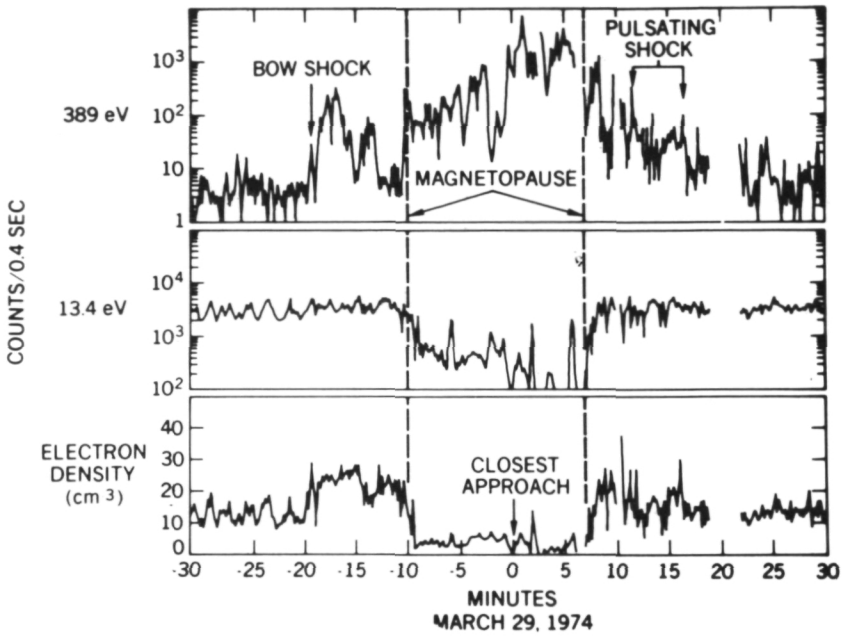

Figure 1. Mariner-10 plasma science experiment data for March 29, 1974.

We have considered a number of possible interaction modes. One possibility is for the solar wind to be deflected by atmospheric mass loading. This mechanism is indicated in the bottom portion of figure 2, where the X-axis points towards the sun. In order for the atmosphere alone to stand off the solar wind, we investigated whether or not the free streaming solar wind can be stopped as it passes through the atmosphere. So we calculated the change in the velocity as the solar wind passes through the atmosphere. The mass addition here corresponds to atmospheric ions that are born in the wind and then accelerated by the solar wind electric field. The light ions are treated by a fluid description while the heavy ions are treated by a kinetic model. In either case, the momentum change of the wind is directly dependent upon the density of the neutral atmosphere. Upper bounds to the neutral atmosphere have been placed by the Mariner-10 ultraviolet spectrometer. We have used these limits and found that the neutral atmosphere is not dense enough to prevent the solar wind from striking the surface where it would then be absorbed, thereby preventing the formation of a bow shock.

We must conclude that the atmosphere is not responsible for stopping the solar wind, and that the obstacle to solar wind flow must be a magnetic

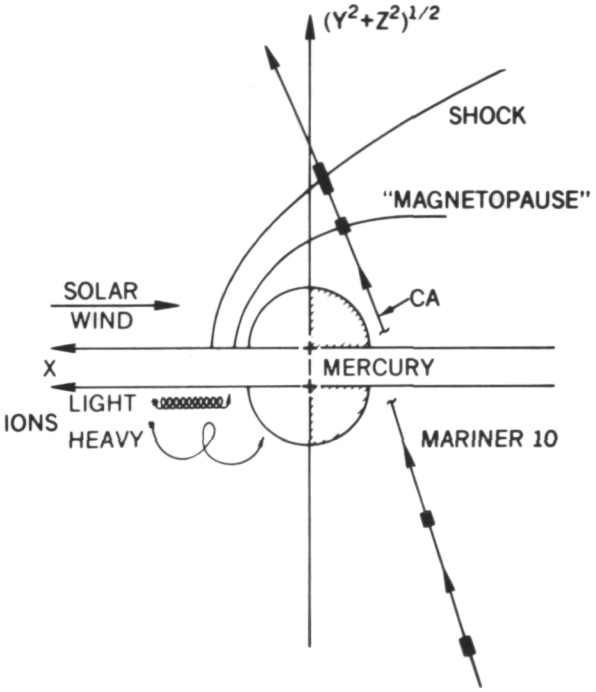

Figure 2. Interaction modes of the solar wind with Mercury.

field. The origin of the field may be an intrinsic planetary field or may be induced by the solar wind. One possibility is indicated in the top portion of figure 2 where a model magnetopause and a shock boundary are shown for a planet-centered dipole. The corresponding boundary crossings determined by the plasma-science instrument are consistent with this model.

The atmosphere is therefore not important for deflecting the solar wind; but, in contrast, the solar wind might be an important source for the atmosphere. What I have in mind is accretion, where a small fraction of the solar wind ions leak into the magnetosphere and are absorbed at the surface.

The only constituent that was detected and measured by the ultraviolet spectrometer was helium. These measurements indicate that the atmosphere of Mercury is collisionless or is an exosphere. We have constructed a model helium exosphere, as shown in figure 3. In this figure, the predicted helium densities are given as a function of planetocentric distance in units of planet radius. Because the surface properties of Mercury were

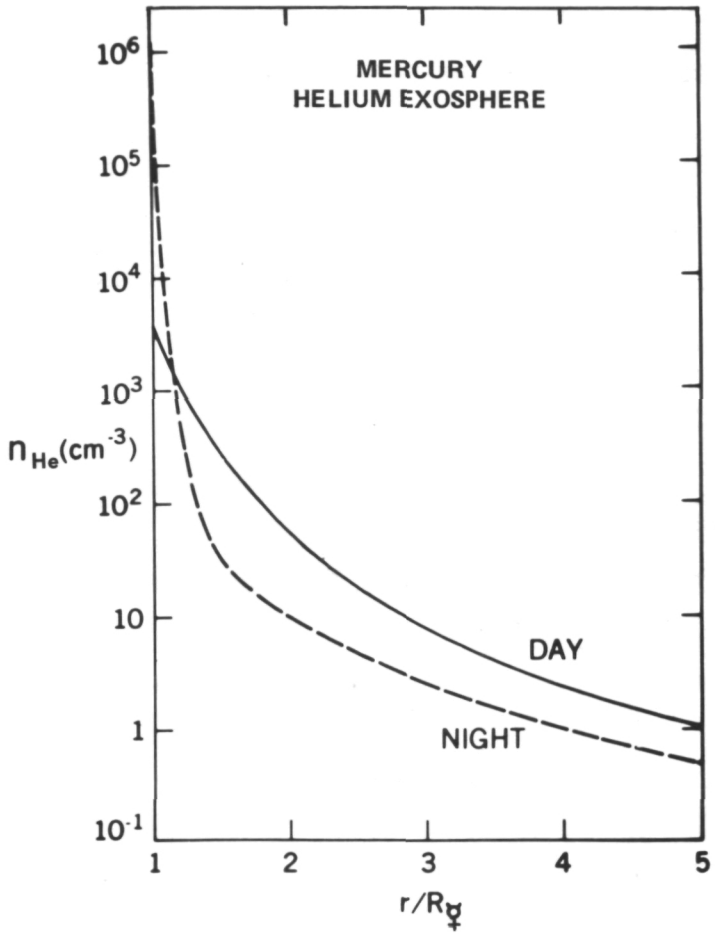

Figure 3. Mercury helium exposure.

found to be similar to those of the moon, we have placed the same constraints on Mercury's exosphere as those of the moon, which results in a nighttime surface density that is about 200 times greater than the daytime density.

The concentration levels have been set by adjusting the density to give the limb intensity observed by the ultraviolet spectrometer. The limb intensity at an altitude of 400 km is 20 rayleighs, due to solar radiation that is resonantly scattered from helium at 584 Å. The solar wind accretion rate is simply equal to the atmospheric escape loss. This translates into a magnetospheric capture fraction of 6/10,000 of the solar wind flux. This is compared to the earth's capture fraction of about 1/10,000.

We do expect a larger capture fraction at Mercury, primarily due to the fact that the magnetopause is so close to the surface of the planet. On the other hand, if solar wind accretion is not sufficient, the source would then be outgassing from the interior. We can use this model to estimate an upper limit for the outgassing rate of Mercury. In doing so, we find an upper limit for the flux to be $10^6/cm^2/s$.

To summarize, we have observed a strong solar wind interaction at Mercury involving a bow shock, a magnetosheath, and a magnetosphere-like region. The obstacle to solar wind flow was found to be a magnetic field, while the atmosphere played no significant role in the interaction. However, we find that the solar wind may be an important accretion source for helium. Whether or not the solar wind is sufficient, our model predicts an upper limit to the outgassing rate.

DISCUSSION

HARTELL: We only have an observation for helium, so there is no way to place a constraint on that.

VOICE: What is the arrangement for helium as compared to that produced by (inaudible)?

HARTELL: The outgassing rate is assumed to be from thorium-uranium decay.

VOICE: Throughout the whole planet?

HARTELL: I do not know where the source is. All I can do is place an upper bound on the flux at the surface.

VOICE: You have a planet and you have a true value for uranium-thorium where it would be uranium-thorium . . .

HARTELL: There are several models. They are not all in agreement.

VOICE: Is this roughly consistent with at least some of the models or what does it tell you about uranium-thorium?

HARTELL: It is probably consistent with John Lewis' model, within an order of magnitude.

DISSIPATION OF THE MARTIAN DUST STORM OF 1971

Barney J. Conrath

At the time Mariner-9 spacecraft was injected into a Martian orbit, in November 1971, an intense, planet-wide dust storm was in progress. The infrared spectroscopy experiment which was carried on the spacecraft obtained information on the thermal structure of the atmosphere, both during a portion of the dust storm and during its subsequent dissipation.

Results of some of these data are seen in figure 1. Temperature profiles for the atmosphere were obtained from the surface up to about 40 km. The sampled temperatures at the 30-km level are plotted as a function of time in days from the beginning of the mission. The data were subdivided according to local time, and the spread in the data points indicates the presence of a diurnal thermal wave.

The dust storm continued for about the first 25 days of the mission, and the atmospheric temperatures remained elevated during that time. When the dust storm began to dissipate and dust settled, the mean atmospheric temperature decreased as did the amplitude of the diurnal wave, as indicated by the curves which have been fit to the data.

If one assumes that the elevated temperatures were due to direct absorption of solar energy by the atmospheric dust, it is possible from these data to estimate the time behavior of the dust optical depth, which is essentially a measure of the total dust in an atmospheric column above a given level. The results of one such inference are shown in figure 2 where the normalized dust optical depth is plotted as a function of time. The solid curve represents the behavior of the optical depth deduced from the temperature data in figure 1. It is essentially exponential in character with an e-folding time of about 60 days. While we have only shown data for one particular atmospheric level, a similar analysis was carried out at many different atmospheric levels from the surface up to about 40 km with essentially the same result, that is, the same exponential behavior with the same e-folding time. Therefore, this curve can be regarded as pertaining to essentially all atmospheric levels.

Using these observations, we first attempted to fit a model which assumed pure Stokes-Cunningham settling and a completely stagnant atmosphere.

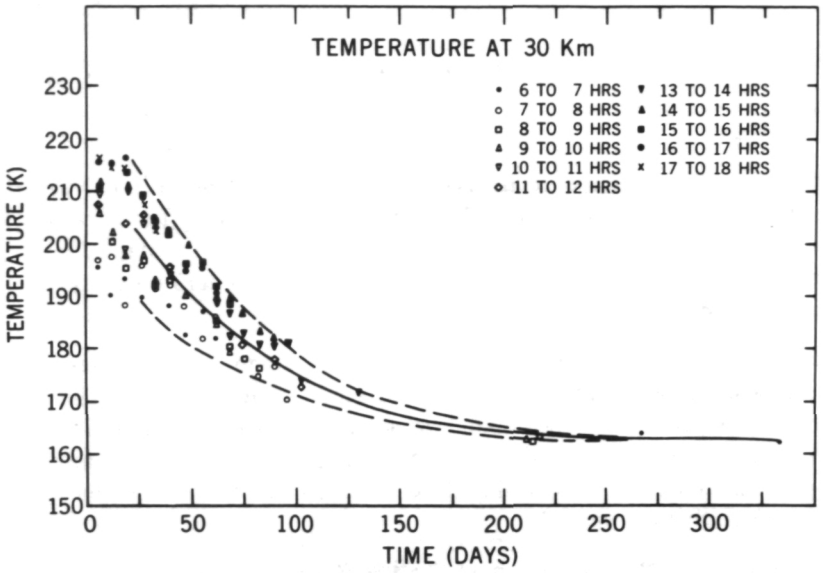

Figure 1. Temperature at 30 km.

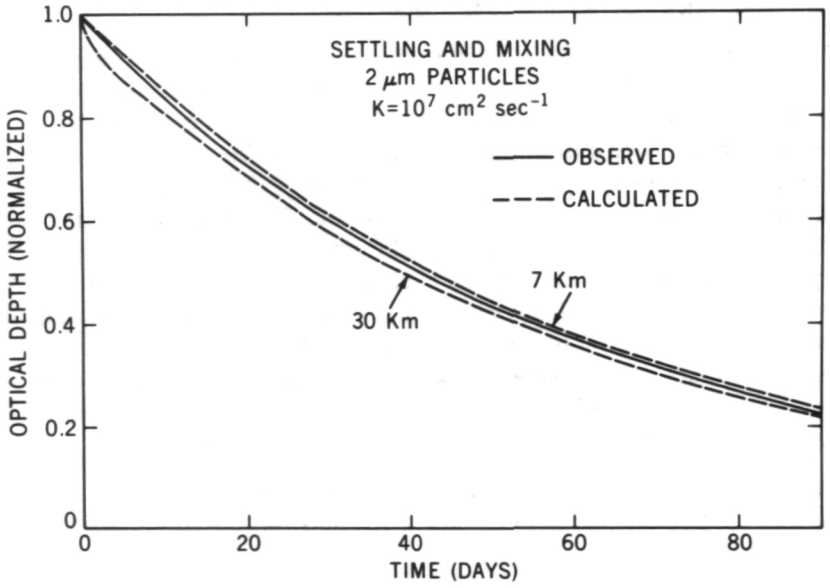

Figure 2. Dust dissipation for Martian dust storm and the Stokes-Cunningham settling model for 0.5-μm particles.

The results of the calculation for such a model for 0.5-μm dust particles are shown by the broken line. In this model, the dust dissipates much more rapidly at higher levels, such as the 30-km level, than at the lower levels, such as the 7-km level. Obviously, this type model does not fit the observations at all.

Next we added atmospheric mixing to the model, with results as seen in figure 3. Again, normalized optical depth as a function of time is shown. The solid curve is the same observational curve shown in figure 2. The atmospheric mixing processes were parameterized in terms of a single effective eddy-diffusion coefficient, K. By adjusting the particle size and the eddy-diffusion coefficient, we were able to bring the theoretical calculations into reasonable agreement with the observations at all levels.

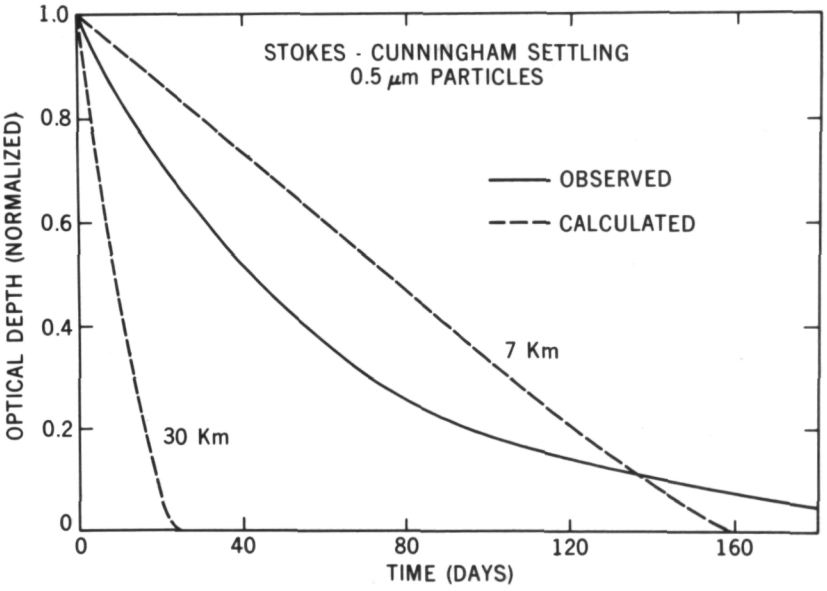

Figure 3. Dust dissipation for the Martian dust storm and the settling and mixing model for 2-μm particles ($K = 10^7$ cm^2 s^{-1}).

Thus, by studying the thermal behavior of the atmosphere during the dissipation of the storm, we are able to infer two parameters. One is that the mean dust particle size was about 2 μm, but perhaps more interesting, the effective eddy-diffusion coefficient was about 10^7cm^2 s^{-1}. This value means that the entire lower scale height of the Martian atmosphere could be

overturned on a time scale of about one day with this type mixing. For comparison, in the earth's atmosphere, the overturning time would be perhaps two orders of magnitude longer. So this is indeed remarkably strong mixing, at least by terrestrial standards.

DISCUSSION

TEPPER: How unique is the solution to the particle size and K?

CONRATH: The particle size is unique because it essentially establishes the time scale or the e-folding time involved. We can establish a lower limit on K. The mixing can be increased and, of course, once the atmosphere is completely mixed you can keep increasing K and it does not affect the results significantly.

NORTHROP: Does the calculational result depend on what your initial vertical distribution is? How do you start that one?

CONRATH: In the case of the Stokes-Cunningham settling, we start out by assuming a completely mixed state, as we think it would probably be during the dust storm.

NORTHROP: Do you mean it is uniformly mixed, or it is uniformly distributed?

CONRATH: The dust mixing ratio is uniform up to a certain height.

VOICE: Does the dust affect the measured infrared spectra?

CONRATH: There are regions of anomolous dispersion which we see in our infrared spectra, features which are due to the dust.

VOICE: It should be optically thin, shouldn't it?

CONRATH: We do see through it. We can see through it well enough to make our temperature determinations at 15 μm, for example.

VOICE: So you are right down to the surface?

CONRATH: Yes.

VOICE: Did you apply this model to the onset of the storm?

CONRATH: No, because we are trying to take advantage of the time rate of change of the temperature. By using other data you can look at what is going on during the storm. For example, the TV pictures that were taken at the same time show that the dust was mixed during the storm up to about five scale heights. You can ask what the eddy-diffusion coefficient has to be to maintain that mixing? Again, it comes out to be 10^7 or 10^8 cm^2 s^{-1}.

LEE WAVES IN THE MARTIAN ATMOSPHERE

Joseph A. Pirraglia

The Mariner-9 television pictures of Mars show that the middle latitudes of the Northern Hemisphere during the winter were covered by waves in the clouds that make up the polar hood. In many instances, the waves were obviously related to the atmospheric gravity waves in the lee of mountains or craters with raised ridges. These atmospheric waves very likely have little consequence on the circulation of the Martian atmosphere, but beyond any purely classical interest, the waves present a diagnostic method of determining the wind velocities and shears, independent of any of the circulation models. Indeed, being a more direct determination, they should serve as a constraint on any of the results obtained from such circulation models.

Figure 1 is a picture of the cloud waves due to the wind blowing across this 100-km-diameter frost-filled crater. There are two sets of waves, a transverse set and a diverging set contained in, roughly, a wedge-shaped region. The wavelength along the center of the wedge is approximately 50 km and the angle between the apparent wind direction and the edge of the wedge is approximately 20°. Both the wavelength and the wedge angle depend upon the parameters of the airstream blowing across the crater and the stability of the atmosphere at the time.

The stability of the atmosphere is known from the temperature structure as determined by the infrared interferometer spectrometer (IRIS) data. Using this stability we attempted to construct the airstream model by trial and error which, when used in calculations based on a theory of mountain lee waves, will give us the correct wavelength and wedge angle.

The airstream model (figure 2) that we used is a simple two-layer model in which the velocity is uniform in both layers, and in which the density of the atmosphere decreases exponentially with altitude. Such a model would be subject to Kelvin-Helmholtz instabilities at all wave numbers. For our use, you can show that this model is a good approximation to a model in which the velocity changes continuously between the two layers, in which case, the Kelvin-Helmholtz instabilities would be confined to a narrow band of wave numbers.

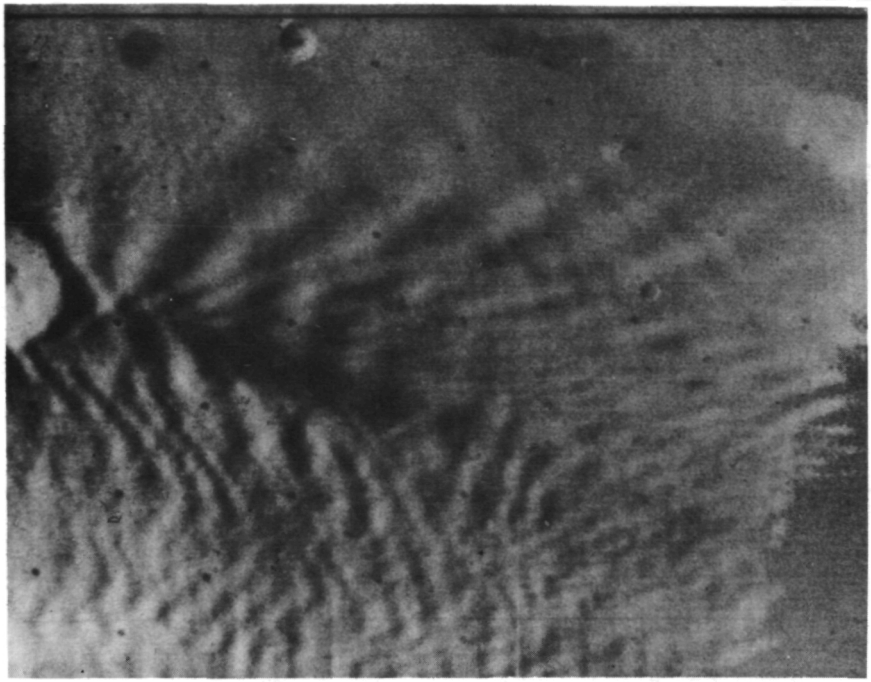

Figure 1. Cloud waves due to wind over Martian 100-km-diameter crater.

In any event, the airstream parameters that give us the wavelength and angle that we are seeking are as shown. It has a 10-km-deep, 40-m/s layer below an 80-m/s layer extending to the top of the atmosphere.

A schematic of the cross section of the crater is also shown. The altitude of the crater is not important in the determination of the wave pattern; it affects only the amplitude of the waves.

The contours shown are not a simulation of the wave clouds, but rather, they are the constant phase surfaces of the wave generated by the model wind blowing across the crater.

To obtain the amplitude, we must multiply these constant phase surfaces by the proper amplitude functions. In any event, these contours of the transverse and diverging waves show that we do indeed have the 60-km wavelength and approximately 20° between the wind direction and the edge of the wave pattern, indicating that our model does approximate the wind at the time of the picture.

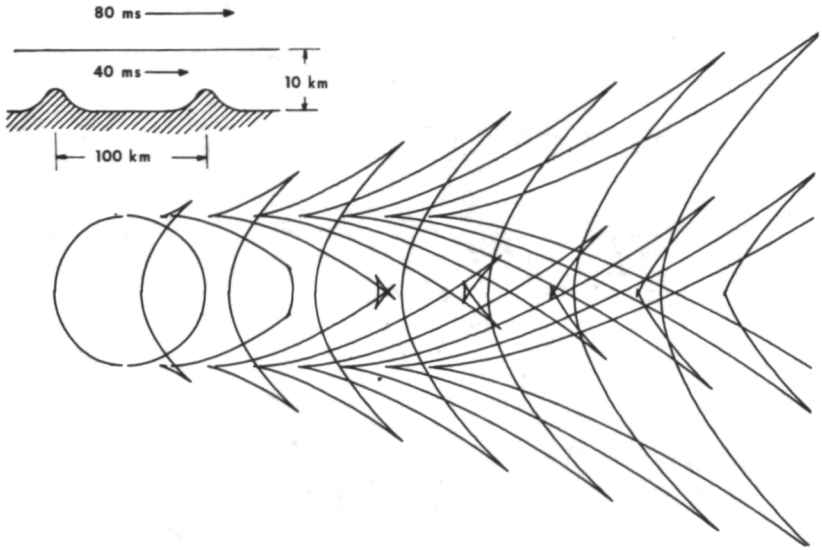

Figure 2. Airstream model and crater schematic.

Except for one case that has not been analyzed, the wavelengths in most of the television pictures indicate that the winds are somewhat less than we have obtained here. In many cases, they are probably on the order of 20 m/s. This is in substantial agreement with the circulation models that have been developed. In particular, a two-layer numerical model by Leovy and Mintz, under approximately the same conditions that we have here, predicts winds of approximately 30 m/s in the lower layer and 70 m/s in the upper layer.

Thus, our results would indicate that the circulation models developed give a more accurate picture of the Martian winds than the speculations of the 80-m/s winds ranging over wide areas of the surface. None of the wavelengths would indicate that we could have 80-m/s winds at the surface.

DISCUSSION

VOICE: There is something I do not understand. If the model is unstable, why do you need the crater to produce the waves or (inaudible)?

PIRRAGLIA: It is not unstable. The atmosphere was stable at the time.

VOICE: I thought you said it was Kelvin-Helmholtz unstable?

PIRRAGLIA: No. I said this two-layer model is subject to the Kelvin-Holmholtz instabilities.

VOICE: Are these two-layer models Kelvin-Helmholtz unstable?

PIRRAGLIA: Yes, they are unstable. But this two-layer model, for our purposes, is a good approximation to a model in which you have a lower layer connected continuously to an upper layer. In that case, the Kelvin-Helmholtz instabilities would be confined to a narrower band. My statement was an attempt to explain why you see a fixed rather than random wave pattern waves due to the Kelvin-Helmholtz instabilities. I think that model could easily be out of range of the Kelvin-Helmholtz instabilities.

VOICE: I thought the higher velocities were required to explain the drifting of dust.

PIRRAGLIA: No, I do not think you need anything of that magnitude.

VOICE: Do you generalize over the globe or do you still have regions of locally high winds.

PIRRAGLIA: There is some speculation that these high winds range over wide areas of the surface. They may very well be only a local phenomena. But I think from the circulation models and the lee waves, there is no indication of winds of that magnitude.

THE FLEXING OF JUPITER'S MAGNETOSPHERE

Theodore G. Northrop

This paper describes work I did when I was in Iowa City with Van Allen. It was actually done with Thomsen and Goertz at the University of Iowa. It was prompted by an observation made by Van Allen which I will describe.

What is commonly called the wiggle diagram is seen in figure 1. It is a plot of the trajectory of Pioneer-10 in the magnetic coordinates of Jupiter. Of course, the inclination of the orbit does not wiggle. What is really happening is that the magnetic dipole, which is tilted at 10° to the rotation axis, wobbles, so the relative magnetic latitude of the spacecraft changes.

The energetic particles in the plasma are most intense in the magnetic equatorial plane due to the effects of the magnetic field and the rotation. The rotational axis has a wobbling effect.

As the spacecraft approaches Jupiter, its distance from the equatorial plane varies with the 10-hour rotation periodicity because of the 10° angle between the rotational axis and the dipole.

In addition, instruments that are counting protons, electrons, orbital plasma density, or measuring the magnetic field, should also see a 10-hour variation; this is, in fact, observed.

Knowing the phase of rotation of the planet and knowing where the spacecraft is, you should be able to predict when the maxima and minima should occur.

For example, if a spacecraft is inbound, a little under the equatorial plane, you should get the maximum in the count rates when the magnetic dipole, which is normal to the magnetic equatorial plane, is pointing towards the spacecraft, and the minimum 180° away. On the outbound, you are going to have the reverse situation. Therefore, we should be able to predict the times of occurrence of the maxima and the minima in the count rates on the inbound and outbound spacecraft trajectories.

Figure 2 is a polar plot; the radius is in Jovian radii, and the azimuth is the system III longitude of the Pioneer-10 at which various events occurred. The circled dots are the phases at which the maxima were seen on the outbound path. The circled crosses are the minima on the outbound path.

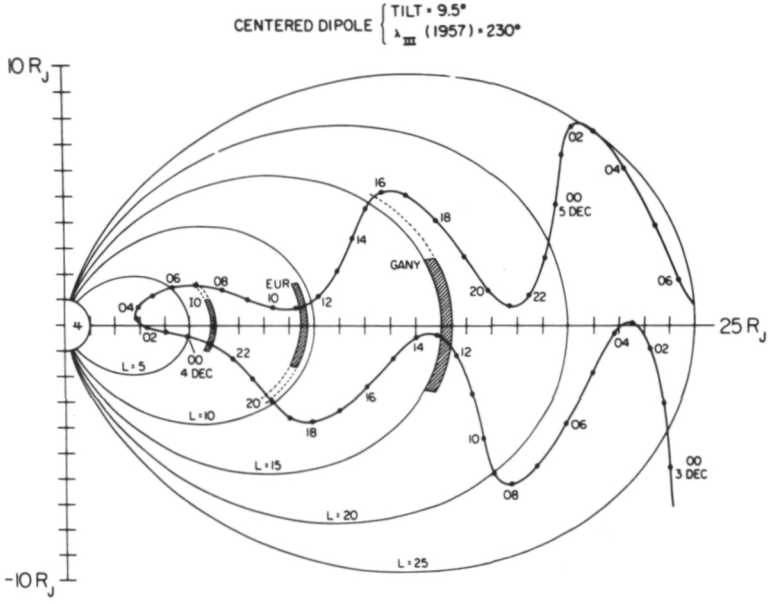

Figure 1. The time-labeled trace of Pioneer-10 in magnetic polar coordinates (magnetic meridian plane projection) for the planetary dipolar model as specified. The cross-hatching shows the regions that bound the orbits of Io, Europa, and Ganymede in such a coordinate system. The time is earth-received time.

If Jupiter's magnetosphere were rotating rigidly, one would expect to see those points arrayed along the $\lambda_{III} = 222°$ and $= 42°$ lines.

The inbound trajectory I might mention, is much more mysterious and less satisfactory. The inbound data are the noncircled plus signs and points.

The outbound maxima and minima represent, because of the direction of the rotation of Jupiter, a time delay. In other words, on the outbound trajectory, the maxima and minima are both occurring after the expected time.

When Van Allen discovered this, we figured that this is easy to explain; the disk is not in fact rigid—it is flexible. In other words, what is happening near the center is not felt instantly further away; it is only felt further away at the appropriate signal propagation velocity which, in this case, is the Alfvén speed.

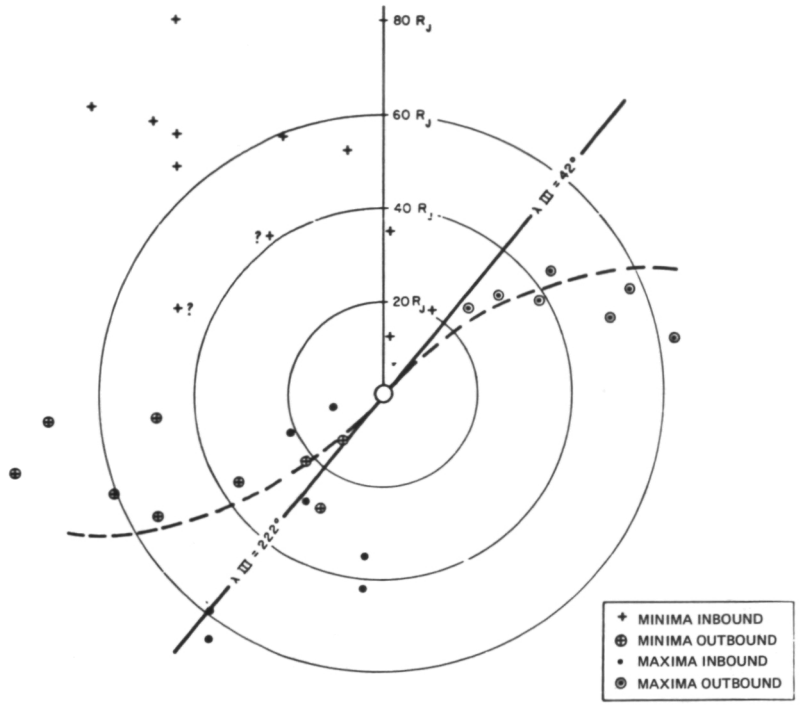

Figure 2. System-III longitudes of Pioneer at times of maxima and minima in electron fluxes.

We made a mathematical model of this. We assumed that information about the location of the magnetic dipole is transmitted at the Alfvén group velocity, which is always directed along the field line in the frame comoving with the plasma. We did not assume corotation of the plasma with Jupiter. We worked out theoretically, in general, what the time delay should be. Then we put into this rather unlovely expression the results of models by Chandrasekhar and by Mestel for mass loss from rotating stars. We had hoped that one would be able to deduce, from the unlovely expression, the Alfvén velocity as a function of radius, which would give us a measure of the cold plasma densities as a function of radius, which would be lovely to have.

When we put in the Mestel solution, the Alfvén velocity in fact disappeared, and we got a simple result. The theoretical result is the dashed line in figure 2. This is a very crude model. We did not do a complete

magnetohydrodynamic solution of the rotation, but the model gives reasonable semblance of what is observed.

On the inbound path, the maxima and minima occurred before they should. In other words, in some way the plasma knew where it was supposed to be before it was told to be there, and we do not understand this. It could be explained in terms of a rapid sweep forward of the field lines between the dawn and the noon meridian longitudes, and that would require rather large electric fields on the order of 2 V/m in the polar regions. That is where it stands now. We need a complete magnetohydrodynamic solution to the problem.

DISCUSSION

SMITH: I was told at Ames on Monday that ingress and egress were very symmetric on the Pioneer-11 (inaudible).

NORTHROP: Yes. Pioneer-11, I believe went around the other way actually. It came in more on the dawn side and went out somewhat oppositely from the Pioneer-10.

SMITH: But there is general agreement that the ingress on Pioneer-10 was during some disturbed time.

NORTHROP: That is true.

VOICE: What magnetic field model did you use?

NORTHROP: We have used observed fields. Some of the Jovian field lines are in fact open. The Iowa group know this for certain now, that many of the field lines are open beyond about 30 R_J. The field lines leave the planet and head for the Equator, but then they curve away from the Equator before reaching it. The rapid drops to magnetosheath conditions always occur when the field lines are going away from the magnetic equatorial plane, they have found. There will be a preprint coming out on that soon. The ones which come up near the poles come out and then do that. The ones that come out near the Equator still close. It depends how far out you are as to which lines are closed. But there certainly are open field lines along which the plasma is escaping. We just took the simplest MHD solution given by Chandrasekhar and later by Mestel. There are lots of problems with our model, admittedly.

JUPITER'S 10.4-cm SYNCHROTRON RADIATION

Thomas J. Birmingham

For about the past 15 years, radio astronomers have realized that Jupiter is the source of very strong, nonthermal fluxes in the decimeter wavelength region. Characteristics of this radiation have led radio astronomers to the rather firm conclusion that this component of Jupiter's spectrum is synchrotron radiation emitted by very energetic electrons spiraling in the strong magnetic field of Jupiter's magnetosphere.

Aboard Pioneer-10 in its encounter with Jupiter in December 1973, there were experiments which measured both Jupiter's magnetic field and the relativistic electron component. Ted Northrop and I have performed a calculation, based upon these Pioneer-10 results, of the synchrontron radiation emitted at 10.4 cm (2900 MHz). Our purpose was to see whether the Pioneer-10 results corroborated what the radio astronomers have been observing for the last decade and a half.

The calculation is a very straightforward one.

$$\text{Emissivity} = \int_{-1}^{+1} d(\cos\lambda) \int_{0}^{\infty} dE\, n(E, \lambda, L)\, P\Big(f, \theta, E, \lambda, B(L)\Big) \quad (1)$$

$$n(E, \lambda, L) = \frac{1}{C} \frac{dj(E, \lambda, L)}{dE\, d\Omega} \quad (2)$$

$$j(>E, L) = \int_{E}^{\infty} dE^1 \int d\Omega^1 \frac{dj(E^1, \lambda^1, L)}{dE^1\, d\Omega^1} \quad (3)$$

We first of all consider only the radiation emitted from Jupiter's magnetic equatorial plane. In order to compute this radiation, we perform the folding integral indicated in equation 1. P is the radiation emitted at a frequency f in a direction θ with respect to the background magnetic field by a single electron which has energy E and pitch angle λ. This electron is assumed to be at a position L (in units of R_J) from the center of the planet. B is the magnitude

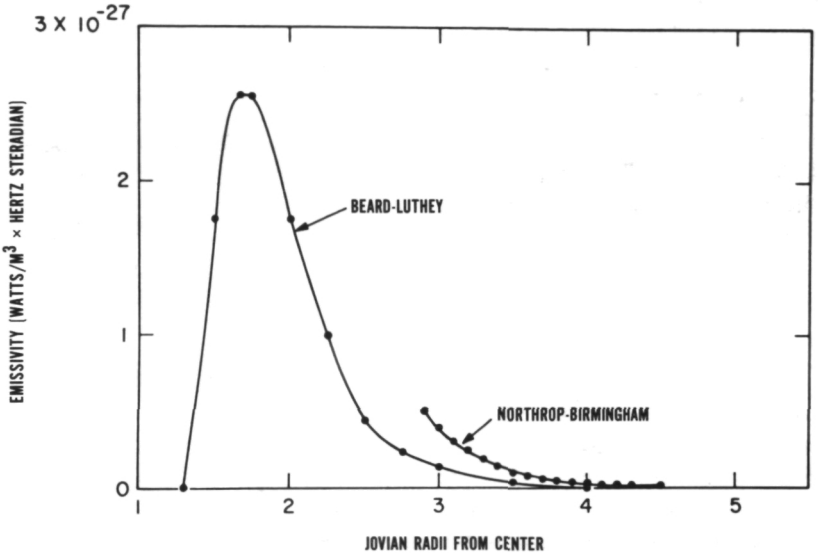

Figure 1. Synchrotron radiation from Jupiter estimated before Pioneer-10 encounter (Beard-Luthey) and calculated from Pioneer-10 electron fluxes (Northrop-Birmingham).

This curve is based solely upon ground-based radio astronomy observations at 10.4 cm made by Berge plus an assumed model of the electron pitch angle distribution in Jupiter's magnetosphere.

Over the range from about L = 2.9 to 3.5, we are roughly a factor of two higher than the Beard and Luthey calculation. This discrepancy could be reduced to approximately 30 percent, depending on where you are in L, if we were to correct for the fact that Beard and Luthey actually made a rather poor guess as to the electron pitch angle distribution in Jupiter's magnetosphere. Pioneer-10 results indicate that the pitch angle distribution is much more highly peaked toward 90° pitch angles than Beard and Luthey had anticipated. We consider agreement to within 30 percent to be excellent, considering approximations and assumptions that have gone into both of these results.

Table 1 presents what we have found to be the relative contributions of electrons in different energy intervals to the total emission at 10.4 cm as a function of L. As one moves toward smaller L values and hence into the stronger magnetic field closer to the surface of Jupiter, the major contribution shifts to lower energies. This shift is simply a manifestation of the

of the magnetic field at the position of the radiating electron. P is folded in with n, which is a phase space density of the electrons. It is n which we relate to the Pioneer-10 observations. In particular, we use the observations of electrons by Van Allen and his collaborators at the University of Iowa.

In general, n is related to the flux of electrons *differential* in both energy and solid angle. The Pioneer-10 observations of the Iowa group, however, measure the omnidirectional flux of electrons *above certain energy thresholds*. In other words, the Van Allen experiment measures the quantity in equation 3 for different values of E, the lower limit of integration. In particular, we have used their data for E of 5 MeV, 21 MeV, and 31 MeV.

In order to obtain the differential flux and hence the phase space density which we have to fold into our calculation, it is then further assumed that the differential flux is power law in energy and also power law in sin 2. The free parameters, N, Γ, and m, are then varied until optimum agreement between Van Allen's integral fluxes and the calculated fluxes are obtained for both the inbound and outbound legs of Jupiter encounter. Listed below are typical values of the parameters which have been found to be optimum at L values of interest for the synchrotron radiation emission.

$$\frac{dj(E, \lambda, L)}{dE\, d\Omega} = N(L)\, E^{-[\Gamma(L)+1]} \sin \lambda^{m(L)}$$

$$\Gamma(L = 3) = 1.9$$

$$m(L = 3) = 9.5$$

$$N(L = 3) = 4.3 \times 10^{13}\ m^{-2}\ s^{-1}$$

Note that m is quite large, which means that the electron pitch angle distribution is strongly peaked toward 90° pitch angles.

The principal result of our calculation is indicated in figure 1. Plotted as a function of distance from the center of Jupiter is the synchrotron radiation emitted per unit volume of Jovian magnetosphere. Both of the curves take into account only that component of the radiation which is polarized in the magnetic equatorial plane. This polarization is, however, the dominant component. The Northrop-Birmingham curve is based on the Pioneer-10 observations; hence, it is cut off at a value of 2.9, corresponding to the closest approach of Pioneer-10. The Beard-Luthey curve, with which we wish to compare our calculation, was presented prior to the Pioneer-10 encounter.

Table 1
The Percent Contribution of Various Electron Energy Ranges to Total Radiation

E (MeV) / L	2.5 to 10 MeV	10 to 20 MeV	20 to 30 MeV	30 to 40 MeV	40 to 50 MeV	50 to 60 MeV	60 to 70 MeV	70 to 80 MeV
2.9	0.01	13.6	32.6	22.0	12.2	6.9	4.1	2.6
3.5	0.00	2.0	18.4	23.6	17.6	11.7	7.7	5.2
4.0	0.00	0.3	8.5	19.7	19.2	14.6	10.3	7.2
5.0	0.00	0.0	0.8	7.3	14.8	16.3	14.1	11.2

fact that in a stronger magnetic field, a weaker energy electron can radiate effectively. You can see that the typical electrons which contribute dominantly to the spectrums at 10.4 cm have an energy of 10 to 30 MeV.

JUPITER'S LOW FREQUENCY RADIO SPECTRUM

Larry W. Brown

In a recent paper, I reported the detection of radio emission from the planet Jupiter near 1 MHz. This emission was identified from the Interplanetary Monitoring Platform-6 (IMP-6) data through the phase of the observed modulated signal detected from the spinning dipole antenna.

The detection of the Jovian emission has now been extended to 25 frequencies between 425 kHz and 9.9 MHz. Approximately 500 days of data covering the period of April 1971 to October 1972 have been scanned for Jupiter emission, with the positive recognition of 382 events.

An event is defined as a 5-minute interval of time containing a positive detection of emission from Jupiter. Criteria for positive detection require simultaneous detection at four semicontiguous frequencies. No Jupiter-related mission was positively observed below 425 kHz.

It is the purpose of this paper to report the spectral character of these events. Due to its sporadic nature, the spectral characteristics of the Jovian emission must be discussed in terms of the statistical behavior of the varying intensity over an arbitrarily chosen time interval. For simplicity, the intensity of an event has been taken as the peak flux density in the 5-minute interval of activity which defines the event. In principle, a spectrum of each event could be constructed and examined for various characteristics. In this respect, the IMP-6 is unique, in that simultaneous measurements of the absolute intensity can be made with fixed frequency receivers with enough resolution to produce a static intensity spectrum for each separate event.

Most of the spectral details discussed here will come from the higher intensity, longer lived bursts, as they are more readily identified and, in general, cover a larger range of frequencies. With this in mind, a composite spectrum of the emission was produced. We have plotted in figure 1 the peak flux density in watts per meter squared per hertz as a function of frequency, with the low frequencies at the left and high frequency at the right. The composite Jupiter spectrum turns out to be complex in the satellite frequency range. There appear to be at least three sources of emission. At frequencies above 2 MHz, the average peak flux density fits well with an earth-observed spectrum constructed in a similar manner. A second source appears to

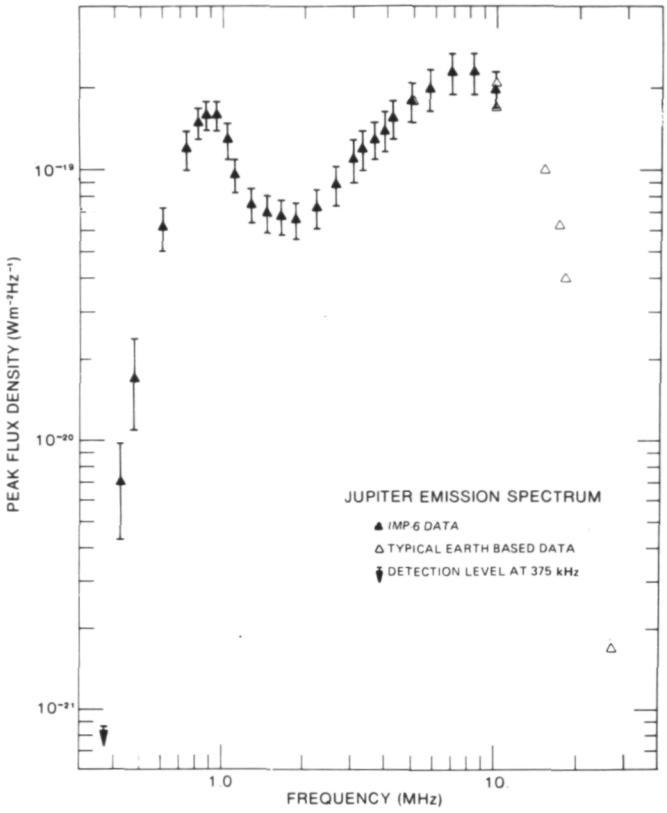

Figure 1. Composite spectrum of Jupiter emission.

dominate the emission at lower frequencies, causing the observed intensities to show a secondary spectral peak near 900 kHz.

An examination of the spectral behavior of individual events will allow a classification of these sources. In figure 2, events occurring on July 13, 1972, between the hours of 10 and 12 UT, illustrate the behavior of the two sources. Within the first hour, the spectrum resembles the composite spectrum with a secondary peak at 1100 kHz. However, in the next hour, the emission peak has disappeared, leaving a smoothly declining intensity. This satellite-observed spectrum is simply an extension of the familiar decametric bursts observed with earth-based instruments. For the purpose of this paper, such bursts have been characterized as normal events.

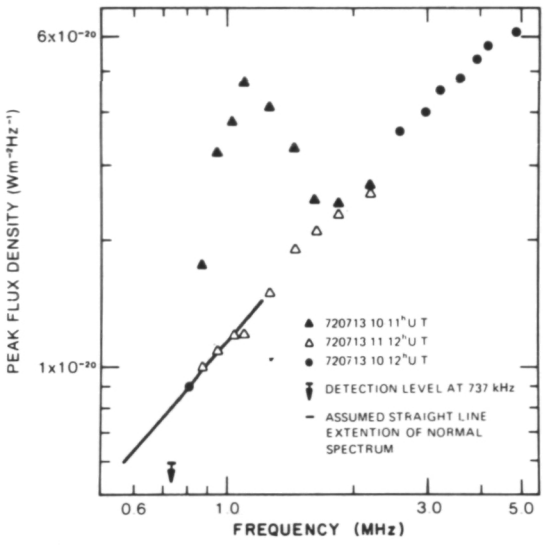

Figure 2. Typical weak burst showing the midfrequency source (▲) and the normal spectral behavior (Δ).

The second source of emission can be seen clearly in figure 3. The radiation is apparently emitted only over a narrow range of frequencies, with a definite peak and a sharp low and high frequency cutoff. The emission is independent of the normal Jupiter event, and there is no apparent correlation between its appearance or intensity with the normal spectrum. This type of spectrum is observed singly about as often as its complex combination with the normal spectrum. The second source behaves in an identical manner to the midfrequency source of earth noise, also identified in the IMP-6 data, and, as such, will be referred to as the Jupiter MF source.

The earth MF source spectrum, on the average, peaks near 250 kHz, with a sharp band pass of 200 kHz. In contrast, the typical Jovian MF emission has a spectral peak near 900 kHz and a wide band pass of 450 kHz. The direction-finding technique has been applied to the earth MF source. The radiation appears to be concentrated near the polar region of the earth and the area of emission is substantial, approximately 3 earth radii. The location and size are suggestive of an origin for the emission in particle precipitation into the cusp and/or the auroral regions of the earth's magnetosphere.

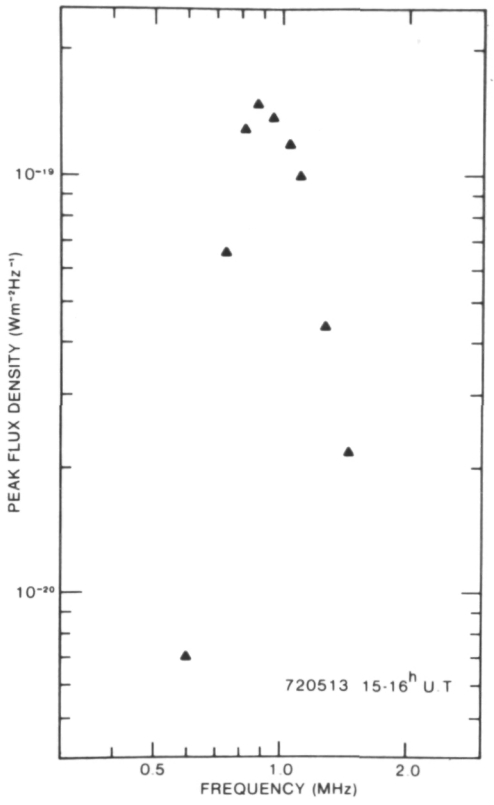

Figure 3. Typical midfrequency source emission without presence of normal spectrum.

The similarities in behavior would suggest that the Jupiter MF source might be located near the cusp or auroral regions of Jupiter's magnetosphere. In that case, the difference in the frequency of the emission peak is probably directly related to the difference in magnetic field strength between the planets. The bandwidth difference would suggest a larger emission region for the Jovian source.

DISCUSSION

VOICE: Can Jupiter's magnetosphere be optically thin in these wavelengths or should there be some absorption present?

BROWN: I really have not investigated that. I would assume it is probably optically thin. There is no indication of self-absorption.

VOICE: Are the earth and Jupiter comparable at those wavelengths?

BROWN: It is the kind of subject which you cannot approach very well statistically, since the variation is quite high. Typically I would say that of the MF sources of the two planets, the Jovian is probably a factor of 2 or 3 higher, but certainly of the same order of magnitude.

LATE RESULTS FROM THE PIONEER-11 FLYBY

Bonnard J. Teegarden

This paper presents the preliminary results from the Goddard-University of New Hampshire cosmic-ray experiment during the recent Pioneer-11 encounter with Jupiter. Before continuing, however, I would like to say a few words about the other Goddard experiment on Pioneer-10, the flux-gate magnetometer.

This experiment performed flawlessly throughout the encounter, and it observed a maximum magnetic field strength of 1.2 gauss just prior to occultation. A preliminary spherical harmonic analysis has been performed, and it indicates that the simple offset dipole model is only a fair representation of the field. Inside 2 to 3 Jovian radii, higher order harmonic terms are necessary to fit the field.

This encounter was viewed with some apprehension because, during the Pioneer-10 encounter, an integrated radiation dose of $\sim 5 \times 10^5$ rads was received by the spacecraft—approximately 1000 times the lethal dose. The Pioneer-11 trajectory carried the spacecraft even closer to the planet (1.6 Jovian radii) than did Pioneer-10 (2.8 Jovian radii). The Pioneer-11 trajectory was, however, at a much higher latitude than Pioneer-10. As a result, the total radiation dose in Pioneer-11 turned out to be less than that on Pioneer-10.

The upper panel of figure 1 shows the Pioneer-10 and -11 trajectories in the ecliptic plane. The two trajectories are clearly quite different, with Pioneer-10 being prograde and Pioneer-11, retrograde. Pioneer-10 enters near the subsolar point and exits near the dawn meridian. Pioneer-11 enters at $\sim 45^\circ$ to the sun-Jupiter line and exits nearly in the sunward direction.

In the lower panel of figure 1, the Jovimagnetic latitudes of Pioneer-10 and -11 are shown as a function of time (G. D. Mead and R. E. Sweeney, private communication, 1974). The traces for Pioneer-10 and -11 are rather similar on the inbound pass. The characteristic 10-hour periodicity due to the tilt of Jupiter's dipole is, of course, evident in both trajectories. Near perijove, however, the Pioneer-11 trajectory undergoes a very rapid change in latitude so that very little time is spent near the magnetic equator. On the outbound

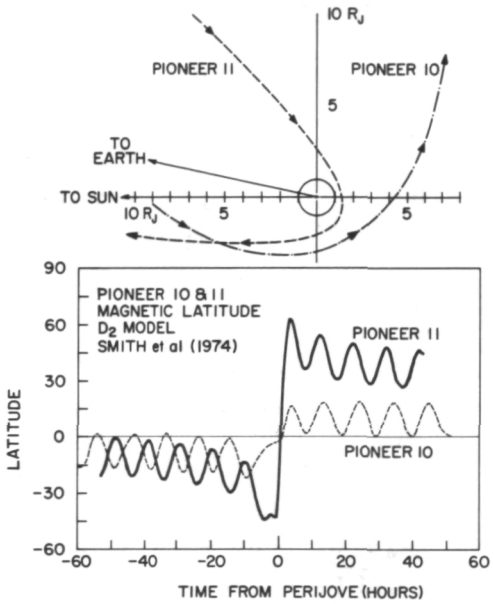

Figure 1. Trajectories and Jovimagnetic latitudes of Pioneers-10 and -11.

pass, Pioneer-11 attains a maximum Jovimagnetic latitude of ~60° and is typically in the 30° to 50° range until it passes well outside of the trapped radiation region. Pioneer-10, on the other hand, oscillates between 0° and ~ 20° latitude on the outbound pass.

The upper panel of figure 2 shows the history of the electron flux during the encounter in two energy bands. Two proton bands are plotted in the lower panel. The first, temporary increase in the electron flux (~ 98 R_J) corresponded to two successive magnetopause crossings as recorded by the plasma experiment. Whether this is a flapping of a thin magnetodisk or a compression of the entire magnetosphere due to an enhanced solar wind stream is subject to debate at this point. What seems clear, though, is that this is a very unstable region. It can be moved and deformed very easily.

According to the plasma instrument and magnetometer, we are essentially in interplanetary space again until we reach 65 Jovian radii where we again cross the magnetopause. The particles again show a steep increase at the second magnetopause crossing, and apparently we then enter a quasi-trapping region inside of 65 Jovian radii.

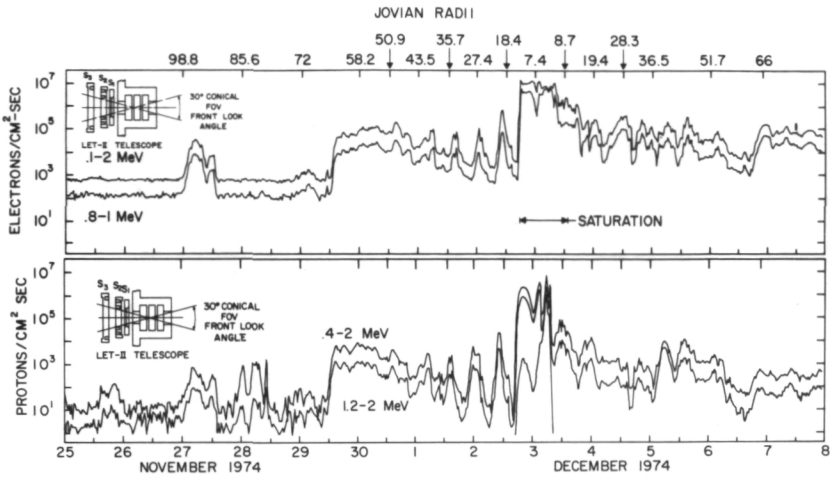

Figure 2. Electron and proton fluxes during Jupiter encounter in different energy bands.

A fairly disordered, chaotic behavior exists until we get into roughly 40 Jovian radii, and then the 10-hour periodicity due to the variation in the location of the spacecraft with respect to Jupiter's magnetic equator becomes quite pronounced. Within about 20 Jovian radii, we have quite dramatic variations in the intensity, well correlated with the appearance of minimum magnetic latitude. In fact, the last variation before periapsis is more than five orders of magnitude from peak to valley. In figure 3, the Pioneer-10 and -11 time histories for 1.2- to 2.1- and 14.8- to 21.2-MeV protons are compared during the period near periapsis. The data are plotted as a function of the magnetic L parameter derived from the Smith D2 model. There is a very dramatic dip on Pioneer-11 at Io, roughly a factor of 100, somewhat larger than the dip that was seen on Pioneer-10. It is important to note that Pioneer-11 was at a much higher magnetic latitude at this point than Pioneer-10. Hess et al.* have predicted that, in fact, at higher latitudes one expects to see a stronger depletion of particles due to the presence of Io.

It is curious that prior to crossing the orbit of Io, there is not a great deal of difference between the fluxes on Pioneer-10 and -11 as would be expected because of the difference in latitudes. One possibility is that perhaps things have changed in the year between the Pioneer-10 and -11 encounters. Other information which we have yet to analyze (pitch angle distributions, for example) should shed some light on this question.

* W. H. Hess, P. J. Birmingham, and G. D. Mead, "Absorption of Trapped Particles by Jupiter's Moons," *J. Geophys. Res.*, **79**, 1974, p. 2877.

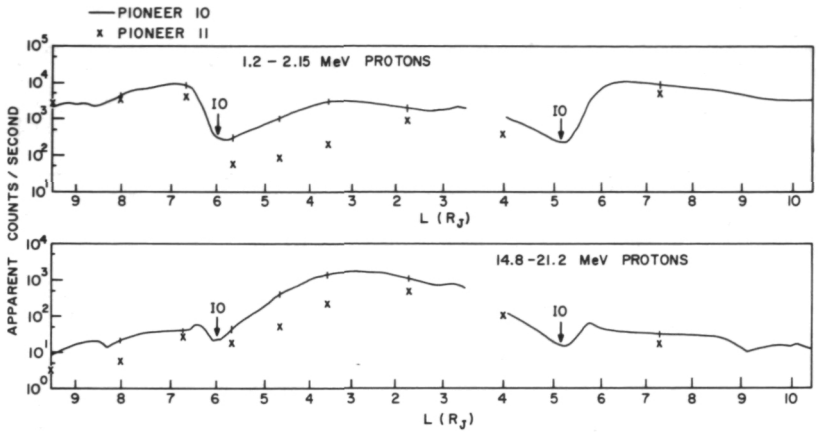

Figure 3. Pioneer-10 and -11 proton time histories during period near periapsis.

It is curious that prior to crossing the orbit of Io, there is not a great deal of difference between the fluxes on Pioneer-10 and -11 as would be expected because of the difference in latitudes. One possibility is that perhaps things have changed in the year between the Pioneer-10 and -11 encounters. Other information which we have yet to analyze (pitch angle distributions, for example) should shed some light on this question.

The latitude difference is apparently present inside the orbit of Io as we go through periapsis. On the outbound leg, the fluxes again appear to be rather close to each other, which is curious in view of the rather large latitude difference between the two.

Finally, a word about the future of Pioneer-11. Tentatively, it is being targeted for the gap between the innermost ring of Saturn and its surface, a space roughly one-tenth of a Saturn radius across. It then appears that what has already been an extremely exciting mission still holds a great deal in store.

DISCUSSION

VOICE: What did the proton flux do during periapsis?

TEEGARDEN: As you know, it went through roughly a 40-minute occultation during periapsis. Our data itself does not provide a lot of information.

I have heard that the University of Chicago instrument saw a very large but short-lived burst of protons at greater than 30 MeV, which was roughly 40 times the peak intensity of Pioneer-10. I do not know what that means in terms of the integrated dose of radiation yet Those calculations have not been performed, but I think that the fact that we have survived argues that when you integrate the radiation over time, it is going to come out less than Pioneer-10.

TIME AND ENSEMBLE AVERAGE THEORIES FOR COSMIC-RAY PROPAGATION

Alexander J. Klimas

We shall discuss theories for the propagation of cosmic rays in a turbulent magnetic field. We are interested primarily in constructing the appropriate equations which describe this propagation. I shall discuss the work performed jointly by Dr. Goldstein and myself at GSFC and by Dr. Saudri at Princeton, New Jersey.

To begin, consider this simple statement: The cosmic-ray distribution function is isotropic. Typically, we learn that fact by putting a detector into space, turning it on at some time, and beginning a collection of a number of particles. After collecting a significant number of particles, we can determine that they seem to be coming from all directions in space. Thus we conclude that the distribution function is isotropic, but this is incorrect. In fact, it is the time average of the distribution function which is isotropic. The time-averaged distribution function is isotropic because of the turbulent magnetic fields through which the particles move. However, the approach to this problem taken by theorists to discover the mechanism for this isotropization does not involve the time-averaged distribution function at all. Normally, many systems of particles are imagined, each in its own representation of the magnetic field. With this ensemble of magnetic fields, appropriate field-ensemble averages of the particles or of the magnetic fields are taken. The ergodic assumption is made; that is, it is assumed that the field-ensemble averages are equivalent to the actual time averages of the observation. This assumption is essentially unchecked; it has never been studied.

We at Goddard have begun to realize that this assumption almost certainly fails for low energy cosmic rays. We are getting around this problem by constructing a theory which deals directly with the time-averaged cosmic-ray data and the time-averaged magnetic-field data. The theory is based on a multiple time scale extension which gives the evolution of the distribution function on many different time scales. The fastest time scale of evolution is averaged, leaving the slow evolution of the time-averaged distribution function.

We have many applications in mind for this theory. The most direct and obvious here at Goddard is the traditional cosmic-ray astronomy problem.

I think most of you are familiar with that problem; therefore, I shall discuss a few other applications which may not be that familiar: particle-wave interaction in turbulent plasma and particle collisions in strong magnetic fields.

Consider the components of a turbulent plasma which may be found in a variety of places. There are many charged particles moving in a very complicated fashion, even in a simple field. But this is a turbulent plasma which contains a complicated electromagnetic field; the motion of the particles is very hard to describe. These particles keep bumping each other; that is, we have particle-particle collisions. In addition, what really causes difficulty is the fact that the field is created by the particles themselves in their motion in the field. The problem is highly nonlinear, and the approach to it might be to neglect the collisions between particles to simplify the problem. However, we are still left with a very difficult problem. We might take then, in this collisionless plasma, the test particle approximation in which we assume we know what the field is and try to compute the motion of the particles in that given field.

This is an extremely simple plasma that we are describing, but it is not just a theorist's toy. In fact, the cosmic-ray plasma in the planetary medium is exactly that kind of plasma. The cosmic ray-data, with a good theoretical description, is used as a stepping stone towards a kinetic theory for a turbulent plasma which then has many applications. Dr. Goldstein will be mentioning this in the following paper.

With our new time-averaged approach versus ensemble-averaged approach, we also see many applications to a wide range of problems in the general field of statistical mechanics where, indeed, the concept of ensembles and probability distribution functions are very common. Very often the averaging that should be done is really time averaging and many wide-ranging problems may depend on this approach.

STRONG TURBULENCE THEORY FOR COSMIC-RAY PROPAGATION

Melvyn Goldstein

One of the fundamental problems in plasma physics has been the development of the complete kinetic theory of plasmas in strong magnetic fields. Such a theory is essential for a complete understanding of the electrodynamic properties of many phenomena, among them the atmospheres of pulsars, acceleration mechanisms of solar flares, the structure of the solar wind, and the mechanism of cosmic-ray propagation in both the galaxy and the interplanetary medium. The same basic theory is needed in many aspects of controlled thermonuclear-fusion research. The development of such a theory is a very complex undertaking. I will describe one aspect of such a kinetic theory which Dr. Klimas and I have been developing.

For many problems in astrophysics, the complete kinetic theory is not necessary. For example, in the interaction of cosmic rays with the interplanetary medium, the gas of energetic cosmic rays is too tenuous to produce plasma instabilities. Consequently, most of the interaction consists of the hot cosmic-ray particles scattering from the turbulent magnetic fields that are embedded in the interplanetary medium.

This problem in nomenclature of kinetic theory is a "test particle" problem. It is a necessary part of any complete plasma-kinetic theory. Also, the extensive data available at Goddard from spacecraft observations of solar wind magnetic fields and plasmas along with measurements of the galactic cosmic-ray intensity can be used as aids in testing and developing such kinetic theories. And conversely, such theories are necessary for a complete understanding of these data. In developing an appropriate test particle theory, we have taken several points of view, and I will give a qualitative description of one such approach.

For some time now there has been available in the plasma literature a nonlinear theory which describes electrostatic-plasma turbulence. Although the theory is appropriate for test particle situations, it is of limited utility in astrophysical problems where magnetohydrodynamic and electromagnetic wave modes often predominate. Recently the theory has been generalized

to include electrodynamic waves*, and we are examining and developing this generalized theory as it applies to the problem of cosmic-ray propagation in magnetostatic turbulence.

There are several ways in which these nonlinear turbulence or resonance-broadening theories differ and improve upon linear analysis. This is indicated schematically in figure 1. An idealization of linear theory is that a particle's motion in a turbulent magnetic field is computed to first order as though the turbulent field were not present; that is, it executes a helical trajectory along the mean field, and then one computes the perturbations of that orbit due to the fluctuating field. The real world may be a trajectory which looks very little like the helix.

The nonlinear theory improves on this first-order description of particle motion by including, in a statistical way, the effects of the waves on the particles during an interaction. In the linear analysis, the particle will resonate with, and consequently scatter from, a wave of a unique frequency. The resonance velocity is given by a linear combination of the unique wave frequency of the electromagnetic turbulence, the Larmor frequency, and the wavelength of the electromagnetic wave:

$$V_{\text{resonance}} = (\nu \pm \Omega_{\text{Lamor}})\lambda$$

In the turbulence theory, this concept is generalized:

$$\nu \longrightarrow \nu + \delta\nu + \text{iD}$$

The unique frequency of resonance in the linear analysis becomes a spread of frequencies, where $\delta\nu$ symbolizes that frequency spread, and $\delta\nu$ and D can be larger than ν.

The interaction time in the linear analysis can be arbitrarily long, especially for particles whose pitch angles with respect to the mean field are near 90°; that is, particles whose helical trajectories are essentially circles. A turbulence or resonance-broadening theory introduces a complex quantity (iD) whose basic feature is to saturate the resonance after a finite time so that the particle is quickly scattered out of the wave region.

These nonlinear quantities ($\delta\nu$ and iD) can be quite large. Their magnitude depends on the intensity of the turbulence and the particle energy. For

*Ben-Israel, I., T. Piran, A. Eviatar, and J. Weinstock, "A Statistical Theory of Electromagnetic Waves in Turbulent Plasmas," *Astron. and Astrophys.*, in press, 1975.

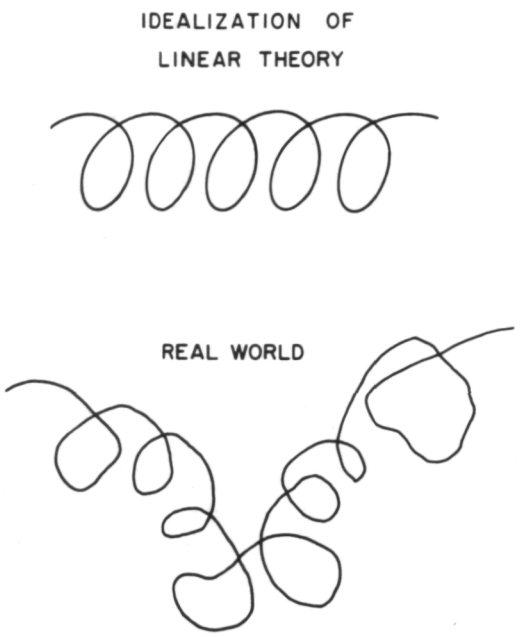

Figure 1. Schematic of actual cosmic-ray propagation turbulence in comparison to the idealization of linear theory for turbulence.

low energy cosmic rays in the solar wind, the nonlinear terms in the theory become essential and can become the dominant terms.

The theory of electromagnetic plasma turbulence provides a rigorous mathematical framework with which to describe the pitch-angle scattering of cosmic rays in magnetostatic turbulence. We have used a magnetostatic turbulence spectrum which approximates some of the features of the interplanetary magnetic field and also allows direct comparison with numerical simulations of the problem that have been developed here at Goddard (Kaiser, 1974). Some typical results are shown in figure 2 where the relative amount of pitch-angle scattering through 90° is plotted. (This is the pitch-angle scattering coefficient in appropriate dimensionless units.)

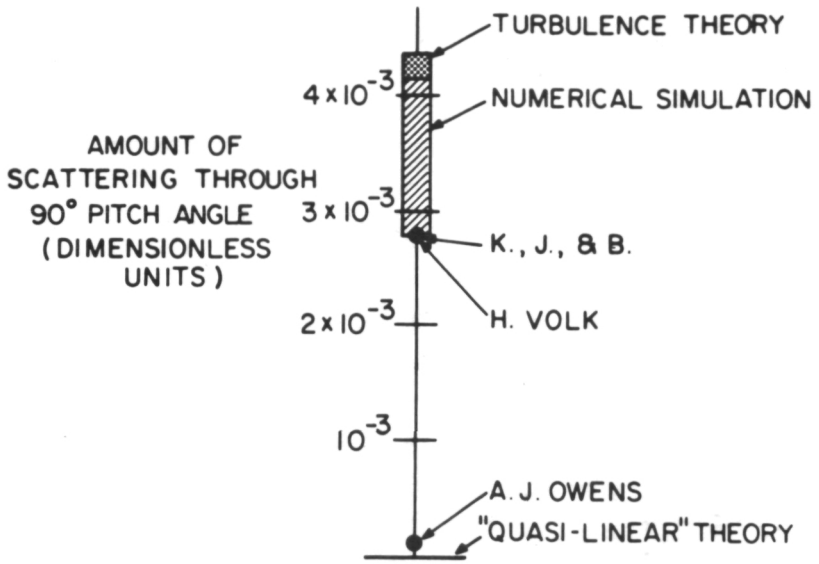

Figure 2. Typical results for moderate energies and field strengths.

The quasilinear analysis predicts an infinite time for the interaction and no scattering through 90° pitch-angle. Several other attempts have been made to improve upon the quasilinear theory. The analysis of Owens* produces essentially negligible scattering through 90°.

With this choice of parameters, the results of the theory of Völk (1973) come quite close to the numerical simulation, but if the parameters are changed slightly, the agreement becomes poor. For the range of parameters that have been explored in the simulations, only the heuristic theory developed by Jones et al. (1973) and our results are consistently close to the numerical experiments.

At lower particle energies, our results predict rather different behavior than that of the theory of Jones et al. The simulations are not yet sufficiently reliable at these lower energies to determine which analysis is more correct. For these particular parameters, both their theory and our own calculations are within the error of the numerical simulation.

The development of a good test particle theory will hopefully lead to a better theoretical understanding of many phenomena encountered in

*Owens, A.J., Ph. D. thesis, California Institute of Technology, Pasadena, 1973.

astrophysical and laboratory plasmas as well as provide a basis for progress in the development of a complete kinetic description of plasmas in strong magnetic fields.

REFERENCES

Jones, F.C., T.B. Kaiser, and T.J. Birmingham, 1973, *Phys. Rev. Lett.*, **31**, p. 485.

Kaiser, T.B., 1974, "Simulation of Pitch-Angle Diffusion of Charged Particles in a Disordered Magnetic Field," *Solar Wind Three*, C.T. Russell, ed., Inst. of Geophys. and Planetary Physics, U.C.L.A.

Völk, H.J., 1973, *Astrophys. and Space Sci.*, **25**, p. 471.

DISCUSSION

TEMKIN: How does your theory differ from that of Jones et al.?

GOLDSTEIN: The physical problem we are attacking is the same, but our analysis is different. We have followed a rather straightforward mathematical prescription to derive a pitch-angle scattering coefficient starting from the collisionless Vlasov-Boltzmann equation. It is not yet clear just how some aspects of our analysis relate to some of the very plausible, though heuristic, arguments made by Jones et al.

PARTIALLY AVERAGED FIELD THEORY OF COSMIC-RAY PROPAGATION

Frank Jones

A method was devised by Tom Birmingham, Tom Kaiser, and myself for calculating transport coefficients for particles in random-force fields that we believe represents an improvement over the older, more standard quasilinear theory.

A rather general case of particles in a random-force field is described here, but clearly what we have in mind and what we have been applying it to is the problem of cosmic rays in random magnetic fields, either in the solar system or in the galaxy. The problem in the solar system is, of course, understanding the solar modulation of galactic cosmic rays, which involves the diffusion of these particles through the mixed-up magnetic field in the solar system.

The basic formula that is arrived at through standard quasilinear theory is used. By various means, the following expression is developed for the velocity-space diffusion coefficient which is labeled D.

$$D = \int_0^\infty d\tau \, \langle F_1(Z) \, F_1(Z_0(\tau)) \rangle \qquad (1)$$

where:

$Z_0(\tau = 0) \equiv Z$,
Total force = $F_0 + F_1(Z)$,
F_0 – Steady uniform,
F_1 – Random with $\langle F_1 \rangle = 0$,
$|F_1| \ll |F_0|$, and
$Z_0(\tau)$ = Orbit due to F_0 alone.

D is given by an integral over the correlated average, and average here means ensembles where the ensemble consists of all possible random fields which have certain predetermined statistical properties.

We use (1) the correlated average of the random part of the force, which is called F_1 and is evaluated at an arbitrary point which is called Z, and (2) a moving point, which we call Z_0 where, in the quasilinear theory, Z_0 is the orbit of a particle which is moving under the influence of the steady part of the force, F_0 alone. We are simply ignoring the effects of F_1, the small fluctuating force, in calculating this orbit. We apply the boundary condition that at the time $\tau = D$, $Z_0 = Z$.

Before discussing our modification of this theory, consider the same expression for D averaged in two steps instead of taking the average over all possible fields.

$$D = \langle F_1(Z) \underbrace{\int_0^\infty d\tau \langle F_1(Z_0(\tau))\rangle_P}_{\text{impulse due to partially averaged } F_1} \rangle_F \tag{2}$$

First we do what we call a partial averaging, which I have designated with the subscript P:

$$\Delta P = \int_0^\infty d\tau \langle F_1(Z_0(\tau))\rangle_P \tag{3}$$

then we do the final averaging which is designated by the subscript F:

$$D = \langle F_1(Z)\Delta P\rangle_F \tag{4}$$

Partial averaging means taking the average over all possible force fields with a prescribed value of the field at the point Z. The force field is not allowed to vary completely at random; we hold its value fixed at this point Z, and then average over all possible fields consistent with this value at the point Z.

And if we do this, we see what the partially averaged F_1 will look like in figure 1. If it has gaussian statistics, it will simply be given by:

$$\langle F_1(Z_0)\rangle_P = F_1(Z)\, C\,(|Z - Z_0|) \qquad (5)$$

This essentially drops to zero when it is several correlation lengths away, and the correlation length is one of the statistical parameters that describes this random force field.

If it is not a gaussian process, it is going to have to look something very much like this. It is going to have to have the value F_1 at the point Z, and it is going to have to drop off to zero when you get a few correlation lengths away. It may not be exactly that function, but it is going to be similar.

The integral in equation 3, the expression for D, is simply the integral of the force field integrated with respect to time, and that is an impulse or change in momentum.

What we have done is compute the momentum change of this partially averaged force field by following the particle orbit as though that force field were not there.

This is recognized as essentially the classical Born approximation—to compute the effect of a force by following an undeviated particle orbit through it and summing the impulse on the particle. Unfortunately, like all Born approximations, it breaks down in those cases where the momentum transfer is large or, in other words, in those cases where the trajectory Z_0 is a poor approximation of the true orbit. There are certain situations where we know this is the case. When you get to this point, it can be seen how we have modified this theory.

We calculate ΔP, not by using the Born approximation and using the undeviated orbits, but by calculating the explicit orbit, including the effects of F_1 in the orbit calculation. We use this orbit in the calculation of ΔP or the impulse.

In this case, the ΔP is a much more complicated function of the value F_1 at the point Z, and so the final averaging, equation 4, can be quite difficult and very often requires numerical techniques to do because of the complexity of the functional dependence here.

However, there is one case that is amenable to a fairly straightforward, analytic approximation, and this is the case where we have particles moving in a uniform magnetic field upon which are superimposed rather small fluctuations in the form of plane waves polarized perpendicular to the uniform

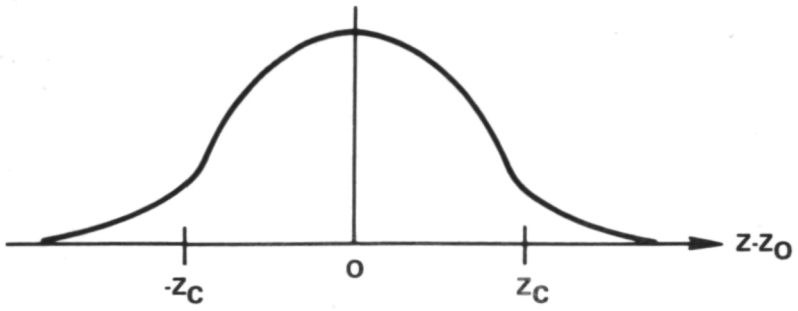

Figure 1. Partially averaged F_1.

field. This is sometimes referred to as the slab model because the perturbations are considered to be functions only of the directions along the average field, and you have these perturbation fields in big slabs.

We also tried to test this theory and determined what we could compare it to to see if we were at all on the right track. To do this we used computer simulations. In these simulations we used Monte Carlo techniques to generate random magnetic fields which we stored in the computer, an IBM 360/91. Particle orbits were then computed in these random fields.

In this way we could simulate a distribution of particles in a random magnetic field and actually follow their motion and, from this, essentially "measure" the pitch-angle diffusion coefficient. In the real sense, the diffusion coefficient is calculated, but it is very much like an experiment.

We can measure this for different values of the cosine of the pitch angle which is labeled μ in figure 2. This is the pitch angle with respect to the average field; this is just a coordinate system we use.

The diamonds in figure 2 are the measured values of the diffusion coefficient, including experimental errors; that is why they are large. There is some uncertainty in the value of μ and in the value we calculated.

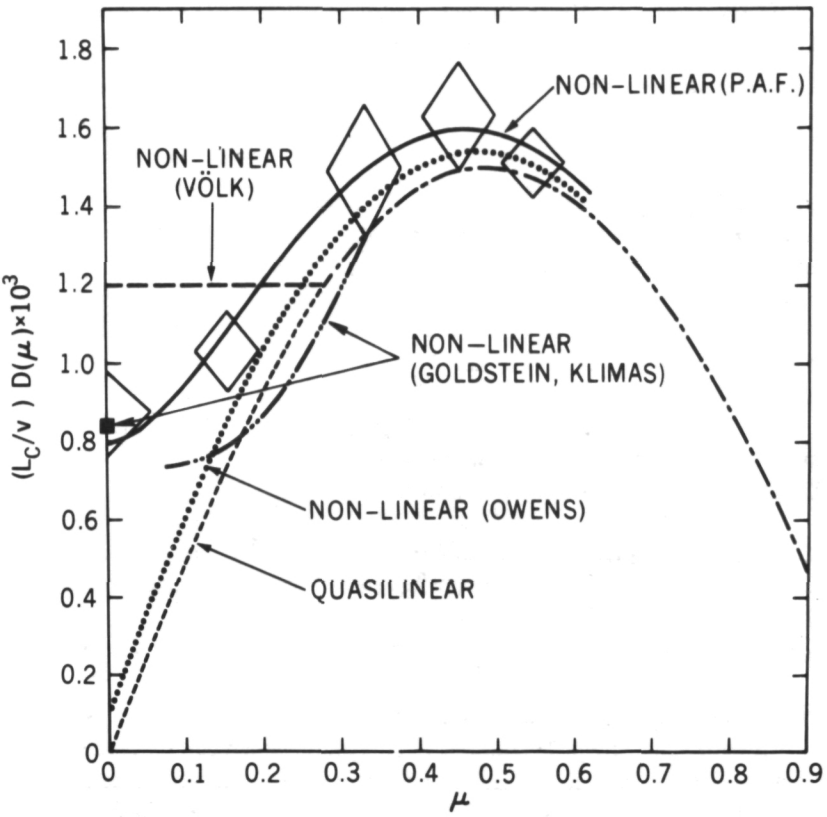

Figure 2. Various average field theories for cosmic-ray propagation.

The predictions of quasilinear theory predict for $\mu = D$ or a 90° pitch angle, essentially zero diffusion; particles very often cannot get through $\mu = D$ in this theory. Our theory, which is the solid line, and also the non-linear theories of Owens and Volk, which are based on the Dupree-Weinstock strong turbulence theory, are also plotted. The Goldstein-Klimas theory is actually a more thorough application of the strong turbulence theory and does fit the simulations in this particular case somewhat better than the others.

We believe that the approach that I have described to you today does hold promise, and we also believe that it constitutes a significant advance over the previous approaches that have been used on this problem.

THE ISOTOPIC COMPOSITION OF BERYLLIUM AND THE AGE OF COSMIC RAYS

Jonathan F. Ormes

For over 20 years, we have known that the light cosmic rays (Li, Be, B) are overabundant relative to their universal abundances. This leads us to the assumption that they are absent in the cosmic-ray source and that they are produced by the spallation reactions of heavier cosmic rays (primary cosmic rays from the sources like carbon and oxygen). Using the relevant interaction cross sections, one determines that the cosmic rays must have passed through about 5 g/cm^2 of matter. Since the cosmic rays are all highly relativistic (have velocity equal to the velocity of light), one can then find the time they spend in the galactic medium if one knows its density. The relationship is: $X = \zeta ct$. Assuming the density is 1 atom/cm^3, then

$$5\ \text{g/cm}^2 = 1\ \text{atom/cm}^3 \times 1.6 \times 10^{-24}\ \text{g/atom} \times 3 \times 10^{10}\ \text{cm/s} \times 3 \times 10^{7}\ \text{s/year} \times t$$

and $t = 3.5 \cdot 10^6$ years.

Among these light nuclei there is a radioactive isotope, ^{10}Be, which decays to ^{10}B with a half-life of $(1.5 \pm 0.3) \times 10^6$ years, which can be used as a clock to measure cosmic-ray age. For example, the Be/B ratio depends upon the fraction of Be that has decayed. This method is not sensitive enough to yield definitive results.

A more sensitive method is to look at the detailed isotopic composition of Be itself. This is an exceedingly difficult task. The Be is rare and so large area detectors must be built. The separation of isotopes is exceedingly difficult and requires accuracies of better than 1 percent. We have attempted to do this measurement using a balloon-borne payload which was launched in Canada in August 1974. The experiment uses multiple energy loss measurements to determine the velocity of a particle. This information is then combined with a range measurement to determine the particle's mass.

$$R_{A,Z}(\beta) = \frac{A}{Z^2} R_{1,1}(\beta)$$

Assuming perfect knowledge of range, the ionization loss rate must be determined to 0.5 to 1 percent for clear separation of ^{9}Be from ^{10}Be.

The instrument is shown in figure 1. It consists of a charge-determining section, S1 and S2, and a Cerenkov detector, a spark chamber for determining the track of the particle through the instrument, and a multilayered scintillator stack in which the particles are stopped and their range is measured. The detectors have typical dimensions of 50 to 80 cm and must be mapped to be uniform to better than 1/2 percent over their whole surfaces. Thickness must be known accurately, time drifts with temperature must be corrected for, and tracks must be determined to 1/5°.

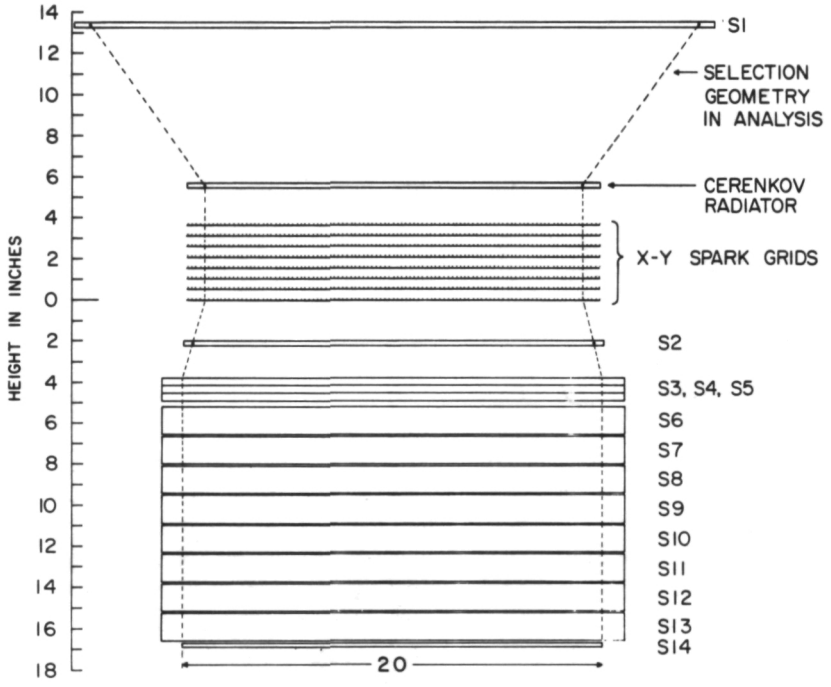

Figure 1. Isotopic detector experiment configuration.

The analysis is complex and requires an in-flight determination of the light response as a function of range. A mass histogram which results is shown in figure 2. All of the background corrections have not been made and there is some uncertainty in the mass scale. However, we can clearly separate ^{7}Be

from $^{9+10}$Be. There are about 209 ^{7}Be and 112 $^{9+10}$Be. When corrections are made to equal energy intervals, this works out to ^{7}Be/Be = 0.55 ± 0.05. This ratio supports a model in which ^{10}Be survives or in which the cosmic rays are less than a few million years old.

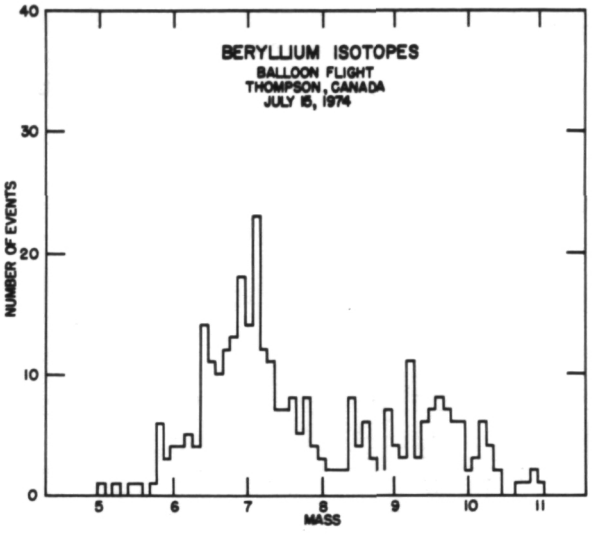

Figure 2. Beryllium isotopes, balloon flight, Thompson, Canada, July 15, 1974.

This conclusion also follows from the apparent presence of a reasonable number of particles in the histogram, 3 mass units from ^{7}Be. The statistics are better than obtained on any previous measurement, and, if we can improve the resolution in the future, we should be able to use the ^{10}Be abundance directly as a clock. At present, however, our data imply a lifetime for galactic cosmic rays of less than 3×10^{6} years and, hence, suggest that cosmic rays may reside in regions of density higher than 1 atom/cm^{3}. I think this is just the beginning of the results to come from isotropic composition measurements. As techniques improve, I expect to see rapid advances in this field over the next few years.

GALACTIC ^{2}H AND ^{3}He

Tycho von Rosenvinge

About 5 years ago there was considerable discussion concerning the possibility of distinguishing the effects of a nearby source of cosmic rays from the combined effects of more distant sources. It was thought that perhaps a nearby source could dominate at low energies while distant sources would dominate at high energies. Such two-component source models, as they were called, were, however, dropped for lack of sufficient evidence. I would now like to present new evidence for just such a model.

I will be discussing data on the isotopes of hydrogen and helium. In particular, ^{2}H and ^{3}He are thought to result from collisions of protons and ^{4}He with the ambient interstellar medium. Hence their abundances should reflect how they propagated from their source or sources to us.

The ^{2}H data shown in figure 1 were taken from the Interplanetary Monitoring Platform-7 (IMP-7) at 1 A.U. The ^{3}He data shown on the lower part of the figure were taken from Pioneer-10 as it traversed the distance from 1 to 4 A.U. The radial gradients observed by Pioneer-10, however, were small, and therefore we believe that the ^{3}He intensities observed by Pioneer-10 are, in fact, representative of those which would have been measured closer to the earth.

Note that the first two ^{2}H peaks ride on the skirts of proton peaks which are more than 50 times larger. Thus, background can be a problem, but it is less so here than it has been previously. At the highest energy, the ^{2}H peak comes beyond the proton penetration point and so background is not a problem. At the two highest energies, you can see that ^{3}He is clearly resolved, whereas, at the two lowest energies, we are only able to set upper limits.

Previously, the approach to studying ^{2}H and ^{3}He has been to study ratios with respect to ^{4}He first, because there is a tendency to reduce the unknown effects of solar modulation, and, second, because the ratio is sensitive to the shape of the source spectrum. Extensive calculations have been done for models in which sources distributed throughout the galaxy emit protons and ^{4}He with energy spectra ranging from power laws in kinetic energy to ones in total energy. These represent what are considered to be extreme possibilities.

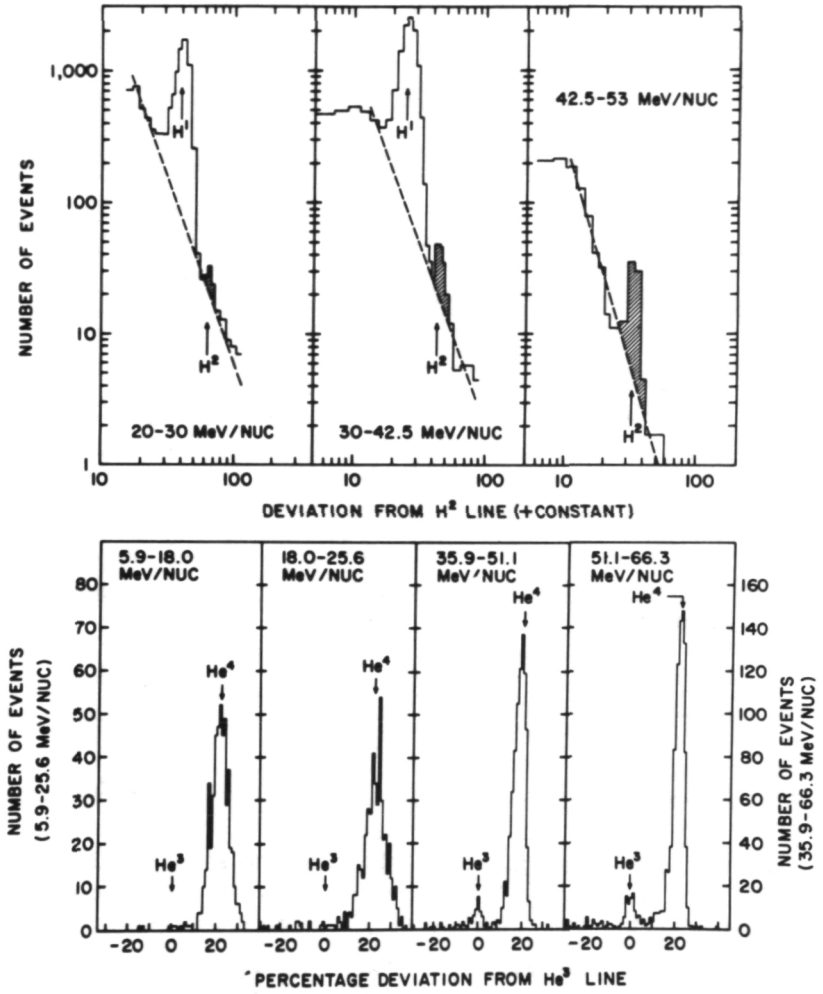

Figure 1. IMP-7 ^{2}H data (top) and Pioneer-10 ^{3}He data (bottom).

Now we will compare our observations to the calculations and will find that such models are deficient. The simplest explanation of this deficiency is that there is a nearby source of ^{4}He. In figure 2, the observed ^{2}H-to-^{4}He ratio on the left and the ^{3}He-to-^{4}He ratio on the right are plotted and compared with the calculated curves for these two extreme assumptions. Note that the calculated curves represent interstellar ratios, whereas the observed data were taken essentially at one astronomical unit. If there are no effects of solar modulation, a reasonable interpretation of these data would be that

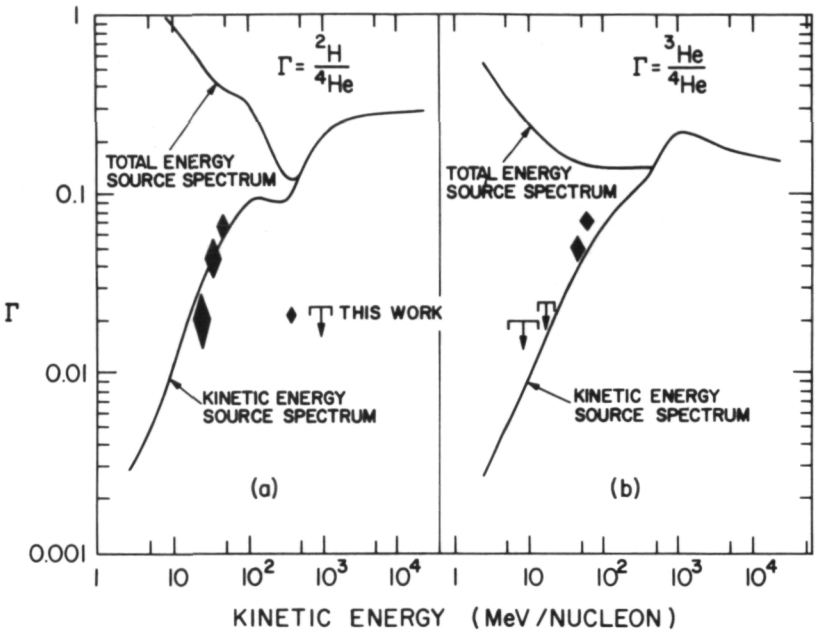

Figure 2. Observed ^{2}H-to-^{4}He and ^{3}He-to-^{4}He ratios compared with calculated curves.

these data points fall on the calculated curve for a kinetic energy source spectrum as do, very nearly, the ^{3}He data points. If, on the other hand, there is considerable solar modulation, then adiabatic deceleration will have occurred. The data points should then be shifted substantially to the right, which means that they fall below the calculated curves. In this case, since the kinetic energy source spectrum is the steepest spectum, which, for example, Dr. Smith would have allowed in his earlier talk on Copernicus results, we need to seek another explanation.

The most probable explanation is that there is a nearby source of ^{4}He. I say "nearby," because for such low ratios it means the ^{4}He is not accompanied by ^{2}H and ^{3}He, which should be present if the ^{4}He source were more distant. Thus, we need to know whether or not solar modulation is significant at the time the data were taken. There is some evidence that solar modulation was, in fact, small. In particular, total intensity levels were near those of the previous solar minimum. Radial gradients observed by Pioneer-10 were small, and the low energy ^{16}O spectrum shows a turnup which is difficult to reconcile with adiabatic deceleration. On the other hand, the shape of the low energy electron spectrum may be interpreted to imply an energy loss of at least 300 MeV per nucleon, which is not small.

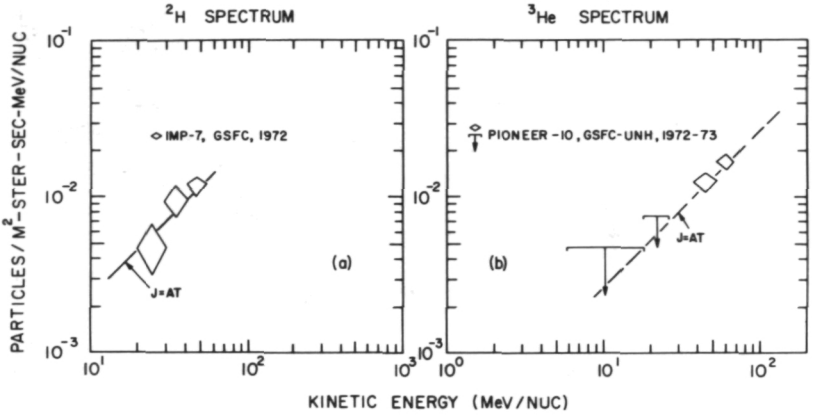

Figure 3. Observed ^{2}H and ^{3}He spectra.

To further examine this situation, the actual ^{2}H and ^{3}He spectra are shown in figure 3. You will notice that the spectra are well fit by a spectral form, J = AT, a spectrum which is proportional to energy. That is true both for the ^{2}H and for the ^{3}He.

This is precisely what you would expect if there is a large amount of solar modulation taking place. Essentially, what happens is that, if there is a lot of modulation, the low energy particles in interstellar space are unable to penetrate to the earth, and the shape of the spectrum that you see at low energies is then effectively determined by the adiabatic deceleration process. These spectra are very different from what you would expect from source spectra which are power laws in kinetic energy and little modulation.

In conclusion, the evidence is in favor of a considerable amount of modulation, and this, coupled with the very low ^{2}H-to-^{4}He and ^{3}He-to-^{4}He ratios which we have observed, implies that there must be a nearby source of low energy ^{4}He which is dominant at those low energies.

DISCUSSION

KING: Do you include the sun as a candidate source for these low energy particles?

VON ROSENVINGE: No, because we carefully select time periods free from solar activity. It is hard to speculate on what the source could be. I know that Len Fisk has some ideas about how the ^{16}O upturn originates.

He ascribes that to a process in the solar wind, and ^{4}He could also be undergoing the same process since it also has a high first ionization potential. The source could also be galactic. The true nature of the source, I really cannot say at the moment.

ELECTRON IMPACT EXCITATIONS IN HOT SOLAR PLASMAS

Aaron Temkin

I shall discuss the atomic-collision physics aspect of deducing temperature and density in the solar corona during active solar conditions, particularly solar flares. The observational data, to which the calculations I shall describe are being applied, have been taken primarily from OSO-5 and OSO-7 experiments by the Goddard group headed by Werner Neupert.

The atomic problem is to calculate the electron impact excitation cross sections of highly stripped atomic ions whose decay gives rise to the X-ray and ultraviolet lines which are observed.

The collision problem is a difficult one because the temperature of the exciting electron level in the solar corona, which ranges from 3 to 40 million K, corresponds to mean electron energies which are lower than the levels which are excited. Thus, only the electrons in the tail of the distribution can do the exciting. But since the number of such high energy electrons goes down exponentially with energy, only those electrons whose energies are near the excitation threshold itself are really effective in populating the levels in question. Nevertheless, the calculational methods from which previous results have been derived are high energy approximations. Thus, they assume that the impacting energies are large compared to excitation energies, and as I have just indicated, that is emphatically not the case. One really needs to use low energy methods, but those methods have traditionally been the difficult part of quantum theory because they require a much more complete quantum-mechanical description of the scattering process.

The main point in this paper is how our work over the years on low energy collisions has put us in a rather unique position to contribute to solving the problem.

The specific problem I would like first to discuss is electron impact ionization of atoms near threshold. This problem has application itself to line profile calculations in the chromospheres of stars where LTE conditions do not prevail. The ionization problem is also of great theoretical importance because it is the fundamental problem in which the final state consists of three separated charged particles; that is, namely the two outgoing electrons and the residual ion. This means that the forces among all pairs of particles

are long range, but at the same time, the problem is intrinsically three-body, and of course, that is what makes it so difficult to solve.

Figure 1 is an epitome of our latest work on this problem. Shown is the cross section for producing two electrons, one of energy ϵ and the other of energy k^2, such that E is the total available energy.

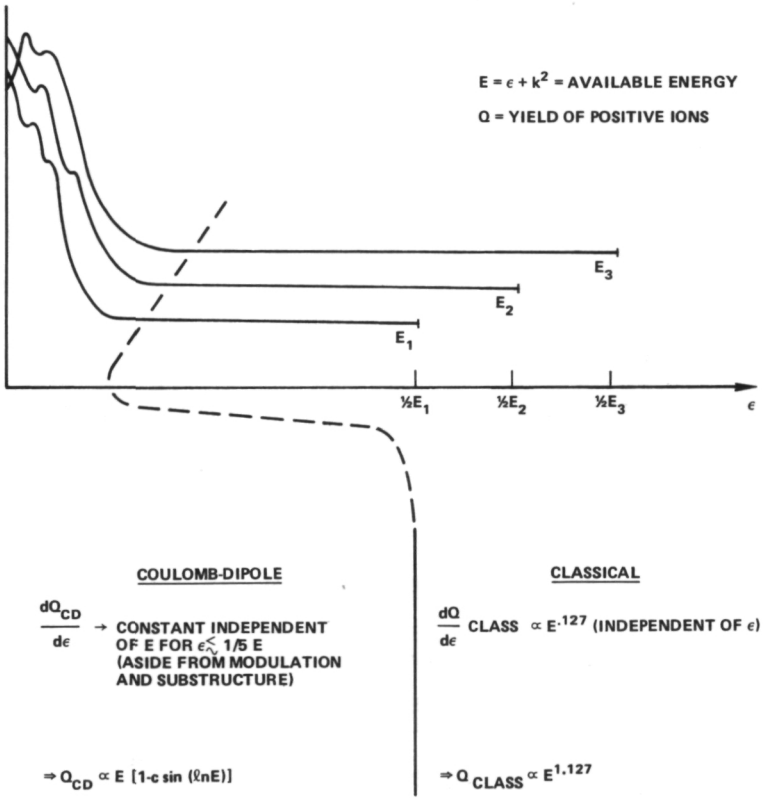

Figure 1. Electron-atom threshold ionization.

The energy of the impacting electron, which is not shown in the figure, is the available energy (E) of the two outgoing electrons plus the binding energy (I) of the originally bound electron to the residual ion: $k_i^2 = E + I$.

The curves in figure 1 are for three total available energies E_i (i = 1, 2, 3); each curve must be symmetric around its midpoint $\epsilon = E_i/2$. Thus, only the first half of each curve is shown.

The theory which is presently invoked is basically a classical theory based on Wannier (1953). The classical argument predicts that the total yield (Q) is dominated by curves which are constant, that is, independent of ϵ over the middle portion of the 1-particle energy regime. The curves are also predicted to diminish as the 0.127 power of the available energy E. The classical argument maintains that the cross section is dominated by such nearly equal energy events because, if the energies of the two outgoing electrons are too different from each other, the slower one will simply not escape because it is so strongly attracted to the residual line.

Our recent work on this problem (Temkin, 1974) shows, to the contrary, that in the unequal energy regime, quantum-mechanical effects (which are well known in the theory of photoionization and in experimentation) will cause the cross section to rise to a value independent of E as ϵ approaches zero. Our new theory essentially says that rather than being constant, or even going down, the curves go up.

Mathematically, this effect can be described by the optical potential which is the effective potential seen by the outer electron as it recedes from the residual ion, and the inner electron. This optical potential also causes the modulation in further substructure in the energy distribution curves. The net result is that the total yield, according to our theory, is dominated by the region, and that causes Q to be essentially a modulated linear function of E as opposed to the classical counterpart which is a higher power of E and, therefore, is much smaller for very small E.

With regard to the electron-ion excitation problem, the important lesson we learned is how to appreciate and calculate the optical potential. This is illustrated in figure 2. The same properties which cause the structure and modulation in figure 1 cause the inelastic cross section to be overlaid with resonances. When these resonances are averaged with the nonresonant background effects, then in the case shown, they cause an approximately 50 percent rise in the total collision strength Ωij.

The implication of this for the solar problem can be appreciated by referring to figure 3. There a comparison is given of a flare and a quiet sun spectra. The analysis to determine the temperature and densities requires knowing the rate coefficient C_{ij} which is an integral over the electron distribution function.

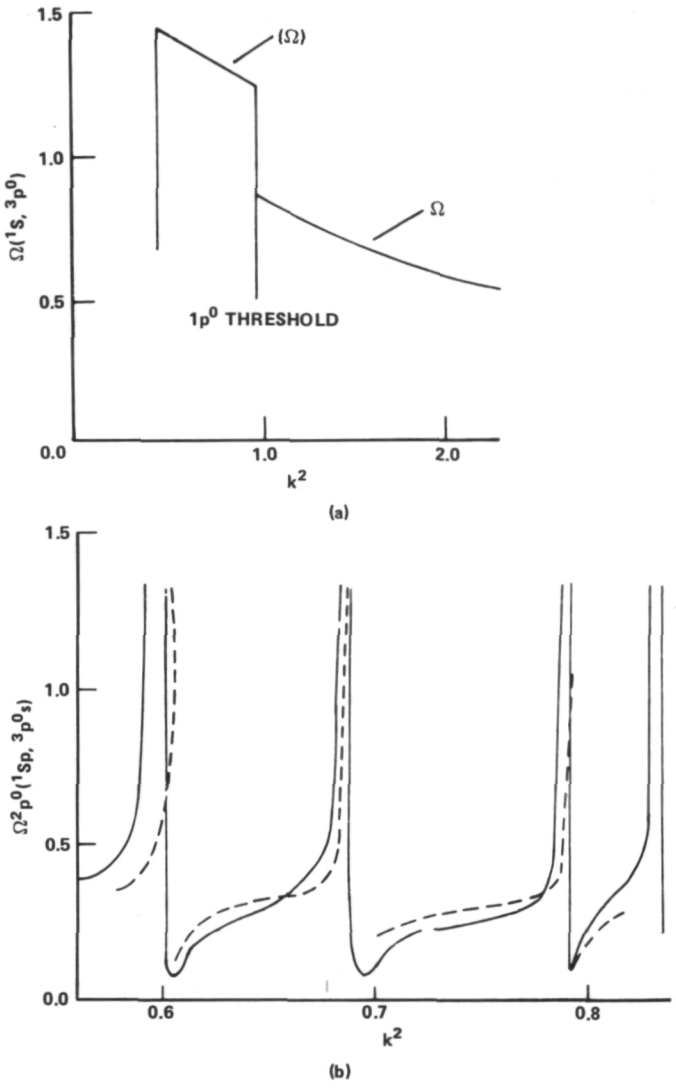

Figure 2. a. The enhancement of the average collision strength in e-CIII excitation due to resonances whose parent state is $^1P^o$. b. The individual resonances from the partial waves correspond to incoming p wave and outgoing s wave of the impacting electron. Dashed curves are distorted wave results and solid curves are the full close coupling results. Both figures from Hershkowitz and Seaton, *J. Phys. B*, **6**, 1176 (1973).

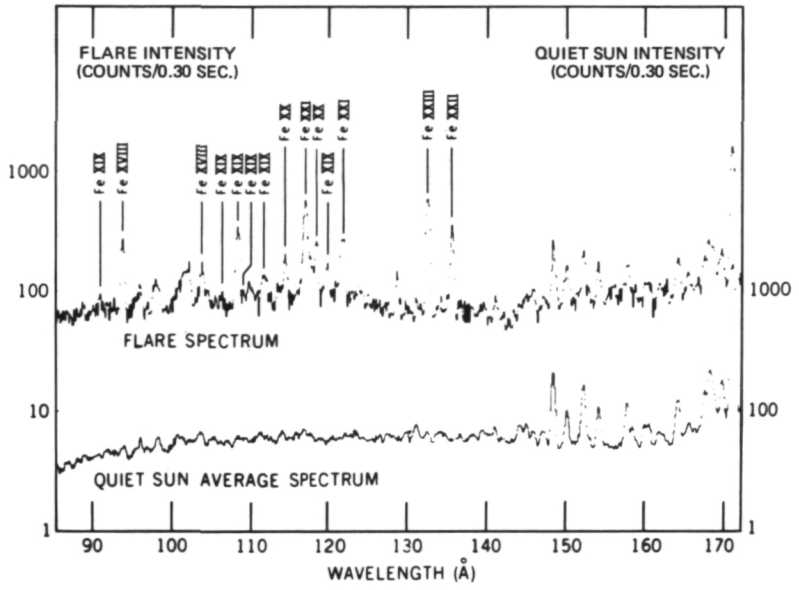

Figure 3. Comparison of flare spectrum (OSO 5) with quiet sun spectrum (from S. Kastner et al., 1974).

$$C_{ij}(T) = \int f_T(v)\, v\, Q_{ij}(v)\, dv \frac{cm^3}{s} .$$

This is the function of the temperature only if it is a Boltzmann distribution, which it is, and the inelastic cross sections (Q_{ij}). By knowing Q_{ij}, one can calculate what electron temperature (T) and what density of the various species whose lines are observed are required to give agreement with the data. But if the Q_{ij} values are wrong by approximately 50 percent, then the solar physicist will undoubtedly be led to quite erroneous conclusions about the conditions in the solar flare.

Thus our ability to know Q_{ij}, which comes down to our understanding of that somewhat theoretical-sounding optical potential, plays a vital role. A preface to the calculational approach is found in Temkin, 1974.

REFERENCES

Kastner, S., W. Neupert, and M. Swartz, *Astrophys. J.*, **191**, 1974, p. 261.

Temkin, A., *A Calculated Approach to Electron Impact Excitation of Ions in Hot Solar Plasmas*, Goddard Space Flight Center, TM X-70755, 1974.

Temkin, A., *J. Phys. B*, **17**, 1974, p. L450.

Wannier, G. H., *Phys. Rev.*, **90**, 1953, p. 817.

THE TOPSIDE IONOSPHERE AS A THREE-TEMPERATURE PLASMA

Eugene J. Maier

The upper ionosphere has traditionally been described as consisting of ions at a temperature, T_I, and electrons at a temperature, T_E, both coupled to a neutral atmosphere which is at a temperature, T_N. This paper describes our observations of deviations from thermal equilibrium of the hydrogen and oxygen ions in regions where there is a relative flow of these ions present. These results were obtained from two experiments on the International Satellite for Ionospheric Studies-2 (ISIS-2) spacecraft, operating in the geometry shown in figure 1.

In figure 1, the spacecraft is rotating clockwise as it progresses along its orbit, which is circular, concentric with the earth, and at an altitude of 1400 km. The typical high latitude field line along which we have an upward flow of hydrogen is illustrated. Then the two experiments, the ion mass spectrometer and the retarding potential analyzer, successively look radially outward from the spacecraft as it rotates. Thus, they sample first the stream flow due to the essentially static oxygen ions, then later look at lower angles.

In the inset at the bottom of the figure, you see the vector diagram where V_H is the velocity of the protons going upward along the field line, minus V_S, the apparent stream flow due to the static ions, and the summation vector which is apparent flow into the spacecraft. The ion mass spectrometer is used to measure the angle β between the spacecraft velocity and the apparent flow direction of the protons. The assumption that the flow is along the field line allows us to determine the actual magnitude of this hydrogen velocity.

This information is then analyzed in conjunction with data seen in figure 2, which is an integral ion energy spectrum obtained from the retarding potential analyzer; current, or flux, is plotted versus applied potential. The equation at the top should be noted. The measured current is equal to the hydrogen ion density times the function of the hydrogen velocity, its angle of flow, and its temperature, plus the other component of the current proportional to the oxygen density times the similar function of the oxygen velocity, its angle of approach, and its temperature.

Until now, one has traditionally analyzed these curves assuming the same temperature to obtain for all components of the plasma. In fact, what we have

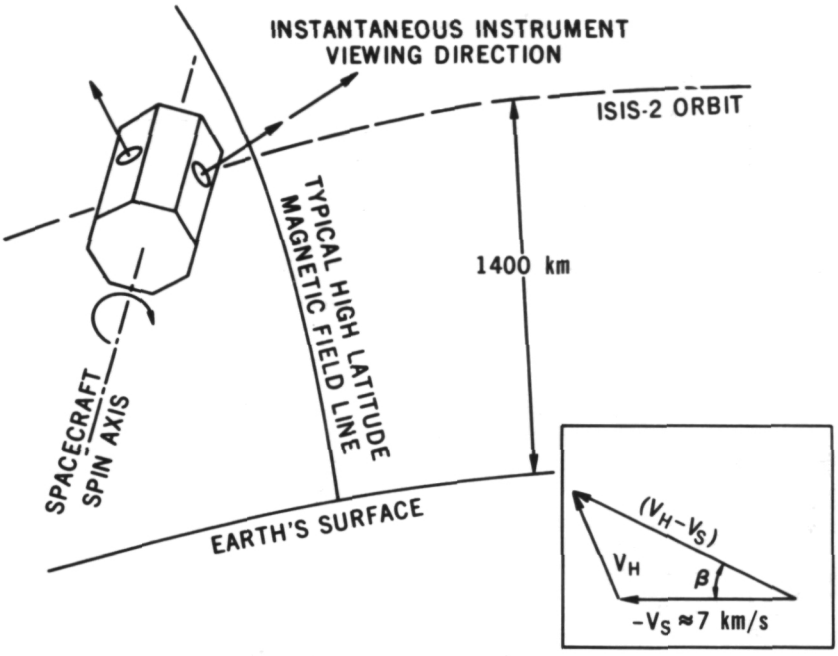

Figure 1. Geometry of the ISIS-2 observatory for flow observations.

done is a more generalized least squares fit to determine one temperature for the oxygen, another one for the hydrogen, the two densities, as well as the spacecraft potential which, of course, determines where one can begin using this curve. Because, in the spacecraft velocity frame, the translational energy of the spacecraft gives oxygen an equivalent energy of about 4 eV, the lower part of the curve yields the spectral information of the oxygen distribution function. The lower energy portion yields the information for the light ions.

The results we have obtained are summarized in figure 3—namely, we find that, in this high latitude region where the flows are present, the temperature of the hydrogen ions is about three times that of the oxygen ions. You will recall that this is at an altitude of 1400 km. By way of explanation, there are two possibilities to be mentioned.

First, I point out that it has been known that, at low altitudes, collision frequencies are very high, and that there is very likely to be thermal equilibrium between all the ion species present in the F layer. At the apex of the field lines, however, the density of oxygen is vanishingly small, so that the plasma

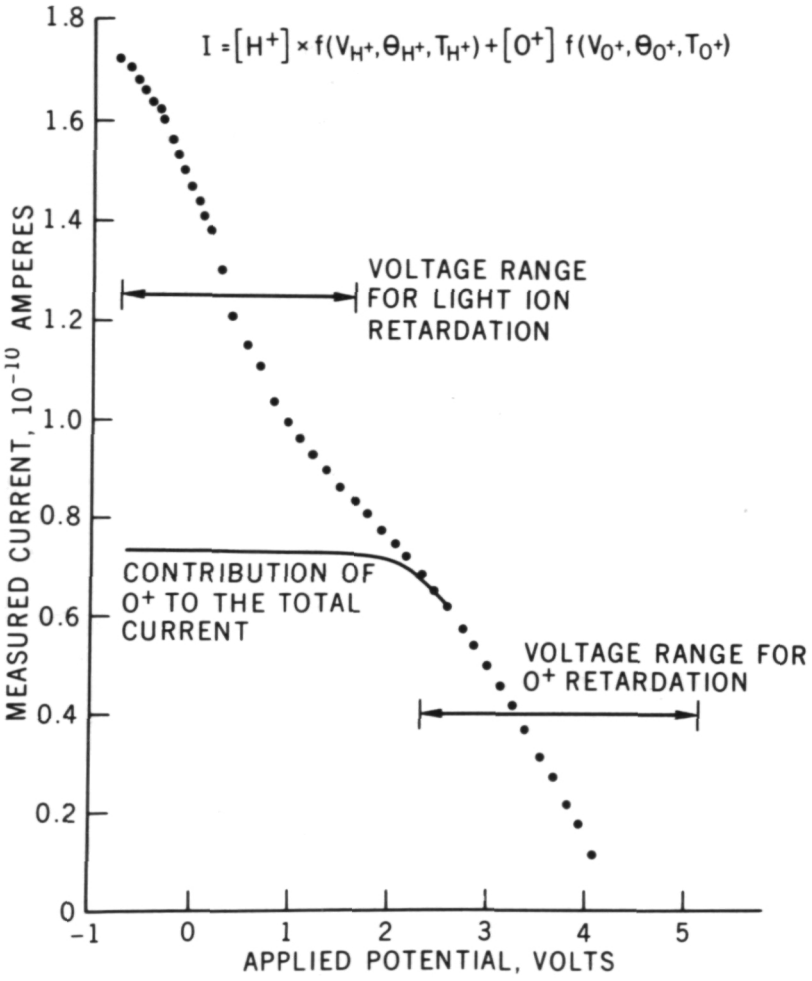

Figure 2. Retarding potential analyzer integral ion energy spectrum.

consists of essentially hydrogen at one temperature and the electrons at perhaps another temperature.

Thus, at the intermediate altitude, we have the situation where the oxygen may be representative of the lower atmosphere. The hydrogen ions present may be representative of the energy structure in the magnetosphere along a connecting field line.

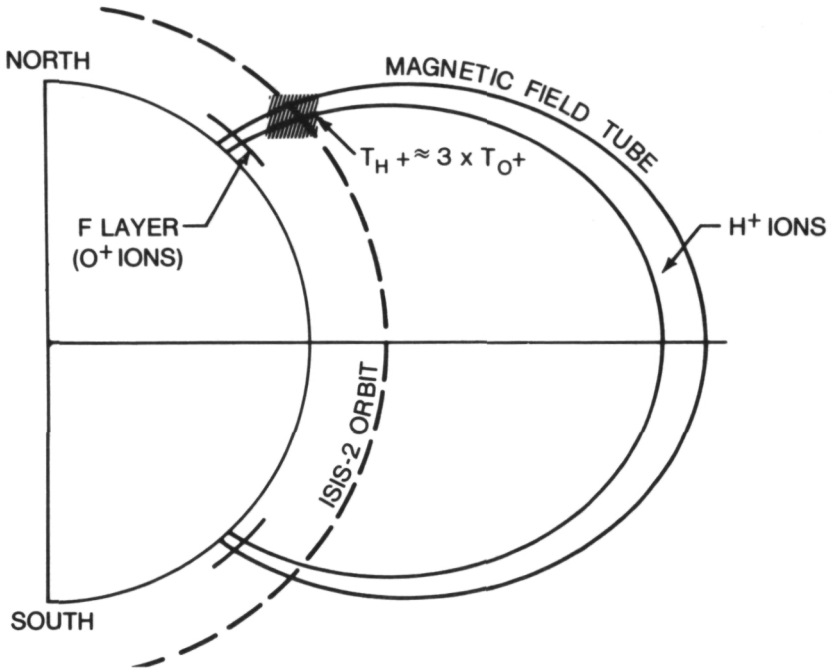

Figure 3. Schematic showing enhancement of H^+ temperature at high latitudes as a result of the H^+ outflow.

Alternatively, the ions can be energized from the protons themselves by the flow upward along the field line. These are very light ions flowing in the presence of much more massive ions. Collisions along that flow path provide a mechanism for interchanging flow energy with thermal energy, thus resulting in an enhanced temperature for the hydrogen.

DISCUSSION

VOICE: What can you say about the presence of O^{++}?

MAIER: Our instrument would not resolve it, but the ion mass spectrometer would show what is present. In fact, the reason we use only hydrogen and oxygen is that we know that those are the prime species. Helium is present sometimes and that is also allowed at the same temperature as hydrogen.

VOICE: Can you detect carbon ions?

MAIER: The carbon, I think, has probably not been observed in an ionized state at that altitude at all.

STORM TIME HEATING OF THE PLASMASPHERE

Larry H. Brace

The information presented in this paper was obtained from the International Satellite for Ionospheric Studies-2 (ISIS-2). ISIS-2 is the result of a development starting with Alouette-1 and including Alouette-2, ISIS-1, and ISIS-2. It has developed into a very good observatory for looking at the earth's atmosphere in terms of the effects of magnetospheric heating at both high and middle latitudes. This paper deals with the midlatitude heating seen during magnetic storms.

Figure 1 shows the configuration of the ISIS-2 orbit. The plasmasphere is a region of relatively high concentrations of ions and electrons of low thermal energies around 1 eV. The plasmapause is the boundary outside of which the densities fall by a factor of 100 to perhaps 1000 relative to the densities in the plasmasphere. The ring current region, with ions and electrons in the 10- to 50-keV range, lies outside the plasmapause. This is a magnetospheric feature, the source of which is not entirely understood, but we do know that there is an interaction region in which ring current energy is pumped into the low energy plasma. That energy is seen in the form of heat conducted down the field lines to the upper F region. In the ring current region we see the elevated electron and ion temperatures from the ISIS-2 satellite.

During a magnetic storm, interplanetary electric fields (solar fields) move inward into the corotating electric field and remove much of the thermal low energy plasma from the plasmasphere. Therefore, we see this region of heating moving down toward lower latitudes, and the plasmapause is marked by a falloff in an H^+ concentration that is seen when you are outside the plasmasphere.

The ring current also moves into this region where the plasma has been removed, and then, in the recovery phase, low energy plasma is formed through charge exchange down in the F region, going up the field lines, refilling the plasmasphere, and now running into this new ring current population which has formed there. This causes enhanced heating and in this recovery phase we expect to see very high electron temperatures.

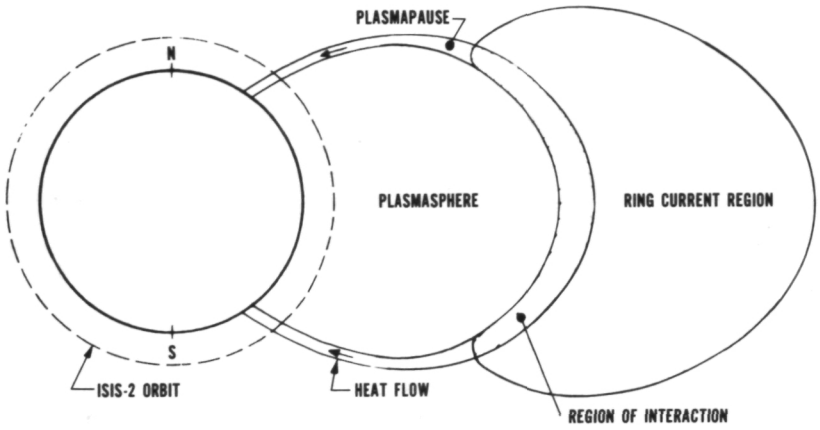

Figure 1. Configuration of the ISIS-2 orbit.

Figure 2 shows what is seen, not during disturbed times, but during the quiet time after the storm. This is a pole-to-pole pass—really two passes that did not quite connect. We measured the electron temperature, the ion temperature, and the ion concentration. The rapid rise of H^+ as we come toward the magnetic equator at about L = 2.9 represents the plasmapause; the arrow (located left of center) then represents the location of the plasmapause determined by looking at the low energy plasma. We see that there are elevated electron and ion temperatures there.

Figure 3 shows the effect we saw in the August 1972 storm. In the lower graph we have plotted K_p versus the date, August 3 through 8, 1972. The arrows and numbers indicate the times and orbits during which we were able to cross the plasmapause and see the effect of energy coming down from the magnetosphere.

I want to focus particularly on the peak shown in the top graph and the recovery that occurred during the falloff of K_p in that particular substorm. Orbits 6220, 6222, 6223, and 6224 are the important ones to follow. Electron temperature is plotted on the ordinate. The arrows indicate the position of the plasmapause during these particular passes.

In orbit 6211, the time before the storm, the temperatures are lower all over than they will be later. The plasmapause is not marked by any great enhancement of electron temperature. During orbit 6220, at the peak of K_p, the plasmapause has moved down around L = 2. The temperatures are elevated at all latitudes, not just at the plasmapause, and there is a general heating through low to high latitudes.

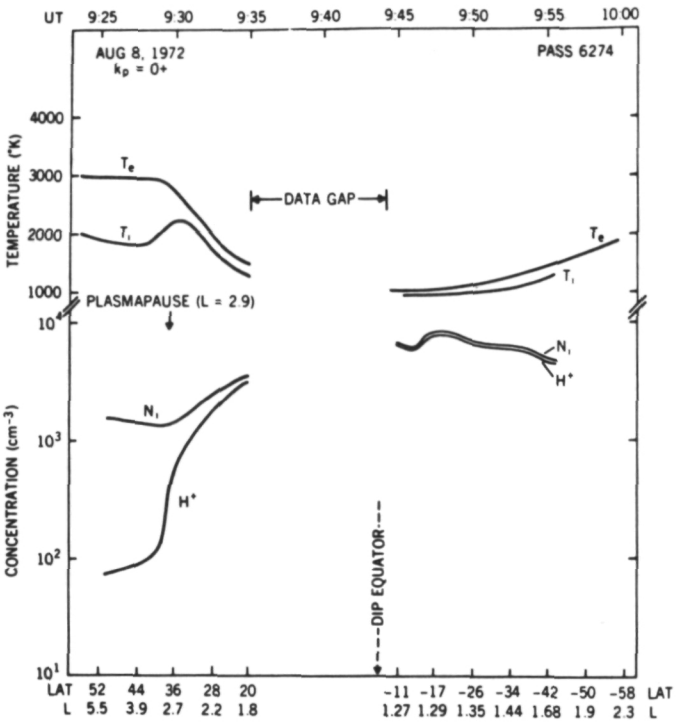

Figure 2. Heat situation in quiet time after a magnetic storm.

Orbit 6222, 4 hours later, passes through the plasmapause and finds that the hot region is enhanced, but the enhancement is over a much narrower region than before and is just outside the plasmapause. By orbits 6223 and 6224, the plasmapause has started to move outward. In other words, the plasmasphere is refilling from below. These new electrons and ions are being heated by the ring current particles, and we now see an elevated temperature over a much narrower range of latitudes. It is a very sharp peak. Looking later in the storm, we find that this peak develops into an even sharper peak, that is, with the temperature both inside and outside the plasmasphere falling; but, right at the plasmapause, there are even more sharp peaks and enhancements of electron temperature.

Thus we can see that the ISIS-2 satellite does provide a valuable platform for looking at the energy that is induced by interactions in the magnetosphere. We can determine the motion, the location of the temperature enhancements, and the range of latitudes over which they occur. But we look forward to the Electrodynamics Explorer satellite which hopefully will provide

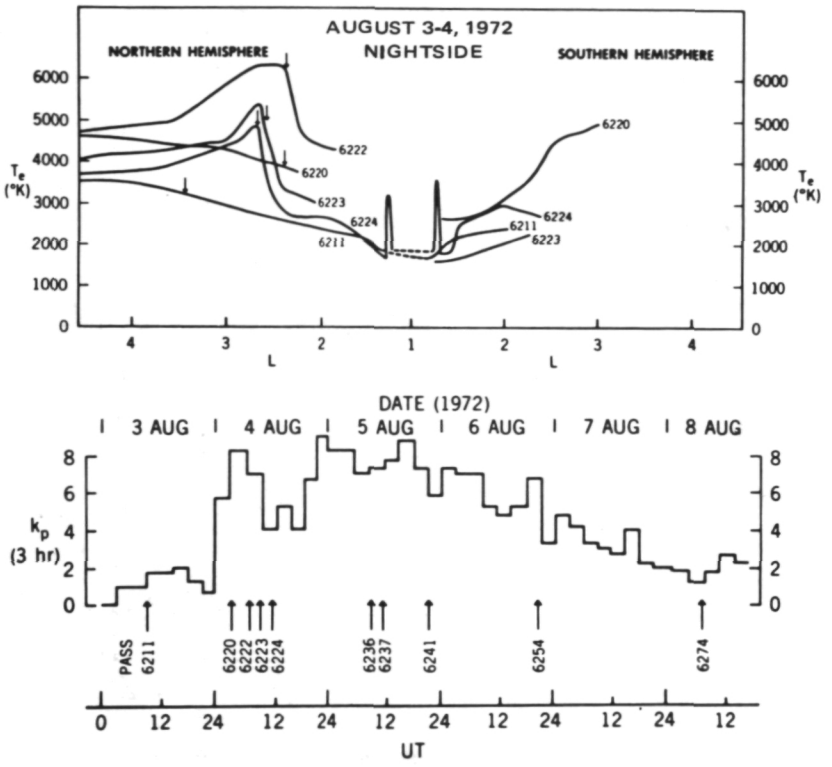

Figure 3. Heating effects seen in the magnetic storm of August 3-4, 1972, by ISIS-2.

not only a low altitude satellite to measure the effects on the atmosphere but also a high altitude satellite to measure the parameters needed to see whether this interaction takes the form of Coulomb collisions or is involved with wave-particle interactions or additional processes.

DISCUSSION

VOICE: Did you calculate the heat flowing into the ionosphere?

BRACE: Yes. That highest temperature peak was about 7500°, and that corresponds to about 10^{10} eV per square centimeter per second.

VOICE: What is the temperature of the ring current particles?

BRACE: There is a distribution of energies there, and a temperature equivalent to 50 keV, a very high temperature. I do not know how well the ring current response to a storm is understood. The fluxes probably increase, and I am not sure what the energies do.

THE SEMIANNUAL VARIATION IN THE UPPER ATMOSPHERE

Sushil Chandra

The semiannual variation or, more specifically, the equinoctial enhancement in neutral density is one of the most persistent features of the upper atmosphere. Most of the information about semiannual variation has come from the neutral density derived from the drag data, though by inference it has been assumed that similar effects are present in the thermospheric temperature. This has led to a search for possible heat sources which might heat the thermosphere preferentially during equinoctial months. In several years, it has been possible to relate the semiannual variation to an enhancement in geomagnetic or solar activity which appears to have equinoctial maxima. The semiannual variation in the atmosphere, however, appears to be much more regular than indicated by either the solar or the geomagnetic indices.

In this paper, I wish to show that the semiannual variation is primarily a density phenomenon and is a manifestation of the coupling between the upper and the lower thermosphere. In the various altitude regions, the major neutral constituents exhibit semiannual effects as a result of two competing factors: (a) the temperature in the upper thermosphere, or the so-called exospheric temperature, which is controlled by solar UV heating, and (b) the changes in the neutral composition below 120 km, which are usually out of phase with respect to exospheric temperature and which are controlled by eddy transport. The various neutral constituents, which tend to be in diffusive equilibrium above 120 km, have their phases displaced with respect to the exospheric temperature as a result of the changes in the lower thermosphere. This picture has emerged largely from our study of the neutral composition obtained from the Aeronomy Satellite–neutral atmosphere temperature experiment (AEROS-NATE) experiment. To illustrate our viewpoint, I have taken atomic oxygen as an example. This is a major constituent between 200 and 600 km, where most of the density data from satellite drag are available.

Figure 1 shows the seasonal and latitudinal variation in exospheric temperature and atomic oxygen at 120 km. The abscissa is geodetic latitude with the Equator in the center and the North and South Poles to the right and left sides. The ordinates are exospheric temperature and the number density. The temperature shown is not measured temperature but is inferred from N_2

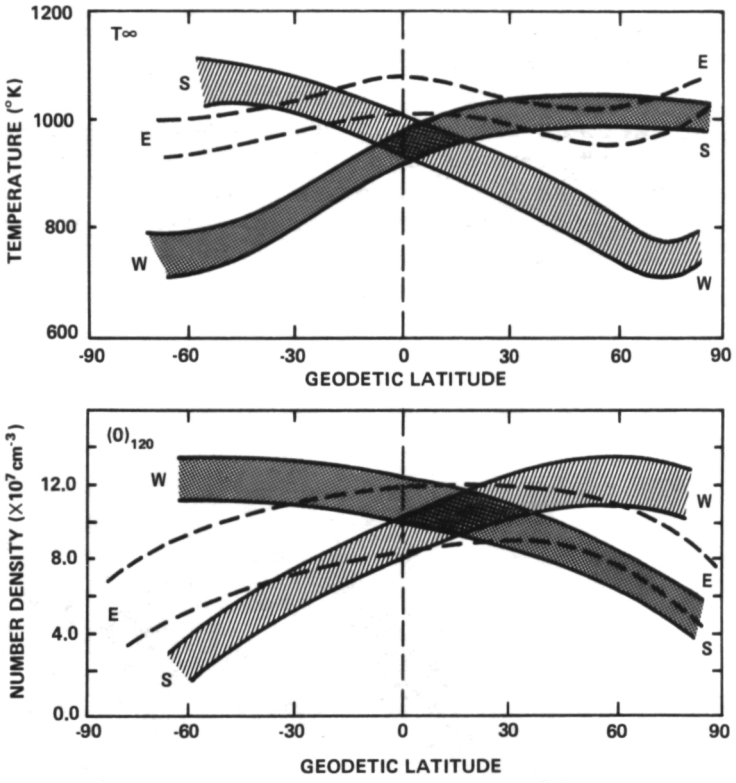

Figure 1. Seasonal and latitudinal variations in exospheric temperature and atomic oxygen at 120 km.

measurements at the spacecraft altitude. Similarly, atomic oxygen number density at 120 km is inferred from the measurement at spacecraft altitude by assuming diffusive equilibrium. The data shown correspond to the daytime conditions in the summer, winter, and equinox for 3 typical days. (These conditions are denoted by S, W, and E in the figure.) First we consider the changes in temperature corresponding to northern winter. The temperature in this case rises from about 700 K in the winter polar region to about 1100 K in the southern summer region. The situation is very much the same when we consider the condition corresponding to the northern summer or the southern winter. The equinox temperature is more like a summer temperature and shows enhancement only in the equatorial region. The behavior of atomic oxygen at 120 km is very different from that of exosphere temperature. During both winter and summer months, it is in antiphase with respect to exospheric temperature. In the equinoctial months it lies between the summer

and the winter curves, even though there is considerable spread in the data. When we examine the seasonal characteristics of atomic oxygen at 400 km, the results are very much what one expects (figure 2). The maximum density or the so-called density bulge is usually confined to the equatorial region. On a global scale, the density in equinoctial month is higher almost everywhere compared to either summer or winter conditions. This feature has been characterized as semiannual variation, and, as we see here, it is a good example of the coupling between the upper and the lower thermospheres which are governed by different physical processes.

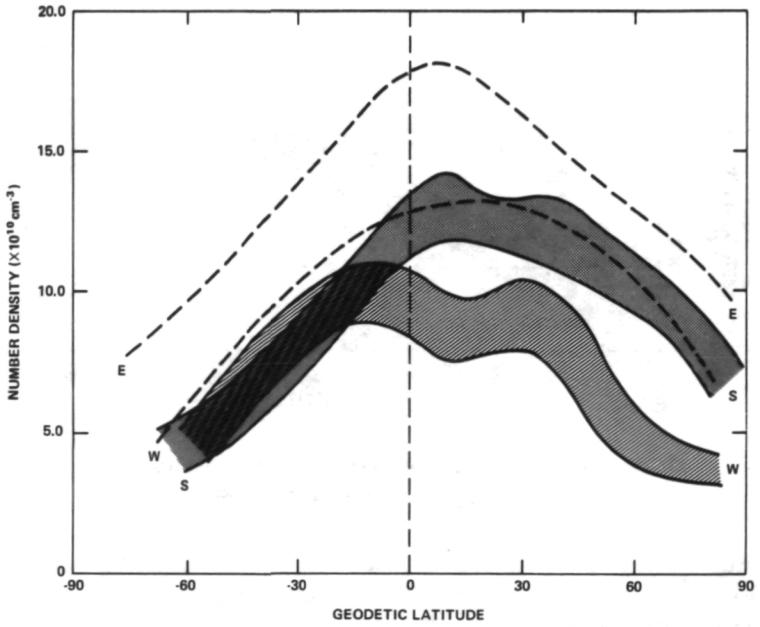

Figure 2. Seasonal and latitudinal variations in atomic oxygen at 400 km.

DISCUSSION

NORDBERG: Where did those temperatures at 120 km come from?

CHANDRA: These are not temperatures. They are densities. What I showed was atomic oxygen density at 120 km. The densities are measured at the spacecraft altitude in the 200- to 600-km region. We extrapolate the density to 120 km by assuming diffusive equilibrium.

"The aeronautical and space activities of the United States shall be conducted so as to contribute . . . to the expansion of human knowledge of phenomena in the atmosphere and space. The Administration shall provide for the widest practicable and appropriate dissemination of information concerning its activities and the results thereof."

—NATIONAL AERONAUTICS AND SPACE ACT OF 1958

NASA SCIENTIFIC AND TECHNICAL PUBLICATIONS

TECHNICAL REPORTS: Scientific and technical information considered important, complete, and a lasting contribution to existing knowledge.

TECHNICAL NOTES: Information less broad in scope but nevertheless of importance as a contribution to existing knowledge.

TECHNICAL MEMORANDUMS: Information receiving limited distribution because of preliminary data, security classification, or other reasons. Also includes conference proceedings with either limited or unlimited distribution.

CONTRACTOR REPORTS: Scientific and technical information generated under a NASA contract or grant and considered an important contribution to existing knowledge.

TECHNICAL TRANSLATIONS: Information published in a foreign language considered to merit NASA distribution in English.

SPECIAL PUBLICATIONS: Information derived from or of value to NASA activities. Publications include final reports of major projects, monographs, data compilations, handbooks, sourcebooks, and special bibliographies.

TECHNOLOGY UTILIZATION PUBLICATIONS: Information on technology used by NASA that may be of particular interest in commercial and other non-aerospace applications. Publications include Tech Briefs, Technology Utilization Reports and Technology Surveys.

Details on the availability of these publications may be obtained from:

SCIENTIFIC AND TECHNICAL INFORMATION OFFICE

NATIONAL AERONAUTICS AND SPACE ADMINISTRATION

Washington, D.C. 20546